Orthogonal Tight Binding Model for Silicon Carbide

Paul Kamenski: St. Edmund Hall – Oxford

Thesis for the Degree of Master of Science by Research

Submitted Trinity Term 2011

Abstract:

A new orthogonal tight binding (OTB) model for the silicon carbide (Si-C) system is presented. The model is parameterized in the reduced TB form which provides a critical step towards the development of an analytic bond-order potential (BOP) for Si-C. Coarse-grained from density functional theory (DFT), through TB, analytic BOPs address a number of the deficiencies of current interatomic potentials for Si-C including the neglect of explicit π-bonding and more accurate σ-bond contributions. Furthermore, the new reduced OTB model is important within TB in its own right as the first simple, selfconsistent OTB model parameterized specifically for SiC without the use of any averaging of elemental interactions. Selfconsistency is achieved through local charge neutrality (LCN). The distance-dependent functions used to define the Hamiltonian matrix elements in the two-centre approximation were obtained directly from given DFT-projected data, and repulsive parameters were fit to DFT binding energies. The electronic structure, binding energies, and heat of formation for the groundstate structures are reproduced well with no spurious groundstate structures found in a database of over 200 unique crystal structures. The significant improvements over existing OTB models for elemental Si and C and the binary SiC results show good promise for further applicability in modelling a wide range of phenomena in Si-C such as thin film growth or interfaces in general.

Thesis for the Degree of Master of Science by Research

Orthogonal Tight Binding Model for Silicon Carbide

Paul Kamenski
St. Edmund Hall - Oxford

Supervisors: David Pettifor, Ralf Drautz, Aleksey Kolmogorov

Approximate number of words: 23,000

Trinity Term 2011

Table of Contents

This thesis is dedicated to my wife,
Claire.

1 Introduction

This thesis aims to contextualize and present a new reduced orthogonal tight binding (OTB) model for the silicon carbide (Si-C) system. The context includes discussions of the SiC material and how it can be modelled on an atomic scale. The new reduced OTB model is then presented with a number of tests.

The motivation for modelling SiC is addressed in Chapter 2 which reviews a number of aspects of the material. First, the many technological uses of SiC are highlighted in Section 2.1 followed by a discussion of the phase diagram and structure of SiC in Section 2.2. The synthesis and mechanical properties of SiC are then discussed in Sections 2.3 and 2.4. Given the uses of SiC and how its properties depend on atomic-scale events, the applicability of atomistic modelling is discussed in Section 2.5.

A number of different methods for modelling SiC on an atomic scale including density functional theory (DFT), tight binding (TB), and interatomic potentials are discussed in Chapter 3. DFT results provide reference values throughout this thesis. The various types of TB models used to study the Si-C system are then reviewed in Section 3.3 to contextualize the current reduced OTB model. The formalism behind reduced TB is discussed in Subsection 3.3.3, defining what it means for a TB model to be a *reduced* TB model including what further approximations are made beyond traditional TB. The effect of these approximations is not germane to TB per se, but rather provides a direct link to the further development of an analytic bond-order potential (BOP). Given this close relationship and next logical step in subsequent

model development, analytic BOPs are reviewed in Section 3.4, with other common interatomic potentials for Si-C reviewed in Sections 3.5 to 3.7. Chapter 3 will therefore make clear the importance of the new reduced OTB model for Si-C in its own right as a TB model in addition to its importance as a critical step along the way towards the development of an analytic BOP for Si-C.

Moving on to the new model, Chapter 4 begins with an introduction and all the functional forms and parameterizations in Sections 4.1 and 4.2, completely defining the new model. Following the coarse-graining of DFT to TB discussed in Chapter 3, the extraction of many of the reduced OTB parameters from DFT-projected data and DFT binding energies is discussed in Sections 4.3 and 4.4. The fitting program used to obtain the final best quantitative agreement is then discussed in Section 4.5.

Using the model described in Chapter 4, a number of tests are presented in Chapter 5. First, in testing the DFT-projected Hamiltonian parameters, electronic structure tests are presented in Section 5.1. Binding energy curves are then presented in Section 5.2 to show the transferability of the reduced OTB model to different coordinations, geometries, and compositions. Sections 5.3 and 5.4 provide reference histograms of coordination shells at equilibrium for select structures and bond, promotion, and repulsive energy contributions, respectively, highlighting where the pairwise distance-dependent functions tend to be accessed and what the resultant energy contributions are. The histograms of coordination shells at equilibrium further provide an indication of how thoroughly the pairwise distance-dependent functions were tested using the elemental and binary structure test beds created for this work.

Further groundstate equilibrium data is presented through the equation of state fits and heats of formation shown in Sections 5.5 and 5.6. Finally, further distortions about the equilibrium elemental and binary groundstate structures are tested through the elastic constant calculations and relaxed point defect energies discussed in Sections 5.7 and 5.8.

The thesis ends with a conclusion Chapter 6, an appendix of all tested crystal structures in Chapter 7, and finally references in Chapter 8.

2 Silicon carbide

2.1 Applications

SiC is of technological interest because of its application both as a structural and electronic material [3, 15-17]. As a structural material, SiC has been used in gas turbines, heat exchangers, ceramic fans, bearings, valves, seals, and protective coatings against wear and corrosion [3, 15, 17]. These applications utilize SiC's hardness, stiffness, good wear resistance, chemical inertness, thermal stability, and low thermal expansion [3, 15].

Other applications of SiC in electronics make use of its good dielectric properties, wide band gap, high electron mobility, and high barrier for electron breakdown [12, 13]. Such applications have been in high-power, high-frequency, and high-temperature devices including X-ray masks, microelectronic devices, passivation and antireflection coatings, as well as in radar, microwave, solar cell, and high-voltage devices [3, 16].

Amorphous SiC is of additional interest due to its semiconducting properties [13]. Certainly all these technologically important properties are related to the structure of SiC.

2.2 Structure

In group IV of the periodic table, carbon and silicon each have four valence electrons, which in the atomic ground state have an s^2p^2 occupation. As molecules and in the

solid state, these elements exhibit a wide range of bonding due to hybridization. Well known examples include the sp^2 hybridized state of carbon in graphite and the sp^3 hybridized state of silicon in its ambient diamond structure.

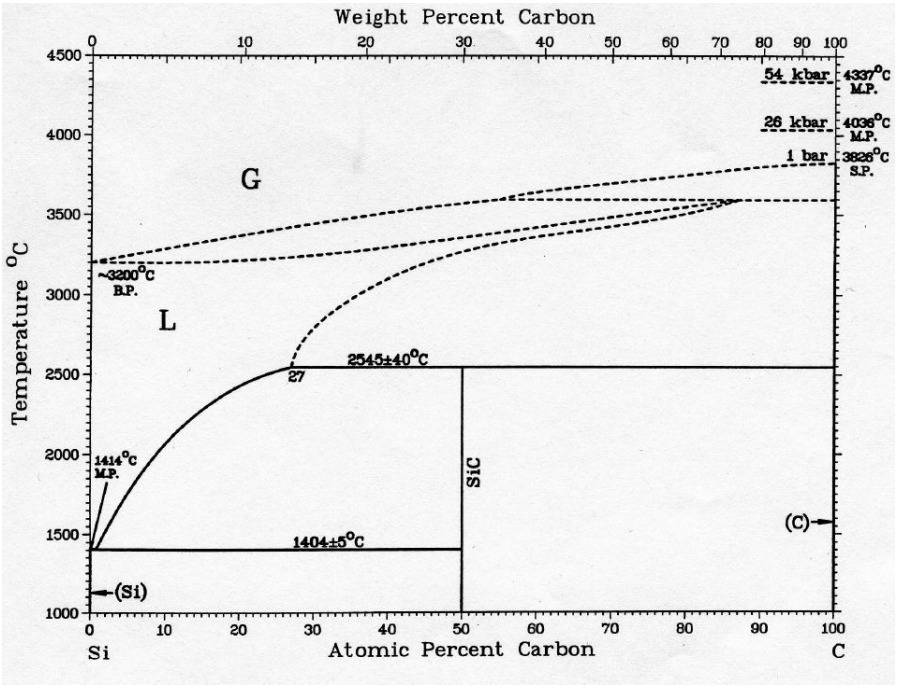

Fig. 2.1. Si-C phase diagram [14].

As shown by the phase diagram for the Si-C system in Fig. 2.1, the only non-elemental phase is a 1:1 stoichiometric line compound. In this line compound at ambient conditions, the carbon and silicon atoms are sp^3 hybridized forming tetrahedral coordinations. This coordination is not unexpected given that the diamond crystal structure is very low in energy for silicon and carbon. The compound B3 crystal structure of SiC is a binary equivalent to the diamond structure. The complexity of the material at this composition lies in the fact that in addition to the cubic B3 crystal structure, SiC forms more than 200 different related structures [3].

These structures, known as polytypes, are related by different stacking sequences of two-dimensional layers of tetrahedrally coordinated silicon and carbon atoms. Just as the elemental face-centered-cubic (FCC) crystal structure is known to have an ABCABC… repeating stacking sequence and the elemental hexagonal-close-packed (HCP) crystal structure is known to have an ABAB… repeating stacking sequence, SiC forms the ABC B3 polytype as well as the AB B4 polytype. Using Ramsdell notation, the cubic B3, "β", or "zincblende" SiC polytype is called "3C" for its three repeating layers and cubic symmetry, whereas the hexagonal B4 structure is called "2H" for its two repeating layers and hexagonal symmetry [15]. In addition to cubic and hexagonal symmetries, SiC can exhibit rhombohedral symmetry, as in the 15R structure [15]. By convention, all SiC polytypes other than B3 are considered to be "α" SiC [15]. The most abundant polytypes are 3C, 6H, 4H, and 2H, with small energy differences, at maximum, calculated by DFT to be 4.3 meV/atom [3].

Bernstein et al. proposed that the charge asymmetry of the Si-C bond should be related to the polytypism of SiC [16]. Given experimental references and their TB results, they noticed that in reference to the hexagonal crystal structure, the *a* lattice parameter decreases with hexagonality but *c* increases, thus distorting the tetrahedral bonding.

In addition to the polytypism of fourfold coordinated SiC, it has been found from X-ray diffraction measurements that SiC transforms to a sixfold coordinated B1 (rocksalt) structure at a pressure above 100 GPa, with a 20% reduction in volume [13].

2.3 Synthesis

Developments in the synthesis of SiC have primarily been related to thin film deposition techniques, ingot production, and sintering. Thin films have been deposited by laser-assisted physical vapor deposition (PVD), pure laser ablation, dynamic ion mixing, plasma-enhanced chemical vapor deposition (CVD), pack cementation, and magnetron sputtering [12, 17].

SiC is mainly deposited by CVD, typically at a deposition temperature of 1000 ˚C [12]. Nanocrystalline SiC films can be deposited by thermal plasma CVD at a growth rate of approximately 10 micron/min [18]. A major variable in the CVD process is the substrate deposition temperature. For nanocrystalline SiC, as the substrate temperature increases, the average SiC grain size, the crystalline fraction in the film, and the hardness all increase [18].

The growth of SiC ingots to produce wafers for electronic applications was difficult due to the presence of high defect densities. The best commercially available three inch diameter ingots (B4 SiC) had dislocation densities of 10^3-10^4 cm^{-2} and micropipe densities of 10-100 cm^{-2} [19]. This was until Nakamura et al. succeeded in developing a process to create the ingots “virtually dislocation-free” in 2004 [19]. Like the CVD growth of SiC films, this synthesis technique is now fairly well controlled.

SiC coatings produced using a pack cementation technique have had problems with porosity and cracks [17]. To enhance the integrity of the coating, an extra Si-rich layer can be added to fill in the cracks, providing a diffusion barrier for oxidation

resistance, but the fundamental problem of porosity and cracking in the SiC from the cementation technique has not yet been overcome.

To enhance the sliding-wear resistance and toughness of sintered SiC, elongated grains have been produced by adding 20 vol% yttrium aluminum garnet (YAG) during sintering [20]. It was proposed that the elongated grains are created as a result of a polytype transformation away from the B3 structure, but no further explanation, structurally or mechanistically, has been provided.

Overall it appears as though synthetic techniques for producing SiC have been successful. Still, these techniques could benefit from further research where gaps in the understanding are present. This is particularly the case for questions related to the relationship between synthesis parameters and subsequent mechanical properties as discussed in the next section.

2.4 Mechanical properties

Perhaps the most used mechanical property of SiC is its hardness: standard B3 SiC has a hardness of approximately 28 GPa [18], whereas the hardest steels have a hardness of 2-3 GPa [21]. In fact, much research has been done to enhance the hardness of SiC by altering its structure, for instance through different deposition conditions, or by using it in a composite material [15, 17, 22, 24]. The drawback of SiC is that it has a low inherent fracture toughness, a K_{Ic} on the order of 2-3 MPa $m^{1/2}$ [22]. In comparison, a 4340 alloy steel has a K_{Ic} of 50-87 MPa $m^{1/2}$ [21]. To improve SiC's toughness, processing or reinforcement routes in a composite could play a critical role.

Liao et al. discussed the hardness of a number of SiC coatings. They found several investigators reporting hardness ranging from 40-80 GPa for SiC-diamond composites formed through high-pressure, high-temperature powder sintering [18]. Hydrogen-free amorphous SiC films, synthesized by magnetron cosputtering of graphite and silicon, had hardness values of 45-55 GPa; however, amorphous SiC films usually contain hydrogen and have a much lower hardness around 10-20 GPa.

As part of a composite, SiC has been used in a thin film multilayer with Si_3N_4 [12] and with diamond-like carbon [22]. By itself, SiC has been deposited in nanocrystalline form [18]. In all cases, increases in hardness have been reported, and for nanocrystalline SiC, fracture toughness increased to 3.9-4.8 MPa $m^{1/2}$. Discussions of substrate deposition temperature effects have been varied.

When SiC was used in a thin film multilayer composite with Si_3N_4, Lattemann et al. found that the hardness was subject to competing effects from the deposition temperature [12]. As the deposition temperature increased, there was increased hardness from structural relaxation, but at higher deposition temperatures, the hardness dropped due to a decrease in the film stress.

In Zhao et al.'s study of SiC/diamond-like carbon thin film composites deposited on steel via electron beam PVD, a rather simple explanation of the substrate deposition temperature effect was proposed [22]. As the substrate temperature increased, the size

of the nanocrystalline B3 SiC grains increased, and the amount of amorphous phase decreased, resulting in an increase in hardness.

In another study, nanocrystalline SiC deposited films were similarly shown to have increasing hardness with increasing substrate deposition temperature [18], but the exact cause was not identified. Rather, it was proposed that the substrate temperature effect could be explained through the enhanced formation of the sp^3 phase versus amorphous (as suggested in Zhao et al.'s study above), the crystalline phase composition, or the grain size and density.

Although various structures of SiC with enhanced mechanical properties over the bulk are well established, numerous discussions of substrate deposition temperature effects indicate that consensus has not been reached regarding the effects of this critical variable. Further research may yield mechanical property optimization techniques.

2.5 Modelling motivation

Due to the fact that the above mentioned mechanical properties and synthesis techniques are related to atomic-scaled phenomena, atomistic simulations of SiC could prove valuable to the study and enhancement of this technologically important material. Nevertheless, the modelling of Si-C systems through computer simulations remains difficult. Many phenomena arise from atomic/microstructural events that occur on length scales which DFT simulations cannot access. Simulations using interatomic potentials can access some of these length scales, but the potentials often lack transparency and accuracy.

2.6 Summary

SiC is well known as a material used for both structural and electronic applications. The phase diagram is rather simple with a single line compound forming at 1:1 compositions. The 1:1 composition compound tends to form heteronuclear tetrahedral bonding configurations, as found in the elemental diamond structures, with different polytypes showing different long-ranged order and amorphous structures showing no long-ranged order. The material is produced using a number of different techniques including CVD growth, ingot production, and sintering. SiC is perhaps best known for its hardness, with much work dedicated to increasing the hardness and ensuring sufficient fracture toughness. Atomistic materials modelling studies may prove helpful to this end.

3 Atomistic materials modelling

3.1 Introduction

This chapter aims to summarize and contextualize the various types of atomistic models used to study the Si-C system. DFT models provide reference quantum mechanical accuracy, often for small-scale systems. TB models include further approximations to allow for larger-scale simulations while still maintaining quantum mechanical accuracy. Finally, interatomic potentials simplify atomic interactions by assuming dependence only on the *local* topology of a material, allowing for the largest-scale atomistic simulations.

The quantum mechanical models used in this work are discussed in Sections 3.2 and 3.3. DFT is discussed briefly in Section 3.2 as its results serve as a reference in the present work. Coarse-grained from DFT, TB is reviewed in Section 3.3, particularly as it relates to the Si-C system. The formalism behind the final model from this work is discussed in Subsection 3.3.3 on reduced TB.

Interatomic potentials based on the local topology of a given material are then discussed in Sections 3.4-3.7. Many of the models for the Si-C system are based on the concept of the bond order. From chemistry, for the simplest case of *s*-orbitals, the bond order between atomic sites *i* and *j* is given by:

$$\Theta_{ij} = \frac{1}{2}\left(N_{+} - N_{-}\right), \tag{1}$$

where N_+ is the number of electrons in bonding states and N_- is the number of electrons in antibonding states. Analytic bond-order potentials having further been coarse-grained from reduced TB are discussed in Section 3.4, as the next logical step in SiC model development following the present reduced OTB model.

The currently most used interatomic potentials for SiC are versions of Tersoff's model [1] and belong to the Abell-Tersoff-Brenner (ATB) family of potentials, for comparison discussed in Section 3.5. Another class of potentials has been developed through recursive inversion of DFT cohesive energy curves. These 'environment-dependent interatomic potentials' (EDIPs) are discussed in Section 3.6. A three-body interatomic potential has been developed for SiC by Vashishta et al. [13], building off of the Stillinger and Weber potential for silicon [23], and is discussed in Section 3.7.

A reactive force field (ReaxFF) potential was fit for Si-C interactions to study poly(dimethylsiloxane) polymer (PDMS) at high temperature and pressure [24]. Since this model has not been fit for or used to study bulk SiC, it is not discussed further.

Overall, atomistic materials modelling has been used to study an array of phenomena in SiC. Both Monte Carlo [25] and Molecular Dynamics [27-30] methods have been used to study dynamics with models ranging from simple rigid ion models [26] to ATB type potentials [3]. Elastic and thermal properties of SiC have been modelled successfully [26-30]. Brittle fracture of B3 SiC has been studied under hydrostatic pressure [27]. Surface reconstructions [28] and radiation damage studies, including

amorphization and point defect production have been reported [34-37]. Deformation mechanisms in nanocrystalline SiC have been studied [29-31], and a high-pressure structural transition study has been reported [13].

3.2 Density functional theory

In order to obtain sufficient accuracy in simulating materials, the electronic structure must be included. In principle, the many-electron Schrödinger equation,

$$\hat{H}\Psi\left(\mathbf{r}_1,\mathbf{r}_2,...,\mathbf{r}_N\right)=E\Psi\left(\mathbf{r}_1,\mathbf{r}_2,...,\mathbf{r}_N\right), \tag{2}$$

would need to be solved, where $\hat{H}$ is the many-body Hamiltonian. However, this is too complicated to solve and therefore requires simplification. This was done within DFT by working with the charge density instead of the wave-function [32], which reduced the many-body Schrödinger equation to a set of effective one-electron Kohn-Sham equations:

$$\left(-\frac{\hbar^2}{2m}\nabla^2+V_{ion}+V_H+V_{xc}\right)\psi_n(r)=\varepsilon_n\psi_n(r). \tag{3}$$

The first contribution in the Hamiltonian is the kinetic energy, the second contribution is the Coulomb potential due to the ionic cores (assumed to be fixed), and the third contribution is the Hartree potential arising from the average electronic charge distribution. The last contribution is the exchange-correlation potential which arises from electron-electron interactions that are ignored in the Hartree approximation. The exact exchange-correlation potential is unknown but good approximations are available. Equation (3) must then be solved selfconsistently as the input potential depends on the output charge density.

3.3 Tight binding

Before DFT was developed, approximations were being made to make quantum mechanical calculations more feasible. Perhaps the most important of those assumptions, which led to the development of the TB approach, were made by Slater and Koster in 1954 [33].

These assumptions included treating the Hamiltonian matrix elements as functions of a resolved angular component and a bond integral: the bond integral is parameterized as a function of interatomic distance and goes to zero beyond a certain interatomic separation. These matrix elements arise from treating the eigenfunctions as a linear combination of near-valence atomic orbitals. The representation of the eigenfunctions is given by the LCAO form,

$$\left|\psi_n\right\rangle = \sum_{i\alpha} c_{i\alpha}^{(n)} \left|i\alpha\right\rangle, \tag{4}$$

where $\left|i\alpha\right\rangle$ is the i-th atomic site's orbital, for instance $\alpha = s, p_x, p_y, p_z$. Finally, Slater and Koster proposed the critical two-centre approximation stating that,

$$\left\langle i\alpha\right|V_j\left|k\beta\right\rangle = 0, \quad i \neq j \neq k, \tag{5}$$

resulting in a sparse Hamiltonian matrix.

Starting from these approximations made by Slater and Koster [33], research has been done in a number of directions: to review the theoretical basis of TB, to develop methods to solve exactly or approximately the TB equations, to make TB models more accurate and transferable, and finally to make TB models faster through further approximations [34].

Some of the original TB work on the diamond and B3 crystal structures was done by Chadi and Cohen studying valence bandstructures in 1975 [35]. They started to explain structures in the electronic density of states (DOS) through relations with the bond integrals and atomic energy level splitting, $\left|E_{i\alpha} - E_{j\alpha}\right|$. They also showed how including second-nearest-neighbor interactions in their TB model affected the DOS.

The 'Solid State Table of the Elements,' published by Harrison in 1980 [36] was a further important development within TB, later updated in 2004 [37]. This reference included what would become widely used bond integral expressions and atomic energy levels across the periodic table. For silicon and carbon the bond integral distance dependence was given as,

$$\beta_{ll'm} = \frac{\alpha_{ll'm}}{r_{ij}^2}, \tag{6}$$

where $ll'm = ss\sigma, sp\sigma, pp\sigma, pp\pi$ and $\alpha_{ll'm}$ is a constant. The only difference between silicon and carbon in this model was the atomic onsite energy levels, hence no species dependence in Equation (6). In 1981 Harrison also did a study on covalent materials adding a higher-energy state, *s**, as a perturbation, without increasing the size of the Hamiltonian [38]. This modification was done to achieve higher accuracy in the conduction bands, but is not necessarily important if studies relate strictly to the valence bands.

Another TB model was developed specifically for SiC by Li and Lin-Chung in 1987 to study the electronic properties of native defects in B3 SiC [39]. This model

included expressions related to overlap contributions, abandoning the simple functional forms used by Harrison, but repulsive contributions were not published.

Also in the late 1980s, roughly 35 years after Slater and Koster's seminal paper on TB approximations [33] and roughly 20 years after the development of DFT [32], that the connection between DFT and TB was made explicit [40, 41]. In 1988, Finnis et al. concluded that TB was now partially justified *ab initio* [40]. In 1989, Foulkes and Haydock showed how TB models could be understood as stationary approximations to selfconsistent DFT if the TB charge density is close to the ground state density and the potential is close to the selfconsistent potential [41].

The development of a total energy TB model specifically for SiC began with the selfconsistent TB model.

3.3.1 Selfconsistent tight binding model

In 1987, Majewski and Vogl developed a semi-empirical, first- and second-nearest-neighbor, selfconsistent tight binding (SCTB) scheme including charge transfer and non-orthogonality [42]. Their model used Harrison's 1980 [36] bond integrals and was tested on 62 binary compounds. Non-orthogonality was introduced into the onsite elements as an extra term. They found that inclusion of the s^* higher-energy state and second-nearest neighbors had little influence on cohesive properties, in agreement with Harrison.

In 1989 Kohyama et al. extended Majewski and Vogl's SCTB model by including a description of the forces [43], as this had been left out of the original paper [42]. In

1990 Kohyama et al. applied the SCTB model, in a slightly modified form, to SiC [44]. They examined several functional forms especially for the overlap function contribution to the onsite energy since SiC had a positive heat of formation and close-packed structural energies were too high. They suggested going beyond the universal scaling bond integrals from Harrison [36].

In 1990 and 1991 Kohyama et al. used their SCTB model for SiC to study grain boundaries in B3 SiC [45, 46]. Even though they suggested going beyond the use of Harrison's bond integrals, they still used the r_{ij}^{-2} universal scaling dependence to study the effect of homonuclear bonds and polarity at the grain boundary. They reported that even though the changes in the onsite levels were small, the overall electrostatic contribution to the total energy was important. Later it was pointed out that this model could not reproduce, to within 1.5 eV/atom, the energies of both the B3 and B1 structures [47].

3.3.2 The tight binding bond model

In 1988, a year after Majewski and Vogl's SCTB model was developed, Sutton et al. proposed a new total energy expression from a derivation based on the difference between input and output charge densities, correct to second order in the difference [48]. In this tight binding bond model (TBBM), the energy for locally charge neutral materials is given by,

$$U_{binding} = U_{bond} + U_{prom} + U_{rep}, \tag{7}$$

where the bond energy and promotion energy are found by solving the Hamiltonian, and the repulsive energy can be taken as pairwise. U_{bond} has two representations given as,

$$U_{bond} = \sum_{i\alpha} \int_{-\infty}^{E_F} \left(E - E_{i\alpha}\right) n_{i\alpha}\left(E\right) dE = \sum_{i \neq j} \sum_{\alpha,\beta} H_{i\alpha,j\beta}^{\mu\upsilon} \Theta_{j\beta,i\alpha}^{\mu\upsilon}, \tag{8}$$

where E_F is the Fermi energy, $E_{i\alpha}$ is the atomic onsite energy level, $n_{i\alpha}$ is the local electronic DOS, and Θ is the bond order [6]. The promotion energy results from the promotion of electrons into higher energy levels for hybridization. In its simplest form for the case of a locally charge neutral *sp*-valent material, it is given as,

$$U_{prom} = \sum_{i} \left(E_{ip} - E_{is}\right) \Delta N_{is}, \quad \Delta N_{is} = N_{is}^{0} - N_{is}, \tag{9}$$

where ΔN_s^{μ} is the difference in the number of electrons in the *s*-orbital with respect to the occupancy of the *s*-state of the free atom. This expression holds true for the case of local charge neutrality (LCN) since $\Delta N_{is} = -\Delta N_{ip}$. LCN was advocated by Sutton et al. as the simplest route to selfconsistency, with a justification given through a discussion of screening and the definitions of the localized orbital basis [48]. Sutton et al.'s major contention was with the prevalence of non-selfconsistent TB calculations, where serious errors occur through the neglect of variations in the potential caused by charge flow.

Sutton et al. discussed the exchange and correlation energies to justify treating them through a pairwise repulsive energy, given as

$$U_{rep} = \frac{1}{2} \sum_{i \neq j} \Phi\left(R_{ij}\right). \tag{10}$$

U_{rep} can also be expressed through an embedding function [5, 7] or can include many-body screening effects [49].

The legitimacy of the TBBM was made more explicit by Paxton in contrast to models that group the bond and promotion energies into a sum over occupied eigenstates, known as band models [50]. When calculated in a non-selfconsistent manner, the two methods are indistinguishable; however, for selfconsistent calculations, the bond model was shown to be consistent with the force theorem [51]. More specifically, in the TBBM there is no contribution to the forces from selfconsistent redistribution of charge resulting from atomic displacement. If the selfconsistent system is perturbed, changes in the electron-electron interaction are canceled in the 'double counting term' from DFT. Such a cancelation does not exist for band models because the 'double counting term' is included in the pairwise repulsive term.

3.3.3 Reduced tight binding

As described above, conventionally, TB Hamiltonians are constructed using a minimal basis of atomic-like valence orbitals. Following from Equation (8), for an *sp*-valent system, this allows the bond energy to be partitioned into σ- and π- bonding contributions,

$$U_{bond} = \sum_{i \neq j} \left[\left(U_{\sigma\, bond} \right)_{ij}^{\mu\upsilon} + \left(U_{\pi\, bond} \right)_{ij}^{\mu\upsilon} \right], \tag{11}$$

where μ and υ represent the species of atoms *i* and *j*. Again from Equation (8), assuming a bond along the *z*-axis, the individual contributions can be calculated from the trace of the Hamiltonian matrix multiplied with the bond-order matrix [52],

$$\left(U_{\sigma\,bond}\right)_{ij}^{\mu\upsilon} = \mathrm{Tr}\begin{pmatrix} ss\sigma_{ij}^{\mu\upsilon} & sp\sigma_{ij}^{\mu\upsilon} \\ ps\sigma_{ij}^{\mu\upsilon} & pp\sigma_{ij}^{\mu\upsilon} \end{pmatrix}\begin{pmatrix} \Theta_{js,is}^{\upsilon\mu} & \Theta_{js,iz}^{\upsilon\mu} \\ \Theta_{jz,is}^{\upsilon\mu} & \Theta_{jz,iz}^{\upsilon\mu} \end{pmatrix}, \tag{12}$$

and,

$$\left(U_{\pi\,bond}\right)_{ij}^{\mu\upsilon} = \mathrm{Tr}\begin{pmatrix} pp\pi_{ij}^{\mu\upsilon} & 0 \\ 0 & pp\pi_{ij}^{\mu\upsilon} \end{pmatrix}\begin{pmatrix} \Theta_{jx,ix}^{\upsilon\mu} & \Theta_{jx,iy}^{\upsilon\mu} \\ \Theta_{jy,ix}^{\upsilon\mu} & \Theta_{jy,iy}^{\upsilon\mu} \end{pmatrix}, \tag{13}$$

where the Hamiltonian matrix elements are given by,

$$\begin{aligned} ss\sigma_{ij}^{\mu\upsilon} &= \langle i\mu s | H | j\upsilon s \rangle, \\ sp\sigma_{ij}^{\mu\upsilon} &= \langle i\mu s | H | j\upsilon z \rangle, \\ ps\sigma_{ij}^{\mu\upsilon} &= \langle i\mu z | H | j\upsilon s \rangle, \\ pp\sigma_{ij}^{\mu\upsilon} &= \langle i\mu z | H | j\upsilon z \rangle, \\ pp\pi_{ij}^{\mu\upsilon} &= \langle i\mu x | H | j\upsilon x \rangle = \langle i\mu y | H | j\upsilon y \rangle. \end{aligned} \tag{14}$$

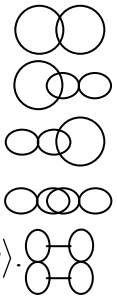

This then leads to the σ-bond contribution,

$$\left(U_{\sigma\,bond}\right)_{ij}^{\mu\upsilon} = \left(ss\sigma_{ij}^{\mu\upsilon}\Theta_{js,is}^{\upsilon\mu} + sp\sigma_{ij}^{\mu\upsilon}\Theta_{jz,is}^{\upsilon\mu} + ps\sigma_{ij}^{\mu\upsilon}\Theta_{js,iz}^{\upsilon\mu} + pp\sigma_{ij}^{\mu\upsilon}\Theta_{jz,iz}^{\upsilon\mu}\right), \tag{15}$$

and two π-bond contributions,

$$\left(U_{\pi\,bond}\right)_{ij}^{\mu\upsilon} = pp\pi_{ij}^{\mu\upsilon}\left(\Theta_{jx,ix}^{\upsilon\mu} + \Theta_{jy,iy}^{\upsilon\mu}\right) = \beta_{\pi,ij}^{\mu\upsilon}\Theta_{\pi,ji}^{\upsilon\mu}, \tag{16}$$

where $\beta_{\pi,ij}^{\mu\upsilon} \equiv pp\pi_{\pi,ij}^{\mu\upsilon}$ and $\Theta_{\pi,ji}^{\upsilon\mu}$ is the sum of the two individual π bond orders in the *x* and *y* directions as defined in [52]. Using the conventional, atomic-like orbital basis therefore yields four σ bond-order terms, shown in Equation (15), as opposed to a simple scalar quantity commonly referred to in chemistry and empirical or coarse-grained interatomic potentials.

Reduced TB models, first defined for elemental systems [53] and then for multicomponent systems [52], are a special class of TB models wherein the σ bond energy can be written as,

$$\left(U_{\sigma\,bond}\right)_{ij}^{\mu\upsilon}=\beta_{\sigma,ij}^{\mu\upsilon}\Theta_{\sigma,ji}^{\upsilon\mu},\tag{17}$$

with a single scalar σ bond order, $\Theta_{\sigma,ji}^{\upsilon\mu}$. This is achieved by constructing a new minimal basis set of *bonding* and *non-bonding hybrid* orbitals that form a singular σ Hamiltonian matrix block. The *bonding hybrids* taking the form,

$$\begin{aligned}\left|i\mu\sigma\right\rangle&=\sqrt{1-p_{\sigma,ij}^{\mu(\upsilon)}}\left|i\mu s\right\rangle+\sqrt{p_{\sigma,ij}^{\mu(\upsilon)}}\left|i\mu z\right\rangle,\\ \left|j\upsilon\sigma\right\rangle&=\sqrt{1-p_{\sigma,ji}^{\upsilon(\mu)}}\left|j\upsilon s\right\rangle-\sqrt{p_{\sigma,ji}^{\upsilon(\mu)}}\left|j\upsilon z\right\rangle,\end{aligned}\tag{18}$$

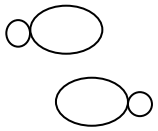

and the *non-bonding hybrids* taking the form,

$$\begin{aligned}\left|i\mu\sigma^{*}\right\rangle&=\sqrt{p_{\sigma,ij}^{\mu(\upsilon)}}\left|i\mu s\right\rangle-\sqrt{1-p_{\sigma,ij}^{\mu(\upsilon)}}\left|i\mu z\right\rangle,\\ \left|j\upsilon\sigma^{*}\right\rangle&=\sqrt{p_{\sigma,ji}^{\upsilon(\mu)}}\left|j\upsilon s\right\rangle+\sqrt{1-p_{\sigma,ji}^{\upsilon(\mu)}}\left|j\upsilon z\right\rangle,\end{aligned}\tag{19}$$

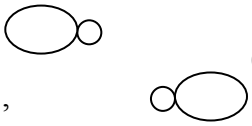

where p_{σ} is species-dependent and can be taken either as a constant, p_{σ}^{μ}, or as a function of the local environment, $p_{\sigma,ij}^{\mu(\upsilon)}\left(R_{ij}\right)$. By making the reduced TB approximation [52] that

$$sp\sigma_{ij}^{\mu\upsilon}\,ps\sigma_{ij}^{\mu\upsilon}=ss\sigma_{ij}^{\mu\upsilon}\,pp\sigma_{ij}^{\mu\upsilon},\tag{20}$$

and provided,

$$\sqrt{p_{\sigma,ij}^{\mu(\upsilon)}\,p_{\sigma,ij}^{\upsilon(\mu)}}=\frac{pp\sigma_{ij}^{\mu\upsilon}}{\left|ss\sigma_{ij}^{\mu\upsilon}\right|},\tag{21}$$

and,

$$\sqrt{\frac{p_{\sigma,ij}^{\upsilon(\mu)}}{p_{\sigma,ij}^{\mu(\upsilon)}}}=\frac{sp\sigma_{ij}^{\mu\upsilon}}{\left|ps\sigma_{ij}^{\mu\upsilon}\right|},\tag{22}$$

the Hamiltonian matrix elements can be defined as,

$$\left\langle i\mu\sigma\left|H\right|j\upsilon\sigma\right\rangle=\beta_{\sigma,ij}^{\mu\upsilon},\tag{23}$$

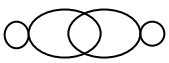

$$\left\langle i\mu\sigma\left|H\right|j\upsilon\sigma^{*}\right\rangle=0,\tag{24}$$

$$\left\langle i\mu\sigma^{*}\left|H\right|j\upsilon\sigma\right\rangle=0,\tag{25}$$

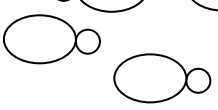

$$\left\langle i\mu\sigma^{*}\left|H\right|j\upsilon\sigma^{*}\right\rangle=0.\tag{26}$$

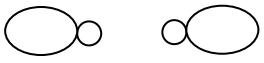

This leads the 2x2 σ block of the Hamiltonian to take the diagonal and singular form,

$$H_{\sigma,ij}^{\mu\upsilon} = \begin{array}{c} \\ |i\mu\sigma\rangle \\ |i\mu\sigma^*\rangle \end{array} \begin{array}{c} \begin{array}{cc} |j\upsilon\sigma\rangle & |j\upsilon\sigma^*\rangle \end{array} \\ \begin{pmatrix} \beta_{\sigma,ij}^{\mu\upsilon} & 0 \\ 0 & 0 \end{pmatrix} \end{array}. \tag{27}$$

Manipulating Equations (18) to (26), Pettifor et al. [52] related the four conventional independent TB σ bond integrals to the three reduced TB parameters $\beta_{\sigma,ij}^{\mu\upsilon}$, $p_{\sigma,ij}^{\mu(\upsilon)}$, and $p_{\sigma,ij}^{\upsilon(\mu)}$ as follows,

$$\left.\begin{array}{l} ss\sigma_{ij}^{\mu\upsilon} \\ sp\sigma_{ij}^{\mu\upsilon} \\ ps\sigma_{ij}^{\mu\upsilon} \\ pp\sigma_{ij}^{\mu\upsilon} \end{array}\right\} = \left.\begin{array}{l} -\sqrt{\left(1-p_{\sigma,ij}^{\mu(\upsilon)}\right)\left(1-p_{\sigma,ji}^{\upsilon(\mu)}\right)} \\ \sqrt{\left(1-p_{\sigma,ij}^{\mu(\upsilon)}\right)p_{\sigma,ji}^{\upsilon(\mu)}} \\ -\sqrt{p_{\sigma,ij}^{\mu(\upsilon)}\left(1-p_{\sigma,ji}^{\upsilon(\mu)}\right)} \\ \sqrt{p_{\sigma,ij}^{\mu(\upsilon)}p_{\sigma,ji}^{\upsilon(\mu)}} \end{array}\right\} \left|\beta_{\sigma,ij}^{\mu\upsilon}\right|. \tag{28}$$

So long as a TB parameterization satisfies the reduced TB approximation in Equation (20) and the final relations in Equation (28), the model will yield σ bond energy contributions which depend on a single scalar σ bond order, as the other three contributions are multiplied by zero valued Hamiltonian matrix elements. This is particularly useful for further development of interatomic potentials based on the concept of a scalar σ bond order.

3.3.4 Tight binding models for the silicon-carbon system

Goodwin, Skinner, and Pettifor (GSP) developed a new functional form for the bond integrals and repulsive term including a fit for elemental silicon [54] to then be used with the TBBM. This was developed to increase the transferability of the bond integrals by implicitly including screening through an exponentially decaying term. A number of subsequent TB models have used this functional form, including models

for elemental carbon and silicon published by the Ames group [5, 7]. The distance dependence is given by,

$$f_{GSP}\left(R_{ij}\right) = f\left(R_o\right)\left(\frac{R_o}{R_{ij}}\right)^n \exp\left\{n\left[-\left(\frac{R_{ij}}{R_c}\right)^{n_c} + \left(\frac{R_o}{R_c}\right)^{n_c}\right]\right\}, \tag{29}$$

where R_0 can be taken as an equilibrium nearest-neighbor distance and all other new variables are fitting parameters.

First, the Ames group used the GSP functional form [54] in 1992 to parameterize an OTB model for carbon, published by Xu et al. [5]. With the goal of increasing transferability, they modified the TBBM formalism to included an embedded-type repulsive energy given in reference [55] as,

$$U_{rep} = \sum_i F\left(\sum_{j\neq i} f_{GSP}\left(r_{ij}\right)\right), \quad F\left(x\right) = \sum_{i=1}^{4} A_i x^i, \tag{30}$$

where A_i variables are additional fitting parameters.

When discussing work on small clusters, Xu et al. introduced a Hubbard-like term to handle the effects of charge transfer. This addition to the total energy was given as,

$$U_{Cou} = \frac{1}{2}u\left(q_i - q_i^o\right)^2, \tag{31}$$

where q_i is the Mulliken population at atomic site i, q_i^o is 4 for carbon, and u was taken to be 4 eV. Even with the enhanced flexibility over the GSP model, Xu et al. struggled to properly model the higher-coordinated theoretical phases of carbon, and so focused on the graphite, linear chain, and diamond structures as shown in Fig. 3.1.

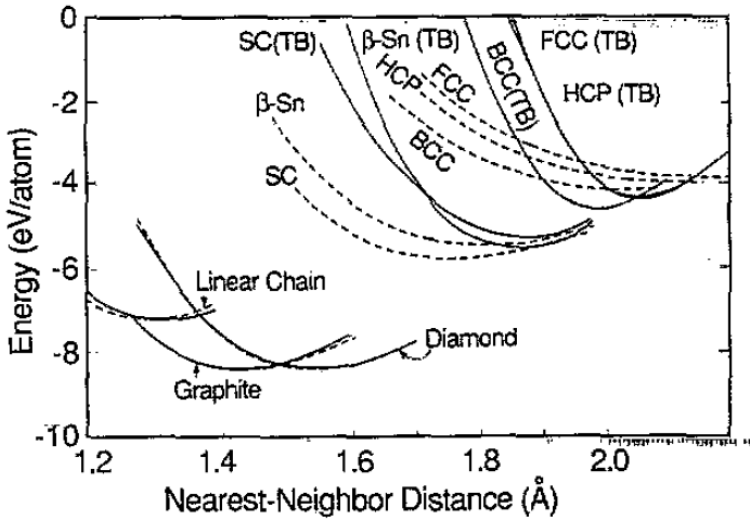

Fig. 3.1. Cohesive energy versus nearest-neighbor distance curves for various structures of carbon. Full and broken lines show the results form OTB and DFT calculations, respectively [5].

Later, the Ames group created an OTB model for silicon with a similar form, published by Kwon et al. [7]. They noted that Harrison's r_{ij}^{-2} scaling for the bond integrals cutoff very slowly for molecular dynamics simulations, so they too used the GSP functional form [54]. Kwon's unique modification was to include orbital interaction, *ll'm*, dependencies to parameters n_c and r_c for additional flexibility. In comparison to the original GSP model for silicon [54] with the strictly pairwise repulsive term and lack of orbital interaction dependencies, Kwon et al. found that for molten silicon, the integration of the first peak in their pair correlation function was much closer to Car-Parrinello molecular dynamics (CPMD) and experimental results. This effective molten coordination number was 6.47 for the Kwon model and 7.17 for the GSP model, in comparison to the CPMD result of 6.5 and the experimental value of 6.4 [7].

However, Kwon et al. found that for small silicon clusters, cohesive energies were slightly lower and bond lengths slightly longer than *ab initio* calculations. No reference to the use of a Hubbard-like term to handle charge transfer was discussed, as was done for the carbon cluster study in Xu et al.'s report.

Shown in Fig. 3.2, Kwon et al.'s cohesive energy curves compared well with DFT data, besides some discrepancies in the equilibrium nearest-neighbor distances for the hypothetical higher-coordination structures. They proposed that *d*-state mixing may be important for these metallic structures, implying the need for an *spd* OTB model for silicon.

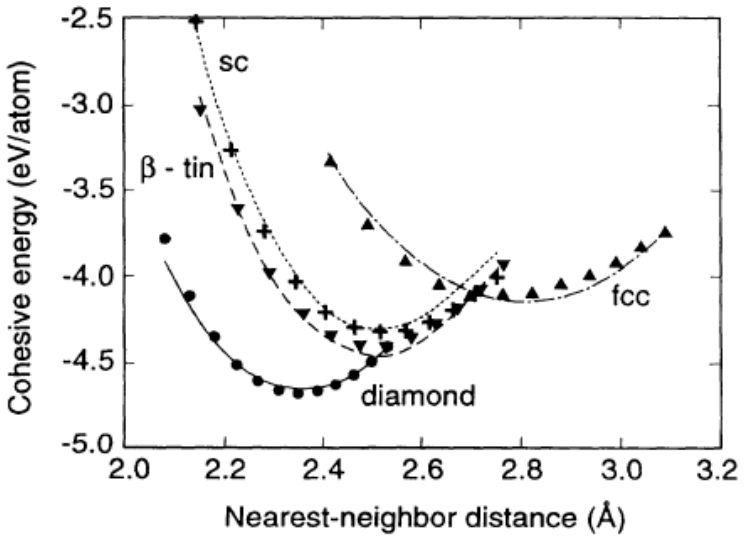

Fig. 3.2. Cohesive energy as a function of nearest-neighbor distance for several bulk phases of silicon. The points are DFT calculations, and lines are from the OTB model. Reprinted with permission from APS [7].

In fact in 1992, two years prior to Kwon et al.'s publication, Robertson proposed the use of a more extensive sp^3s^*-basis for a nearest-neighbor OTB model to study hydrogenated amorphous Si-C alloys [56]. Even including the extended basis,

Robertson found it difficult to fit the bands of elemental silicon and SiC with a common set of silicon orbital energies, indicating that perhaps the minimal sp^3-basis may not be OTB's largest approximation.

Striving to better reproduce the metallic structures for elemental carbon, in 1996, Tang et al., also part of the Ames group, extended Xu et al.'s previous model to include environment dependence through a screening function and coordination scaling effects on the interatomic separation [9]. These additions were made because Tang et al. proposed that the two-centre approximation of Slater and Koster [33] may be insufficient for metallic structures; however, the additions were made in a way such that the two-centre Hamiltonian was still preserved. Whether it was the inclusion of more physics or simply more fitting parameters, given their cohesive energy curves results shown in Fig. 3.3, compared with Fig. 3.1, it is clear that the model is more transferable.

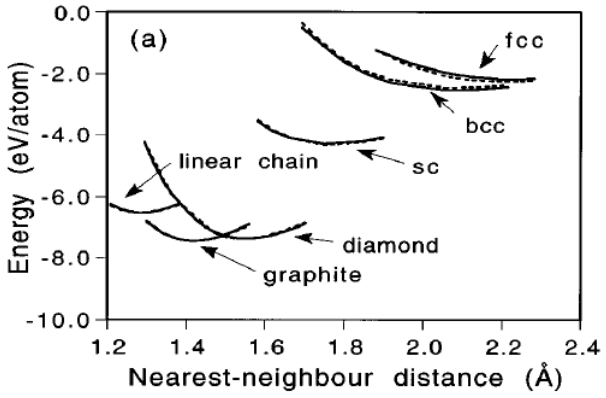

Fig. 3.3. Binding energies as a function of nearest-neighbor distance for carbon in different crystalline structures. The solid curves are TB results and the dashed curves are DFT results [9].

Acknowledging that Tang et al.'s introduction of environment dependence was the most successful to date, Nguyen-Manh et al. strove to *derive* such environment

dependencies of the bond integrals to avoid the *ad hoc* introduction of a rapidly increasing number of parameters for compound systems [49]. They began by inverting the non-orthogonality TB matrix and justifying an approximation that the screening was carried out via valence *s*-orbitals on neighboring sites. Finally by neglecting terms involving the differences in onsite energies, an explicit screening function was derived. It was found that the bond integrals became more transferable by including the screening in this manner.

Mercer in 1996 proposed a method for combining elemental TB models, such as those discussed above for silicon [7] and carbon [5], to study compound systems [47]. The method avoided repeated diagonalization of the Hamiltonian, as done in other selfconsistent models, by parameterizing shifts in the onsite energy levels in terms of interatomic interactions. Mercer applied this method to SiC, but did not use published elemental models for silicon and carbon. Instead Mercer fit up to eight-term mixed polynomial-exponential functions for the bond integrals and distance dependencies for the onsite terms.

Mercer reported calculating "large values" for the intra-atomic elements which tended to rise "very rapidly" as the lattice constant decreases, proposing this was possibly due to kinetic energy contributions from overlapping orbitals. Nevertheless, by letting the intra-atomic terms shift and taking an arithmetic average of the elemental bond integrals, Mercer was able to reproduce the large-volume clathrate and small-volume B1 structural energies better than other models. For this case, even though the

calculations were non-selfconsistent, variations in the potential caused by charge flow are treated empirically by adding this contribution to the intra-atomic terms.

A number of other non-selfconsistent models were published in subsequent years for Si, C, and SiC [20, 66-72]. Papaconstantopoulos et al. reported a non-orthogonal TB model for C and Si [57] with an extension to SiC [16] requiring the fitting of 134 parameters using an *sp*-basis. They also included a model using an *spd*-basis to improve the representation of the conduction band. It was later reported that their model for SiC worked well for crystalline polytypes but did not give rise to stable nanostructures as found experimentally [58]. Other non-orthogonal TB models have been developed for nanostructures and small clusters of SiC but claim no transferability to the bulk [68, 72].

Fu et al. used Xu et al.'s model for elemental carbon [5] and Kwon et al.'s model for elemental silicon [7] to propose a model for SiC [59]. This was done to study amorphous C on a Si surface through molecular dynamics. Fu et al. justified not using Kohyama's SCTB model for SiC [44] stating that it was not proven to be useful for surfaces and cluster systems. They also noted that the non-orthogonal methods were computationally expensive for use in molecular dynamics. Fu et al. used Mercer's idea of averaging the elemental bond integral values to create bond integrals for the compound [47], but chose to use a weighted average for the repulsive functional coefficients and pair-repulsive function. Along with the repulsive weighting parameters, Fu et al. fitted shifts to the atomic energy levels to get the 'correct' charge transfer for SiC. Although the Tersoff interatomic potential better reproduced

the energy and lattice parameter of B3 SiC, Fu et al.'s model much better reproduced those values for the B1 structure.

Salvador et al. published a TB model for SiC in 2004 [60], five years after Fu et al.'s publication, using the exact same idea to average the elemental bond integrals and take weighted averages for the repulsive term without making reference to Fu et al.'s model. Furthermore, Salvador et al. neglected shifting the onsite atomic energy levels as Fu et al. properly did, resulting in a model which predicted electron transfer to silicon, away from carbon, in direct opposition to an electronegativity argument.

In 2002 Ivashchenko et al. published a non-selfconsistent model for SiC neglecting charge transfer which used an sp^3s^*-basis to better reproduce the conduction bands [61]. Although references to the parameterization of the sp^3s^* model were given, no discussion was found in the references. Also, there was no discussion of onsite atomic energy levels.

In summary, it appears as though Kwon et al.'s OTB model for silicon has a good combination of accuracy and simplicity for fast calculation. Xu et al.'s simple OTB model for carbon was quite successful, but to achieve higher accuracy, Tang et al.'s model included further environment dependence. For high-accuracy TB calculations of SiC, a number of non-orthogonal TB models have been developed with moderate success, but the development of a simple OTB model for SiC is still an open issue. Schemes to derive heteronuclear interactions from averaged elemental interactions

have been proposed, but as of yet, an explicit parameterization for sp^3 OTB interactions for Si-C has not been published.

3.4 Analytic bond-order potentials

Beginning in 1989, Pettifor began the movement of deriving analytic BOPs from TB [62]. This movement has continued to the present with reports of systematic extensions of the theory. The link between the k-space TB representation of the electronic states and the real-space, local topological representation of the electronic states in analytic BOPs has been established, rendering the much-sought-after DFT-derived form of an interatomic potential.

In contrast with the interatomic potentials discussed in later sections, the derivation of analytic BOPs is made through approximations to the TB representation of the electronic structure. Connecting with the TBBM, the total energy is the same as Equation (7), a sum of repulsive, promotion, and bond energy contributions [10]. The repulsive energy is treated as described in the TBBM Subsection 3.2.2. The promotion energy can be approximated as:

$$U_{prom} = \frac{1}{2}\sum_{i \neq j} \delta \left\{ 1 - \left[1 + \left(A \frac{\beta_{ij,\sigma}}{\delta} \right)^2 \right]^{-1/2} \right\}, \tag{32}$$

where A and δ are constants and $\beta_{ij,\sigma}$ represents the σ bond integral [10]. The vast majority of the work in deriving analytic BOPs has been to derive the bond orders in the bond energy contribution:

$$U_{bond} = \sum_{i \neq j} \left[\beta_{\sigma,ij} \Theta_{\sigma,ij} + \beta_{\pi,ij} \Theta_{\pi,ij} \right], \tag{33}$$

where $\Theta_{\sigma(\pi),ij}$ represents the $\sigma(\pi)$ bond order between sites *i* and *j*. This explicit treatment of σ- and π-bonds separately is in contrast with the single attractive bond-order term found in many interatomic potentials as discussed later. These analytic BOPs have already been able to capture structural trends across the periodic table [63] and have been applied to silicon and the hydrocarbons [4, 10].

3.4.1 Theory

In 1989, Pettifor introduced the concept of deriving the bond-order formalism for use in interatomic potentials [62]. In this way, there was no need to assume functional forms for the bond order's dependence on the environment. Starting with the simplest *s*-valent case, the recursion method was used to write the bond order as an integral over the difference of two continued fractions. Even at this early stage in analytic BOP development, a connection was made to the formalism of the common embedding potentials used to model metals.

In 1992 and 1993 Aoki and Pettifor furthered the work done in 1989, deriving the bond order with angular dependence through a linearized many-atom expansion using the sum rule [64, 65]. Exact within the TB approximation, this new bond-order expression was shown to fulfill the sum rule hence being equivalent through both the intersite and site-diagonal approaches.

A number of reviews of the analytic BOP derivation have been published [13, 77-79]: a summary is given here. The derivation begins with an expansion of the bond order through its relation to the intersite Green's function:

$$\Theta_{ij} = -\frac{2}{\pi}\,\mathrm{Im}\int^{\varepsilon_F} G_{ij}(\varepsilon)\,d\varepsilon. \tag{34}$$

Off-diagonal matrix elements of the Green's function are then calculated from the diagonal elements G_{00}^{λ},

$$G_{00}^{\lambda} = \left\langle u_0^{\lambda} \middle| \left[\varepsilon - \hat{H}\right]^{-1} \middle| u_0^{\lambda} \right\rangle, \tag{35}$$

where

$$\left|u_0^{\lambda}\right\rangle = \frac{1}{\sqrt{2}}\left[\left|i\right\rangle + \exp\left(i\cos^{-1}(\lambda)\right)\left|j\right\rangle\right]. \tag{36}$$

The intersite Green's function G_{ij} may then be calculated by taking the derivative of G_{00}^{λ} with respect to λ using the BOP theorem [64]:

$$G_{ij} = \frac{\partial}{\partial\lambda} G_{00}^{\lambda}. \tag{37}$$

Using the Lanczos recursion algorithm, the diagonal Green's function elements are then related to a continued fraction:

$$G_{00}^{\lambda} = \cfrac{1}{\varepsilon - a_0^{\lambda} - \cfrac{\left(b_1^{\lambda}\right)^2}{\varepsilon - a_1^{\lambda} - \cfrac{\left(b_2^{\lambda}\right)^2}{\varepsilon - a_2^{\lambda} - \ldots}}}. \tag{38}$$

The set of recursion coefficients $\{a_n, b_n\}$ can be expressed in terms of the moments of the DOS $\{\mu_p\}$, namely:

$$\begin{aligned}
\mu_1 &= a_0, \\
\mu_2 &= a_0^2 + b_1^2, \\
\mu_3 &= a_0^3 + 2a_0 b_1^2 + a_1 b_1^2, \\
\mu_4 &= a_0^4 + 3a_0^2 b_1^2 + 2a_0 a_1 b_1^2 + a_1^2 b_1^2 + b_1^4 + b_1^2 b_2^2.
\end{aligned} \tag{39}$$

The moments of the DOS can then be written as a sum over all self-returning hopping paths within the local atomic environment [66, 67], given as

$$\mu_p = \sum_{i\alpha} \int E^p n_{i\alpha}(E)\, dE = \sum_{i\alpha} \sum_{j\beta j'\beta'\ldots} H_{i\alpha j\beta} H_{j\beta j'\beta'} H_{j'\beta'\ldots} \ldots H_{\ldots i\alpha}, \tag{40}$$

thus providing the critical link between the electronic states and the local atomic environment.

Using the second-moment matrix approximation, the σ and π bond orders are given by [52]:

$$\Theta_{ij,\sigma}^{\mu\upsilon,(2)} = \frac{1}{\sqrt{1 + \sum_{k\neq i,j} \left(g_{jik,\sigma}^{\mu}\right)^2 \left(\widehat{\beta}_{ik,\sigma}^{\mu\kappa}\right)^2}} \tag{41}$$

and

$$\Theta_{ij,\pi}^{\mu\upsilon,(2)} = \frac{1}{\sqrt{1 + \Phi_{2\pi} - \sqrt{\Phi_{4\pi}}}} + \frac{1}{\sqrt{1 + \Phi_{2\pi} + \sqrt{\Phi_{4\pi}}}}, \tag{42}$$

where $g_{jik,\sigma}^{\mu}$ is an angular function between a μ atomic species at site i and neighboring sites j and k given by,

$$g_{jik,\sigma}^{\mu} = 1 + p_{\sigma}^{\mu}\left(\cos\theta_{jik} - 1\right). \tag{43}$$

The normalized bond integral $\widehat{\beta}_{ik,\sigma}^{\mu\kappa} = \beta_{ik,\sigma}^{\mu\kappa} / \beta_{ij,\sigma}^{\mu\upsilon}$ measures the relative strength of a neighboring σ bond to that of the σ bond of interest. $\Phi_{2\pi}$ and $\Phi_{4\pi}$ are the second-moment matrix two-hop and four-hop contributions given by

$$\Phi_{2\pi} = \sum_{k\neq i,j} \left[\sin^2\theta_{jik} \frac{p_{\pi}^{\mu}}{1 + p_{\pi}^{\mu}} \left(\frac{\beta_{ik,\sigma}^{\mu\kappa}}{\beta_{ij,\pi}^{\mu\upsilon}}\right)^2 + \left(1 + \cos^2\theta_{jik}\right) \left(\frac{\beta_{ik,\pi}^{\mu\kappa}}{\beta_{ij,\pi}^{\mu\upsilon}}\right)^2 \right], \tag{44}$$

$$\Phi_{4\pi} = \sum_{k,k'\neq i,j} \Bigg(\sin^2\theta_{jik} \sin^2\theta_{jik'} \left(\widehat{\beta}_{ik}^{\mu\kappa}\right)^2 \left(\widehat{\beta}_{ik'}^{\mu\kappa'}\right)^2 + \sin^2\theta_{jik} \sin^2\theta_{ijk'} \left(\widehat{\beta}_{ik}^{\mu\kappa}\right)^2 \left(\widehat{\beta}_{ik'}^{\mu\kappa'}\right)^2 + \sin^2\theta_{ijk} \sin^2\theta_{ijk'} \left(\widehat{\beta}_{jk}^{\upsilon\kappa}\right)^2 \left(\widehat{\beta}_{jk'}^{\upsilon\kappa'}\right)^2 + \sin^2\theta_{ijk} \sin^2\theta_{jik'} \left(\widehat{\beta}_{jk}^{\upsilon\kappa}\right)^2 \left(\widehat{\beta}_{jk'}^{\upsilon\kappa'}\right)^2 \Bigg) \frac{\cos\left(\theta_{kijk'}\right)}{4}, \quad (45)$$

where

$$\left(\widehat{\beta}_{ik}^{\mu\kappa}\right)^2 = \frac{p_\pi^\mu}{1+p_\pi^\mu} \left(\frac{\beta_{ik,\sigma}^{\mu\kappa}}{\beta_{ij,\pi}^{\mu\upsilon}}\right)^2 - \delta^\mu \left(\frac{\beta_{ik,\pi}^{\mu\kappa}}{\beta_{ij,\pi}^{\mu\upsilon}}\right)^2, \quad (46)$$

where δ^μ is a parameter [10]. The σ bond order in Equation (41) from this second-moment matrix approximation is equivalent in form to the bond order in the ATB potentials discussed later in Section 3.5.

Together with the π bond order, these expressions are derived systematically from DFT through TB, including an electronic DOS shape parameter [66]. In contrast with the ATB potentials, the breaking of saturated π-bonds and radical formation are described explicitly. Likewise, there is no need for an *ad hoc* torsional stiffness term around double bonds as was included in the REBO potential [68].

Moving beyond the σ bond-order connection with ATB potentials, Pettifor and Oleinik extended the bond-order expression to four levels of recursion to better describe structural trends [8]. Additionally, in 2004, Pettifor et al. generalized the analytic BOP formalism for the case of multicomponent *sp*-valent systems [52]. After discussing the relation between the shape of the electronic DOS and structural stability, a derivation was given as to why the second-moment contribution alone can not distinguish between structures. This has critical bearing on the ATB family of

potentials, as they are, in essence, second-moment based interatomic potentials. They must then *fit* the structural energy differences, since such results can not come from the functional form. The new expressions for the fourth-moment derived bond orders taken from reference [10] included four-member ring terms given by:

$$\Theta_{ij,\sigma}^{\mu\upsilon,(4)} = \left\{ 1 + \frac{\Phi_{i,2\sigma} + \Phi_{j,2\sigma} + \left(\frac{\delta^{\mu}}{\beta_{ij,\sigma}^{\mu\upsilon}} \right)^2 + R_{ij,4\sigma} + \widetilde{\Phi}_{i,2\sigma}\widetilde{\Phi}_{j,2\sigma}\left(2 + \Delta\widetilde{\Phi}_{4\sigma}\right)}{\left(1 + \Delta\widetilde{\Phi}_{4\sigma}\right)^2} \right\}^{-1/2}, \quad (47)$$

where

$$\Delta\widetilde{\Phi}_{4\sigma} = \frac{\Delta\Phi_{4\sigma}}{\sqrt{\Delta\Phi_{4\sigma} + \Phi_{i,2\sigma}\Phi_{j,2\sigma}}}, \quad (48)$$

$$\widetilde{\Phi}_{i,2\sigma}\widetilde{\Phi}_{j,2\sigma} = \frac{\Phi_{i,2\sigma}\Phi_{j,2\sigma}}{\sqrt{\Delta\Phi_{4\sigma} + \Phi_{i,2\sigma}\Phi_{j,2\sigma}}}, \quad (49)$$

$$\Delta\Phi_{4\sigma} = \frac{\Phi_{4\sigma} - 1/2\left[\left(\Phi_{i,2\sigma}\right)^2 + \left(\Phi_{j,2\sigma}\right)^2\right]}{1/2\left(\Phi_{i,2\sigma} + \Phi_{j,2\sigma}\right)}. \quad (50)$$

$\Phi_{i,2\sigma}$, $\Phi_{4\sigma}$, and $R_{ij,4\sigma}$ represent self-returning hopping paths and can be written as

$$\Phi_{i,2\sigma} = \sum_{k\neq i,j}\left(g_{jik,\sigma}^{\mu}\right)^2\left(\widehat{\beta}_{ij,\sigma}^{ik}\right)^2, \widehat{\beta}_{ij,\sigma}^{ik} = \left(\frac{\beta_{ik,\sigma}^{\mu\kappa}}{\beta_{ij,\sigma}^{\mu\upsilon}}\right), \quad (51)$$

$$\begin{aligned}\Phi_{4\sigma} = &\sum_{k\neq i,j}\left(g_{jik,\sigma}^{\mu}\right)^2\left(\widehat{\beta}_{ij,\sigma}^{ik}\right)^4 + \sum_{k\neq i,j} g_{jik,\sigma}^{\mu} g_{kik',\sigma}^{\mu} g_{k'ij,\sigma}^{\mu}\left(\widehat{\beta}_{ij,\sigma}^{ik}\right)^2\left(\widehat{\beta}_{ij,\sigma}^{ik'}\right)^2 \\ &+ \sum_{k,k'\neq i,j}\left(g_{jik,\sigma}^{\mu} g_{ikk',\sigma}^{\kappa}\right)^2\left(\widehat{\beta}_{ij,\sigma}^{ik}\right)^2\left(\widehat{\beta}_{ij,\sigma}^{kk'}\right)^2,\end{aligned} \quad (52)$$

$$R_{ij,4\sigma} = \sum_{k,k'\neq i,j} g_{jik,\sigma}^{\mu} g_{ikk',\sigma}^{\kappa} g_{kk'j,\sigma}^{\kappa'} g_{ijk',\sigma}^{\upsilon}\left(\widehat{\beta}_{ij,\sigma}^{ik}\right)\left(\widehat{\beta}_{ij,\sigma}^{kk'}\right)\left(\widehat{\beta}_{ij,\sigma}^{k'j}\right). \quad (53)$$

The second-moment expressions for the π bond order beginning with Equation (42) are used with this σ bond order since the fourth-moment expressions for the π bond order are complicated, or perhaps impossible, to derive analytically.

The self-returning hopping path functions used to define the bond orders relate directly to the local topology as shown in Fig. 3.4.

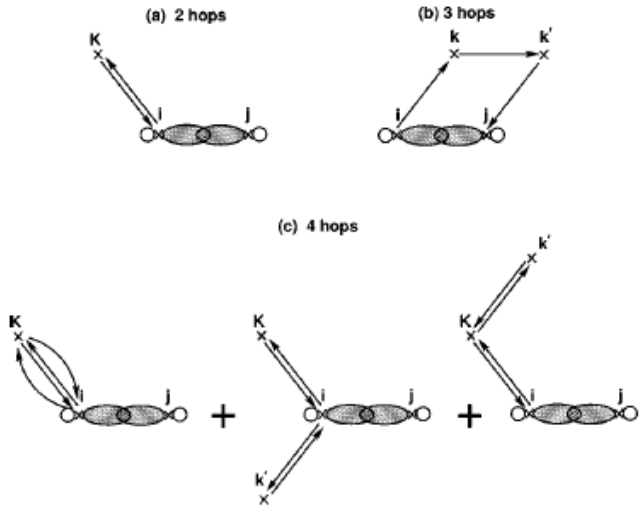

Fig. 3.4. Self-returning hopping paths of length 2 (a) and length 4 (c) which contribute to the potential functions $\Phi_{i,2\sigma}$ and $\Phi_{4\sigma}$, respectively. The hopping path of length 3 (b) contributes to the four-member ring function, $R_{ij,4\sigma}$ [8].

In a study of structural trends across the *sp*-valent elements, Drautz et al. extended analytic BOPs to include an explicit valence dependence [69], where previous derivations were only for half-full *sp*-bands. This was done by extrapolating from half-full occupancy using a simple envelope function. Neglecting *s*-*p* onsite energy level splitting, Drautz et al. was able to reproduce the trends expressed in the "8-N rule," stating that the coordination of an atom will go as eight less the number of its *sp*-valence electrons.

A major success of the analytic BOP method was that it was able to predict the stability of the puckered graphene structure shown by the pnictogens, which is stabilized by the *p*-orbitals [69]. Bent structures are a common pathological case for the interatomic potentials later reviewed in Sections 3.5 to 3.7. It was noted however, that the analytic BOP formalism still needs extending to include ionic contributions.

The resultant analytic BOPs are one order of magnitude slower than ATB potentials [4, 70], but nevertheless provide a rigorous framework that treats the σ- and π-bonds separately and explicitly. In addition, the use of more levels of recursion to approximate TB provides a systematic way to include higher moment contributions to the bond energies, and hence improve the accuracy of the calculations.

3.4.2 Applications

In 2006, Murdick et al. applied the analytic BOP formalism to the GaAs system [71], making use of the extension to multicomponent systems [52]. For ease of fitting, the U_{prom} term was grouped into the U_{rep} term, leaving the total energy expression,

$$U_{tot} = U_{rep} + U_{bond}. \tag{54}$$

Murdick et al. retained two levels of recursive representation for both the σ- and π-bonds orders and used GSP functions [54] for both the bond integrals and repulsive pair function. They found their parameter set to not be transferable enough to predict both bulk and tetramer structures. There were also significant deviations in the bulk modulus, melting temperature, and formation energy of interstitials, although improvement was reported in comparison to other models. It was proposed that the model may benefit significantly from the incorporation of screening and/or charge

transfer. Nevertheless, this model was used to study the deposition of GaAs and was able to demonstrate, for the first time, both the substrate temperature and flux ratio effects on the atomic structure [6].

Gillespie et al. created an analytic BOP for silicon retaining four levels of recursive representation in 2007 [10]. Their potential preferred large atomic spacings in clusters in comparison to Hartree-Fock calculations and had significant discrepancies in defect energies compared to DFT. However, as depicted in Fig. 3.5, comparison with other interatomic potentials for silicon showed the much improved predictive power of this model, especially concerning defect energetics shown in the bottom-right panel [6]. Gillespie et al. also noted that potentials using environment-independent repulsive terms tend to incorrectly predict a positive Cauchy pressure, but analytic BOPs resolve this issue through the promotion energy [10]. In comparison with other silicon potentials, the analytic BOP shows improved results for surface calculations, in particular for the 7x7 surface reconstruction.

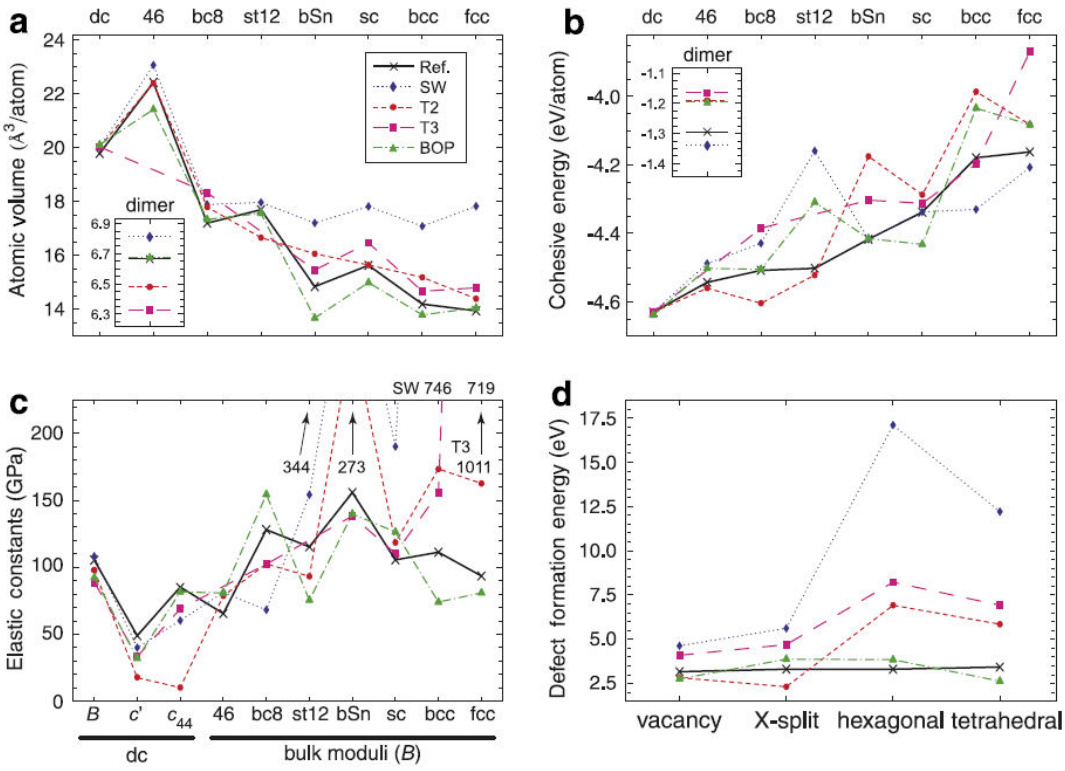

Fig. 3.5. (a) Atomic volume, (b) cohesive energy, and (c) elastic constants for a variety of silicon phases. (d) Defect energy of the diamond-cubic silicon structure [6].

A further development to the analytic BOP formalism was made by Mrovec et al. in an application to the hydrocarbon system by including a higher-order atomic onsite energy level splitting contribution to the σ bond-order term [4]. Specific examples of its effects were given, such as the fixing of the overcoordination found in amorphous structures when onsite energy level splitting is neglected. As a test of the analytic BOP formalism, Mrovec et al. did not attempt to improve on existing TB models for carbon, but instead tried to reproduce the Xu et al. model [5] to exemplify the power of the recursion process.

Mrovec et al. concluded that the results of their analytic BOP were limited by the TB model they used. In comparison with ATB potentials, the incorporation of the π bond order rendered a good description of the barrier to rotation of ethylene. When

studying amorphous structures, Mrovec et al. reported that both the Tersoff and Brenner potentials fail to describe the correct fraction of sp^3 hybridized atoms, including the density dependence. The analytic BOP displayed the correct trend, but had a significantly lower sp^3 fraction than experiment, as shown in Fig. 3.6.

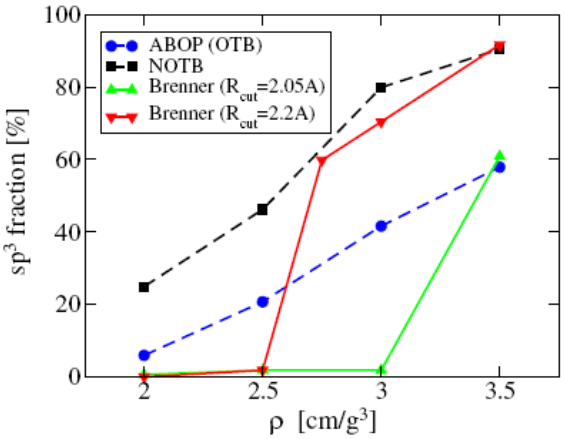

Fig. 3.6. Variation of sp^3 content in amorphous-C:H samples predicted by analytic BOP, non-orthogonal TB, and two Brenner potentials with different cutoffs [4].

3.5 Abell-Tersoff-Brenner interatomic potentials

To date, the most popular interatomic potentials used to simulate Si-C have all fallen under the umbrella of nearest-neighbor ATB potentials developed through the work of Abell, Tersoff, and Brenner since the 1980s.

Abell first introduced the generic form for this potential,

$$U = \frac{1}{2}\sum_{i \neq j}\left[f_R\left(R_{ij}\right) + b_{ij} f_A\left(R_{ij}\right)\right], \tag{55}$$

where U is the energy, f_R and f_A are repulsive and attractive pair potentials respectively, R_{ij} is the atomic separation, and b_{ij} is the empirical bond order [72].

For metallic and molecular bonding, using chemical pseudopotential theory, Abell showed that for *s*-valent systems the local coordination number *z* dominates the bond order and therefore set

$$b_{ij} \propto \left(z_i\right)^{-1/2}. \tag{56}$$

The pair interactions, f_R and f_A were taken to be Morse-type pair interactions which allowed for open and close-packed structures to be favored depending on the ratio of the slopes of the repulsive and attractive pair functions [68].

Useful as this relation was, Tersoff found that in order to be able to describe the *sp*-valent group IV elements, Si and C, the bond order needed to depend on more than the local coordination. He made the bond-order term also depend on bond angles, and by 1989 parameterized his new functional form to model interactions between Si-Si, C-C, and Si-C [1]. Tersoff's model followed from Equation (55) where,

$$f_R\left(R_{ij}\right) = A_{ij}\exp\left(-\lambda_{ij}R_{ij}\right), \quad f_A\left(R_{ij}\right) = -B_{ij}\exp\left(-\gamma_{ij}R_{ij}\right), \tag{57}$$

$$b_{ij} = \chi_{ij}\left(1+L_i^{n_i}\zeta_{ij}^{n_i}\right)^{-1/2n_i}, \quad \zeta_{ij} = \sum_{k\neq i,j} g_i\left(\theta_{jik}\right) f_C\left(R_{ik}\right), \tag{58}$$

$$g_i\left(\theta_{jik}\right) = 1+\frac{c_i^2}{d_i^2} - \frac{c_i^2}{d_i^2+\left(\eta_i-\cos\theta_{jik}\right)^2}. \tag{59}$$

$f_C\left(R_{ij}\right)$ is a trigonometric cutoff function with values from one to zero. All new variables were fitting parameters except for the additional atomic index *k* and the bond angle θ_{jik} between bonds *ij* and *ik*. Only one new parameter, χ_{ij}, was introduced in this compound model versus the elemental models in order to strengthen or weaken heteropolar bonds. All other parameters were taken as either the arithmetic or geometric average of elemental values. Quite successfully, Tersoff found that even if

the parameter χ_{ij} is omitted, the B3 SiC phase is still stable to decomposition to the elemental phases. There is, however, a large discrepancy with DFT results concerning the stability and lattice constant of the B1 phase. The B1 phase using this Tersoff model is 1.5 eV/atom higher than B3 SiC compared with 0.7 eV/atom from DFT. The calculated lattice constant is 4.25 Å compared with 4.03 Å from DFT. It was proposed that since the B1 structure has considerable ionic character, this potential "might be expected to fail drastically." It was also noted that due to the short range of the potential, there is no energetic difference between cubic and hexagonal polytypes. Still, this model has withstood the test of time, setting a standard which no Si-C interatomic potential has since clearly surpassed.

In 1990, Brenner noted some discrepancies in the results from Tersoff's fit to the hydrocarbon system, namely that none of the fittings provided a good description of both the bond lengths and the stretching force constants [2]. Also, in intermediate bonding situations, for instance in radicals or conjugated systems, the bond order was interpolated resulting in unphysical intermediate bonds between a single and double bond. Interested in CVD growth, Brenner went on to develop a new variant of ATB potential to interpolate corrections to the bond order between discrete numbers of neighbors. This model for studying covalent systems was later applied to the SiC system [73]. The main development was to replace b_{ij} in Equation (55) with an average bond order $\bar{b}_{ij}$ with corrections for carbon.

$$\bar{b}_{ij} = \frac{\left(b'_{ij} + b'_{ji}\right)}{2} + F_{ij}\left(z_i^{tot}, z_j^{tot}, z_{ij}^{conj}\right), \tag{60}$$

$$b_{ij}^{'}=\left[1+\sum_{k(\neq i,j)}\left\{\begin{matrix} g_i\left(\theta_{jik}\right)f_C\left(R_{ik}\right)\exp\left(\alpha_{ijk}\left[\left(R_{ij}-R_{ij}^{'}\right)-\left(R_{ik}-R_{ik}^{'}\right)\right]\right)+ \\ \Delta_{ij}\left(z_i^{(\mu)},z_i^{(\upsilon)}\right) \end{matrix}\right\}\right]^{-\delta_i}, \quad (61)$$

where $z_i^{(\mu)}$ and $z_i^{(\upsilon)}$ are the number of species μ and υ atoms, respectively, bonded to atom i, and z_i^{tot} is the total number of neighbors $\left(z_i^{(\mu)}+z_i^{(\upsilon)}\right)$ of atom i:

$$z_i^{(\mu)}=\sum_{j(=\mu)\neq i}f_C\left(R_{ij}\right), \quad (62)$$

$$z_i^{(\upsilon)}=\sum_{j(=\upsilon)\neq i}f_C\left(R_{ij}\right), \quad (63)$$

$$z_i^{tot}=z_i^{(\mu)}+z_i^{(\upsilon)}. \quad (64)$$

z_{ij}^{conj} depends on whether a bond between carbon atoms i and j is part of a conjugated system:

$$z_{ij}^{conj}=1+\sum_{carbons\ k(\neq i,j)}f_C\left(R_{ik}\right)\varphi\left(x_{ik}\right)+\sum_{carbons\ l(\neq i,j)}f_C\left(R_{jl}\right)\varphi\left(x_{jl}\right), \quad (65)$$

where

$$\varphi\left(x_{ik}\right)=\begin{cases}1, & x_{ik}\leq 2\\ \left\{1+\cos\left[\pi\left(x_{ik}-2\right)\right]\right\}/2, & 2<x_{ik}<3,\\ 0, & x_{ik}\geq 3\end{cases} \quad (66)$$

and

$$x_{ik}=z_k^{tot}-f_C\left(R_{ik}\right). \quad (67)$$

z_{ij}^{conj} yields a continuous value as bonds break and reform and will define any bond where a neighboring carbon atom has a coordination less than four $\left(z_i^{tot}<4\right)$ as being part of a conjugated system. Δ_{ij} and F_{ij} were then taken as two- and three-dimensional

cubic splines to interpolate between values at discrete numbers of neighbors. α, $R^{'}$, and δ parameters are fitted constants.

Even with this correction to the bond order, Brenner's 1990 model failed to properly model bent and buckled structures, instead predicting linear structures. This was reportedly due to lone pairs of electrons not being explicitly treated. Also, this model did not include barriers to rotation, for instance about a C=C double bond, or long-ranged van der Waals interactions. Brenner noted the Tersoff model's failure to describe bond lengths and stretching force constants simultaneously, but also could not fit both simultaneously even with the bond-order correction and slightly more complicated forms for the repulsive and attractive pair functions. This interatomic potential did, however, address the problem with Tersoff's inherent overbinding of radicals, making it much better suited to model systems where conjugacy is important.

In 1996, Dyson and Smith extended the 1990 Brenner hydrocarbon model to include interactions with silicon [73]. Just as the bond-order correction terms Δ_{ij} and F_{ij} applied only to carbon in Brenner's model, the bond-order correction term in Dyson and Smith's model also applied only to carbon, not silicon. They found that their model underestimated the cohesive energy for close-packed structures of elemental silicon, a common problem for elemental models of silicon [74]. Once again, this model had trouble describing the preference for buckling in structures, but did include a correction for conjugacy.

In 2005, Erhart and Albe applied Tersoff's interatomic potential to the Si-C system but refit the pair parameters to dimer properties and the three-body parameters to cohesive energies and bond lengths of high symmetry crystal structures [3]. This focus on fitting the bulk phases of silicon and carbon was in opposition to the focus of Brenner as well as Dyson and Smith on molecules and surfaces. Even with the explicit aim at transferability between parameters for elemental silicon and carbon and for the compound SiC, Erhart and Albe failed to produce a single transferable parameter set. Two parameter sets for silicon were reported, one for elemental silicon, and one for silicon in SiC. Even by differentiating between elemental and compound silicon, neither of the parameter sets were able to reproduce the experimental melting point of silicon (1687 K), but instead yielded values of 2450 ± 50 K and 2150 ± 25 K.

Like Tersoff, Erhart and Albe were unable to fit the sixfold coordinated B1 structure of SiC while maintaining reasonable elastic properties for other structures. As Tersoff did in 1989 [1], Erhart and Albe accepted this deviation in the cohesive energy of the B1 structure in favor of a better description of the elastic properties of B3 SiC.

Erhart and Albe also admit that Dyson and Smith's potential [73] as well as a slightly modified version of the Tersoff potential parameterized by Gao and Weber [75] better model point defects. However, they reported that these other potentials lacked transferability to the elemental silicon and carbon systems.

The most complex form of semi-empirical ATB potential was published by Brenner et al. [68] three years before Erhart and Albe published their model for the Si-C

system. Brenner et al.'s 2002 reactive empirical bond-order (REBO) potential for hydrocarbons [68] has yet to be extended to the Si-C system.

The major development in the REBO potential was the inclusion of a π bond order in the average bond-order term. This π bond-order term has two contributions, one to describe radicals and conjugated systems, and a second contribution from the dihedral angle as depicted in Fig. 3.7:

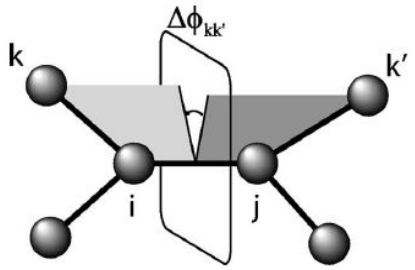

Fig. 3.7. Dihedral angle formed between atoms $kijk'$ [10].

The average bond-order term is given as

$$\bar{b}_{ij} = \frac{\left(b_{ij}^{\sigma-\pi} + b_{ji}^{\sigma-\pi}\right)}{2} + b_{ij}^{\pi}, \quad b_{ij}^{\pi} = b_{ij}^{RC} + b_{ij}^{DH}, \tag{68}$$

where b_{ij}^{RC} is the radical-conjugation contribution and b_{ij}^{DH} is the dihedral angle contribution.

$$b_{ij}^{\sigma-\pi} = \left[1 + \sum_{k(\neq i,j)} g_i'\left(\cos\left(\theta_{jik}\right)\right) f_C\left(R_{ik}\right) \exp\left(\alpha_{ijk}\right) + \Delta_{ij}\left(z_i^{(\mu)}, z_i^{(\upsilon)}\right)\right]^{-1/2}, \tag{69}$$

which is similar to Equation (61). The main differences are that $g_i'\left(\cos\left(\theta_{jik}\right)\right)$ is now a sixth-order polynomial spline and the exponential dependence is simplified to a constant. $f_C\left(R_{ik}\right)$ is still the smooth trigonometric cutoff function and $\Delta_{ij}\left(z_i^{(\mu)}, z_i^{(\upsilon)}\right)$

is a correction term fit to a bicubic spline. b_{ij}^{RC} is a slightly modified form of F_{ij}, roughly reproducing the average bond-order term in Equation (60) of the original Brenner model. The difference then comes form the b_{ij}^{DH} term, which by definition applies only to C=C double bonds, given as

$$b_{ij}^{DH} = T_{ij}\left(z_i^{tot}, z_j^{tot}, z_{ij}^{conj}\right)\left[\sum_{k(\neq i,j)}\sum_{k'(\neq i,j)}\left(1-\cos^2\left(\theta_{kijk'}\right)\right)f_C\left(R_{ik}\right)f_C\left(R_{jk'}\right)\right], \qquad (70)$$

where

$$\theta_{kijk'} = e_{jik}e_{ijk'}. \qquad (71)$$

The function $T_{ij}\left(z_i^{tot}, z_j^{tot}, z_{ij}^{conj}\right)$ is a tricubic spline, and the functions e_{jik} and $e_{ijk'}$ are unit vectors in the direction of the cross products $\boldsymbol{R}_{ji}$ x $\boldsymbol{R}_{ik}$ and $\boldsymbol{R}_{ij}$ x $\boldsymbol{R}_{jk'}$, respectively where the $\boldsymbol{R}$ terms are vectors connecting the subscripted atoms. The repulsive and attractive pair potentials also took on more complicated forms from the original models.

Overall it was reported that the Brenner et al. 2002 REBO potential for hydrocarbons had improved bond energies, lengths, and force constants compared with the 1990 Brenner potential [68]. Still they were unable to fit high-pressure phases of carbon due to the cutoff function, so they focused on the diamond and graphite phases. Given the difference between the 2002 REBO potential's average bond-order term and the average bond-order term from the 1990 Brenner potential, this family of potentials have gone so far as to include explicit π-bonding effects only by considering the dihedral angle torsional effect empirically. Still, such a correction in the REBO potential has not been applied to the Si-C system.

3.6 Environment-dependent interatomic potentials

Besides the ATB family of potentials, two other many-body potential forms have been developed for covalent materials. These include the environment-dependent interatomic potentials (EDIPs) for elemental silicon and carbon described here as well as the Vashishta 2007 potential for the compound SiC described in Section 3.7.

The EDIP family of potentials was developed using a technique of inverting DFT cohesive energy curves published in a useful form by Bazant and Kaxiras in 1996 [76]. With the goal of somehow linking quantum mechanical calculations with the development of classical interatomic potentials, Bazant and Kaxiras grouped the energy of an atom into different shells surrounding the atom in a lattice. If the interatomic potential were taken to zero at a given distance, Carlsson, Gelatt, and Ehrenreich (CGE) showed that this uniquely defines a pair potential for a given level of recursion [77]. Bazant and Kaxiras went further to show how this could be used along with a coordination dependence to define a many-body potential.

Bazant and Kaxiras noted however, that this inversion process assumes a volume-independent potential, at times "to an unphysical extreme." This is because the potential is first fit to the longest interaction distances, thereby not effectively incorporating screening. They tried to remedy this by not fitting to entire cohesive energy curves for structures, but only near equilibrium for different structures. By first studying the results from fitted pair potentials, they noticed a clear coordination dependence and presented a general way to invert DFT cohesive energy curves.

This was used by Bazant et al. in 1997 to propose functional forms for an EDIP for silicon [78]. In 1998, Justo et al. fitted this EDIP to improve the description of local bonding around defects along with bond angle and coordination distributions for molten silicon [79].

$$U = \sum_{j \neq i} f_2\left(R_{ij}, z_i\right) + \sum_{j \neq i} \sum_{k \neq i, k > j} f_3\left(\overrightarrow{R_{ij}}, \overrightarrow{R_{ik}}, z_i\right), \tag{72}$$

where f_2 and f_3 are two- and three-body functions, and z_i is calculated similarly to Equation (62), but using an exponential cutoff function instead of a trigonometric function.

$$f_2\left(R_{ij}, z_i\right) = A\left[\left(\frac{B}{R_{ij}}\right)^C - \exp\left(-\eta z_i^2\right)\right]\exp\left(\frac{\sigma}{R_{ij} - \alpha}\right), \tag{73}$$

$$f_3\left(\overrightarrow{R_{ij}}, \overrightarrow{R_{ik}}, z_i\right) = \exp\left(\frac{\gamma}{R_{ij} - \alpha} + \frac{\gamma}{R_{ik} - \alpha}\right)\Omega\left(l_{jik}, z_i\right),\ l_{jik} = \cos\theta_{jik}, \tag{74}$$

$$\Omega\left(l_{jik}, z_i\right) = \lambda\left[\left(1 - \exp\left(-\omega\left(z_i\right)\left(l_{jik} + \tau\left(z_i\right)\right)^2\right)\right) + \delta\omega\left(z_i\right)\left(l_{jik} + \tau\left(z_i\right)\right)^2\right], \tag{75}$$

$$\omega\left(z_i\right) = \omega_o \exp\left(-\varsigma z_i\right),\ \tau\left(z_i\right) = u_1 + u_2\left(u_3 \exp\left(-u_4 z_i\right) - \exp\left(-2u_4 z_i\right)\right), \tag{76}$$

where all new variables are fitting parameters. Once again the philosophy was to interpolate smoothly between areas near equilibrium.

Bazant et al. noted the peculiarity that since the two- and three-body interaction terms depended only on coordination z_i and not on both z_i and z_j, the bond strength is not symmetric or otherwise stated, $f_2\left(R_{ij}, N_i\right) \neq f_2\left(R_{ji}, N_j\right)$. They also stated that "the theory behind the model begins to break down for non-integer coordinations" due to the interpolation scheme used. Bazant et al. went so far as to include environment

dependence in both the two- and three-body functions but omitted an explicit π-bonding contribution. Instead, directionality and hybridization were addressed through empirical fitting.

For molten silicon, the potential produced a significantly more physical bond angle distribution but an unphysical density. This potential also produced metastable partially reconstructed partial dislocation configurations, an artifact of the description of the local environment during changes in coordination. Overall, however, defect energetics were improved over previous models.

In 2000, Marks applied the same EDIP formalism to elemental carbon using an adjusted coordination value [80]. While discussing thin film deposition simulations done using ATB potentials, Marks noted that these interatomic potentials did not describe the amorphous carbon phase well, significantly underestimating the sp^3 bonded fraction. Fitting the environment-dependent two- and three-body terms, Marks found the resultant EDIP for carbon to predict the sp^3 bonded fraction of tetrahedral amorphous carbon more in line with CPMD results than the ATB potentials, as well as OTB models. However, such results came at the cost of having a general absence of distances associated with double and triple carbon bonds due to the treatment of environment dependence.

Most recently, in 2010, Lucas et al. extended the EDIP model to the binary SiC proposing two models, one making use of the original C and Si EDIP models and one with an entirely new parameterizations for C, Si, and SiC [11]. Both new models

were said to be well suited for modelling point defects, but both models predicted the lowest energy silicon interstitial, the Si_Tc silicon atom in a tetrahedral site surrounded by carbon atoms, to be dynamically unstable. Agreement with the high-pressure B1 phase is also not significantly improved in comparison with the Erhart and Albe model [3] or Tersoff's model [1]. The elastic constants for B3 using the completely refit SiC model are improved relative to the Tersoff model, but not in comparison with Erhart and Albe's model. Overall, even with the flexibility of multiple parameterizations, no clear improvement was achieved.

3.7 Vashishta potential

Given the failures of the Tersoff 1989 [1] and Erhart and Albe 2005 [3] models in reasonably describing the B1 structure of SiC, Vashishta published a classical many-body potential for SiC in 2007 aiming to better describe this high-pressure phase transition as well as stacking fault energies [13]. The energy was described using a two-body term and a three-body term, as was proposed by Stillinger and Weber in 1985 [23],

$$U = \sum_{i<j} f_2\left(R_{ij}\right) + \sum_{i,j<k} f_3\left(R_{ij}, R_{ik}, \theta_{jik}\right). \tag{77}$$

The two-body term was given as follows,

$$f_2\left(R_{ij}\right) = \frac{\alpha_{ij}}{R_{ij}^{\eta_{ij}}} + \frac{Q_i Q_j}{R_{ij}} \exp\left(-R_{ij}/\lambda\right) - \frac{D_{ij}}{2R_{ij}^4} \exp\left(-R_{ij}/\xi\right) - \frac{W_{ij}}{R_{ij}^6}, \tag{78}$$

where all variables are fitting parameters except for the interatomic spacing, R_{ij}.

$$f_3\left(R_{ij}, R_{ik}, \theta_{jik}\right) = R\left(R_{ij}, R_{ik}\right) P\left(\theta_{jik}\right), \tag{79}$$

where

$$R\left(R_{ij},R_{ik}\right)=B_{jik}\exp\left(\frac{\gamma}{R_{ij}-\alpha}+\frac{\gamma}{R_{ik}-\alpha}\right)\Theta\left(\alpha-R_{ij}\right)\Theta\left(\alpha-R_{ik}\right), \tag{80}$$

$$P\left(\theta_{jik}\right)=\frac{\left(\cos\theta_{jik}-\phi\right)^2}{1+C_{jik}\left(\cos\theta_{jik}-\phi\right)^2}. \tag{81}$$

All new variables are fitting parameters except for the step function, $\Theta\left(\alpha-R_{ij}\right)$. No derivation is given for the functional forms, but the contributions in the two-body term are said to relate to steric size effects of the ions, charge transfer effects leading to Coulomb interactions, charge-dipole interactions due to the electronic polarizability of ions, and induced dipole-dipole (van der Waals) interactions. The three-body term closely resembles the Stillinger-Weber form, except that the angular function was modified from the original $P\left(\theta_{jik}\right)=\left(\cos\theta_{jik}+1/3\right)^2$.

Although this model was able to produce a reasonable description of the B1 structure and stacking fault energies, it lacks transferability to the elemental phases as all Si-Si interactions and C-C interactions are purely repulsive.

3.8 Summary

Although many of the interatomic potentials discussed in Sections 3.5-3.7 have successfully modeled the elastic and thermal properties of Si-C, their approximations in the σ bond order and failure to treat π-bonding beyond empirical rotational barriers has lead to a number of the deficiencies mentioned. As a way to provide a physical basis for the treatment of σ- and π-bonding in an interatomic potential, and in fact, to provide a physical basis for the complete functional form of an interatomic potential, DFT has been coarse-grained to TB, which has further been coarse-grained to

analytic BOPs, described in Sections 3.2-3.4. One significant step in this process is the development of a reduced TB model, the background of which was discussed in Subsection 3.3.3. Chapter 4 follows, fully defining the new reduced OTB model for the Si-C system.

4 Reduced tight binding model for silicon carbide

4.1 Introduction

For clarity and ease of implementation, all functional forms and parameters are fully described in Section 4.2, rather than being scattered throughout the Chapter. With DFT precision known to be on the order of roughly 1 meV, clearly, presenting many additional digits for fitting parameters should not be considered statistically significant with respect to the precision of the reduced OTB model. Instead, additional digits are presented to strike a balance in showing the true error function minimum in the fitting process, where very small parameter changes do indeed lower the error function value.

With the entire model reported as concisely as possible in Section 4.2, further plotting and clarification regarding the origins of the parameters is given throughout the rest of the chapter. Sections 4.3 and 4.4 describe how the distance-dependent Hamiltonian parameters and TB pair-repulsive functions are obtained from DFT. Section 4.5 then describes the fitting program used to obtain the best final quantitative accuracy. Finally a summary is given in Section 4.6.

4.2 Functional forms and parameterization

Following the general TBBM form in Subsection 3.3.2, and more specifically the reduced TB model form from Subsection 3.3.3, a reduced OTB model for the Si-C system has been parameterized. The binding energy is given by,

$$U_{binding} = U_{bond} + U_{prom} + U_{rep} + \Delta U_{at}, \tag{82}$$

where the bond energy and promotion energy are found by solving the Hamiltonian just as in the TBBM, the repulsive energy is modeled by an embedded pair function, and the change in the free atom energy ΔU_{at} is a species-dependent constant.

Just as in the TBBM, U_{bond} has two representations given as,

$$U_{bond} = \sum_{i\alpha} \int_{-\infty}^{E_F} \left(E - E_{i\alpha}^{\mu}\right) n_{i\alpha}^{\mu}\left(E\right) dE = \sum_{i \neq j} \sum_{\alpha,\beta} H_{i\alpha,j\beta}^{\mu\upsilon} \Theta_{j\beta,i\alpha}^{\mu\upsilon}, \tag{83}$$

where E_F is the Fermi energy, $E_{i\alpha}^{\mu}$ is the atomic onsite energy level, $n_{i\alpha}^{\mu}$ is the local electronic DOS, and $\Theta_{j\beta,i\alpha}^{\mu\upsilon}$ is the bond order [6].

The promotion energy is again given as,

$$U_{prom} = \sum_{i} \left(E_{ip}^{\mu} - E_{is}^{\mu}\right) \Delta N_{is}^{\mu}, \quad \Delta N_{is}^{\mu} = N_{is}^{\mu,0} - N_{is}^{\mu}, \tag{84}$$

where ΔN_{is}^{μ} is the difference in the number of electrons in the *s*-orbital with respect to the occupancy of the *s*-state of the free atom. The model has been fitted as a selfconsistent model using the LCN approximation described in Subsection 3.3.2, so again it follows that, $\Delta N_{is} = -\Delta N_{ip}$.

Following the reduced OTB model description in Subsection 3.3.3, the bond integrals $\beta_{\sigma,ij}^{\mu\upsilon}$ and $\beta_{\pi,ij}^{\mu\upsilon}$ have been parameterized using GSP functions [54],

$$\beta_{\sigma/\pi,ij}^{\mu\upsilon}\left(R_{ij}\right) = \beta_0 \left(\frac{R_0}{R_{ij}}\right)^n \exp\left\{n\left[-\left(\frac{R_{ij}}{R_c}\right)^{n_c} + \left(\frac{R_0}{R_c}\right)^{n_c}\right]\right\}. \tag{85}$$

All parameters are fitting parameters except for the experimental equilibrium nearest-neighbor distance, R_0, and the nearest-neighbor shell cutoff distance, R_c. Since the exponential term in the GSP function implicitly accounts for screening effects [54], R_c is taken as the arithmetic average of the first- and second-neighbor shell distances in the groundstate equilibrium structure given as,

$$R_c = \left(R_0 + R_2\right)/2, \tag{86}$$

where R_2 is the second-neighbor shell distance in the groundstate equilibrium structure. β_0 defines the bond integral value at the groundstate nearest-neighbor distance, R_0, and was initially taken directly from DFT-projected data as is later described in Section 4.2. The final parameterized values allow for easy comparison between the elemental and binary equilibrium groundstate structures.

In order to keep the model as local as possible, $\beta_{\sigma,ij}^{\mu\upsilon}$ and $\beta_{\pi,ij}^{\mu\upsilon}$ are replaced by an analytic parameter-free tail function developed by Jan Gehrmann which matches the function value and first derivative at a certain interatomic distance R_1 and smoothly takes the function value and first derivative to zero by an interatomic distance R_{cut}. As this is a nearest-neighbor model, R_1 was defined to be the largest nearest-neighbor distance from the fitted DFT projection data, and R_{cut} was varied discretely by 0.1 Angstrom to be as short as possible while avoiding significant kinks in binding energy curves from second-neighbor effects. The tail function χ is given by,

$$\chi^{\mu\upsilon}_{\sigma/\pi,ij}\left(R_{ij}\right)=\frac{B_0}{2}\exp\left\{B_1\frac{R_{ij}-R_1}{B_0}\right\}\left[1-\cos\left(\pi\frac{R_{ij}-R_{cut}}{R_{cut}-R_1}\right)\right],$$
$$B_0=\beta^{\mu\upsilon}_{\sigma/\pi,ij}\left(R_1\right), \tag{87}$$
$$B_1=\left.\frac{d\beta^{\mu\upsilon}_{\sigma/\pi,ij}\left(R_{ij}\right)}{dR_{ij}}\right|_{R_1}.$$

The bond integral parameters are given in Table 4.1,

	β_0	R_0	n	R_c	n_c	R_1	R_{cut}
$\beta^{SiC}_{\sigma,ij}$	-7.775592652	1.888	1.035493729	2.4855	3.824344087	2.38	3.8
$\beta^{SiC}_{\pi,ij}$	-1.513841204	1.888	3.001507291	2.4855	8.951758564	2.38	3.8
$\beta^{CC}_{\sigma,ij}$	-10.44200309	1.545	1.23871924	2.034	4.391704341	1.7	2.8
$\beta^{CC}_{\pi,ij}$	-2.29460689	1.545	1.340786373	2.034	3.247385974	1.7	2.8
$\beta^{SiSi}_{\sigma,ij}$	-5.823739707	2.333	1.470975347	3.0715	3.359541894	3.0	4.3
$\beta^{SiSi}_{\pi,ij}$	-1.330342431	2.333	5.066060479	3.0715	5.53617E-05	2.8	4.3

Table 4.1. Reduced OTB bond integral parameters in eV and Angstrom.

The reduced TB parameters $p^{\mu(\upsilon)}_{\sigma,ij}$ have been parameterized using the form,

$$p^{\mu(\upsilon)}_{\sigma,ij}\left(R_{ij}\right)=\frac{1}{1+\left[c^{\mu(\upsilon)}_{ij}\exp\left(-\gamma^{\mu(\upsilon)}_{ij}R_{ij}\right)\right]}, \tag{88}$$

where $c^{\mu(\upsilon)}_{ij}$ and $\gamma^{\mu(\upsilon)}_{ij}$ are fitting parameters. The parameters are given in Table 4.2.

	$c^{\mu(\upsilon)}_{ij}$	$\gamma^{\mu(\upsilon)}_{ij}$
$p^{Si(C)}_{\sigma,ij}$	19.45595525	2.018448047
$p^{C(Si)}_{\sigma,ij}$	4.195920452	0.942578999
$p^{C(C)}_{\sigma,ij}$	1.246258282	0.36217484
$p^{Si(Si)}_{\sigma,ij}$	2.150115326	0.593162873

Table 4.2. Reduced OTB hybrid orbital parameters.

For future transferability with other elements and the potential inclusion of selfconsistent charge transfer, the onsite energy levels were taken from Harrison, 2004 [37] with E_p and E_s of -7.59 eV and -14.79 eV for silicon and -11.07 eV and -19.38 for carbon. When achieving selfconsistency through LCN for the current model, the onsite energy level splitting on a given atom is kept fixed, and the atomic levels shift together rigidly.

The repulsive energy is given as,

$$
\begin{aligned}
&U_{rep} = \sum_i f\left(\sum_{j\neq i} \Phi_{ij}^{\mu\upsilon}\left(R_{ij}\right)\right), \\
&f\left(x\right) = x^{n_1}, \\
&\Phi_{ij}^{\mu\upsilon}\left(R_{ij}\right) = \Phi_{core,ij}^{\mu\upsilon}\left(R_{ij}\right) + \Phi_{GSP,ij}^{\mu\upsilon}\left(R_{ij}\right), \\
&\Phi_{core,ij}^{\mu\upsilon}\left(R_{ij}\right) = \frac{b}{\left(R_{ij}\right)^{m_1}} \exp\left(-qR_{ij}\right), \\
&\Phi_{GSP,ij}^{\mu\upsilon}\left(R_{ij}\right) = \Phi_0 \left(\frac{R_0}{R_{ij}}\right)^m \exp\left\{m\left[-\left(\frac{R_{ij}}{D_c}\right)^{m_c} + \left(\frac{R_0}{D_c}\right)^{m_c}\right]\right\},
\end{aligned}
\tag{89}
$$

similar to the form used by the Ames group [5, 7] except for the simplification of the embedding function $f\left(x\right)$ and the addition of a hard-core screened Yukawa potential, $\Phi_{core}\left(R_{ij}\right)$. A GSP function [54] is used for the form of the pair-repulsive function, $\Phi_{GSP}\left(R_{ij}\right)$. The hard-core screened Yukawa potential is replaced by the tail function in Equation (87) starting at an interatomic distance of D_1 up to a cutoff distance of $D_{1,cut}$, and the GSP function is replaced by the tail function in Equation (87) starting at an interatomic distance of D_2 up to a cutoff distance of $D_{2,cut}$. The

power-law embedding powers n_1 were fit as 0.8988113856 and 0.5659509851 for carbon and silicon respectively. The hard-core screened Yukawa parameters are given in Table 4.3.

	b	m_1	q	D_1	$D_{1,cut}$
$\Phi_{core,ij}^{SiC}$	4749.32651	1.0	4.088699389	1.35	1.7
$\Phi_{core,ij}^{CC}$	1854.002758	1.0	4.803021409	1.05	1.4
$\Phi_{core,ij}^{SiSi}$	30944.00735	8.344279279	1.18623111	1.65	2.0

Table 4.3. Hard-core screened Yukawa repulsive parameters.

The GSP pair-repulsive parameters are given in Table 4.4.

	Φ_0	R_0	m	D_c	m_c	D_2	$D_{2,cut}$
$\Phi_{GSP,ij}^{SiC}$	9.144298686	1.888	2.169688175	2.4855	4.616293959	3.65	3.8
$\Phi_{GSP,ij}^{CC}$	9.096793463	1.545	2.972578612	2.145527576	7.484785565	2.65	2.8
$\Phi_{GSP,ij}^{SiSi}$	20.80116671	2.333	4.669937808	3.0715	2.395995935	4.15	4.3

Table 4.4. GSP pair-repulsive parameters.

For the case of carbon-carbon pair-repulsive energies, when allowed to vary, the parameter D_c remained in the physical region between first- and second-shell distances and greatly improved the fit for higher-coordinated structures. As such, D_c is a fitted parameter for the carbon-carbon pair-repulsive function. When allowed to vary, D_c tended to values outside the physical region for silicon-silicon and silicon-carbon interactions and was therefore kept fixed.

The change in the free atom energy is given by,

$$\Delta U_{at} = \sum_i \Delta E_{i,at}^{\mu}, \tag{90}$$

where $\Delta E^{\mu}_{i,at}$ is a constant. If the reduced OTB model were able to exactly reproduce the binding energies of the spin-polarized DFT reference binding energies, the free atom energies would be zero. Since the spin-polarization degree of freedom is absent in the current reduced OTB model, a positive value for $\Delta E^{\mu}_{i,at}$ could be justified. In different test fits, both positive and negative values were found for $\Delta E^{\mu}_{i,at}$. As the fitted value for $\Delta E^{C}_{i,at}$ tended to be large and negative, $\Delta E^{C}_{i,at}$ was fixed to zero so as to best reproduce the reference binding energies. $\Delta E^{Si}_{i,at}$ tended to a physical positive value, and since it also improved the results, it was allowed to vary in the final parameterization. The final value for ΔE^{Si}_{i} was 0.2688170861 eV.

4.3 Extracting Hamiltonian parameters from DFT

In an effort to obtain the most sensible physical values for the parameters in the model presented in the previous section and to minimize any possible over fitting, as many parameters as possible in the model have been derived from DFT. The two-centre bond integrals $ss\sigma$, $sp\sigma$, $ps\sigma$, $pp\sigma$, and $pp\pi$ have been obtained from DFT using the local orbital projection method from our collaborator Martin Reese working under Matous Mrovec and Christian Elsasser in Freiburg, Germany [81]. So long as Equation (28) from the reduced TB model Subsection 3.3.3 is used to transform the hybrid orbital basis function values back to the traditional OTB projections, any parameterization of reduced TB parameters $\beta^{\mu\upsilon}_{\sigma,ij}$ and $p^{\mu(\upsilon)}_{\sigma,ij}$ will fulfill the reduced TB condition of having only a single σ bond order $\Theta^{\upsilon\mu}_{\sigma,ji}$ contribution to the bond energy.

Following a suggestion from David Pettifor, effective $\beta_{\sigma,ij}^{\mu\upsilon}$ DFT projections were defined so as to give the same second moment, or root mean squared width, of the OTB DOS, and hence keep the TB electronic structure as closely related to the DFT calculations as possible. The proposed definition for the transformation from the traditional *s*- and *p*-basis to the hybrid orbital basis is given by,

$$\beta_{\sigma,ij}^{\mu\upsilon}\left(R_{ij}\right) \equiv -\sqrt{\left[ss\sigma_{ij}^{\mu\upsilon}\left(R_{ij}\right)\right]^2+\left[sp\sigma_{ij}^{\mu\upsilon}\left(R_{ij}\right)\right]^2+\left[ps\sigma_{ij}^{\mu\upsilon}\left(R_{ij}\right)\right]^2+\left[pp\sigma_{ij}^{\mu\upsilon}\left(R_{ij}\right)\right]^2}. \quad (91)$$

Depending on how the reduced TB approximation Equation (20) is substituted into Equation (28), a number of different possible definitions can be derived for $p_{\sigma,ij}^{\mu(\upsilon)}$. So as to make use of all the DFT-projected data, the author of this thesis suggested an average $p_{\sigma,ij}^{\mu(\upsilon)}$ be defined as,

$$p_{\sigma,ij}^{\mu(\upsilon)}\left(R_{ij}\right) = \frac{1}{2}\left\{\frac{1}{1+\left[sp\sigma_{ij}^{\mu\upsilon}\left(R_{ij}\right)/pp\sigma_{ij}^{\mu\upsilon}\left(R_{ij}\right)\right]^2}+\frac{1}{1+\left[ss\sigma_{ij}^{\mu\upsilon}\left(R_{ij}\right)/ps\sigma_{ij}^{\mu\upsilon}\left(R_{ij}\right)\right]^2}\right\}. \quad (92)$$

Intuitively, this definition appears sensible given that $p_{\sigma,ij}^{\mu(\upsilon)}$ indicates the relative *p*-orbital character of the σ bonding hybrid orbital in Equation (18). A stronger *p*-orbital contribution from atom *i* would correspond to larger $pp\sigma_{ij}^{\mu\upsilon}\left(R_{ij}\right)$ and $ps\sigma_{ij}^{\mu\upsilon}\left(R_{ij}\right)$ projected values compared with $sp\sigma_{ij}^{\mu\upsilon}\left(R_{ij}\right)$ and $ss\sigma_{ij}^{\mu\upsilon}\left(R_{ij}\right)$ projected values in Equation (92), increasing the magnitude of $p_{\sigma,ij}^{\mu(\upsilon)}$ towards the maximum value of 1.

Again, the reduced TB parameter $\beta_{\pi,ij}^{\mu\upsilon}$ is defined as,

$$\beta_{\pi,ij}^{\mu\upsilon}\left(R_{ij}\right) \equiv pp\pi_{\pi,ij}^{\mu\upsilon}\left(R_{ij}\right), \quad (93)$$

allowing for the DFT-projected data to be fit directly.

All the transformed data is presented in the following three sections along with the final fits. All the fitted parameters were given in Section 4.2.

4.3.1 Silicon-Carbon

Following the definitions given in Equations (91) and (93), the transformed projected data and final fitted data for $\beta_{\sigma,ij}^{SiC}$ and $\beta_{\pi,ij}^{SiC}$ interactions are shown in Fig. 4.1.

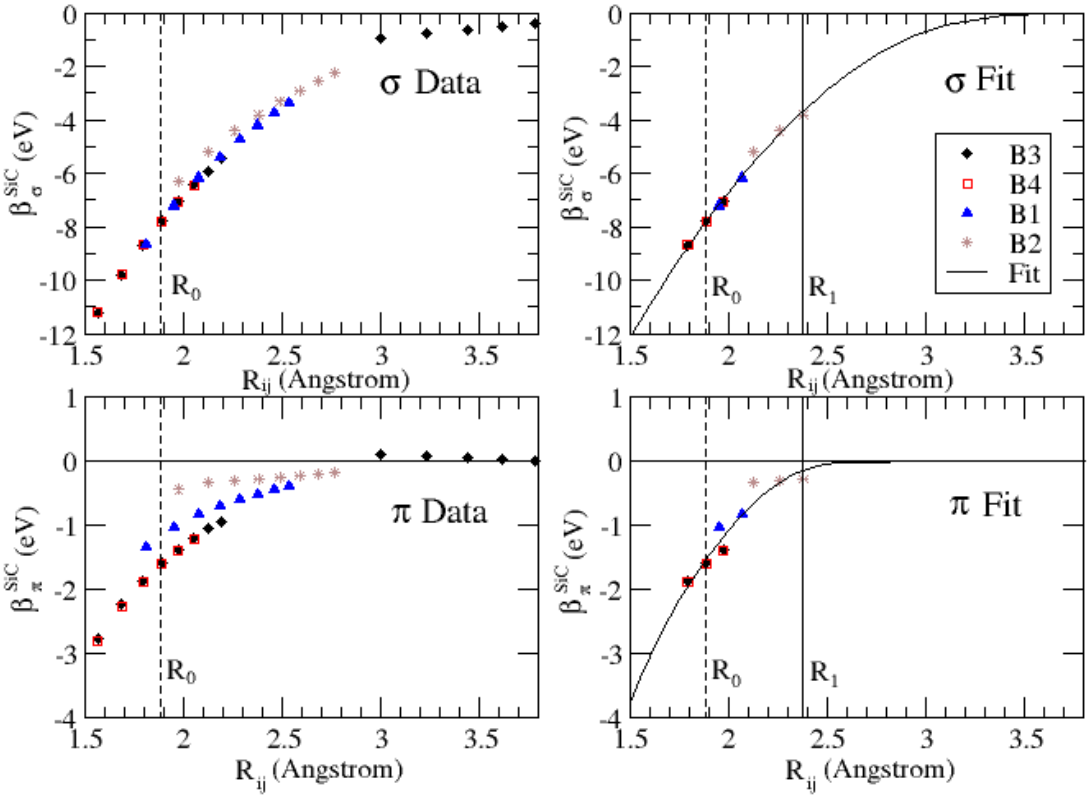

Fig. 4.1. DFT-projected OTB parameters for Si-C transformed to $\beta_{\sigma,ij}^{SiC}\left(R_{ij}\right)$ on top and $\beta_{\pi,ij}^{SiC}\left(R_{ij}\right)$ on bottom. All the raw data is shown on the left and the final fitted data with the fitted curve is shown on the right. Note the dashed lines at R_0 provide a reference of the nearest-neighbor distance of the groundstate structure at equilibrium and the solid line at R_1 provides a reference of the distance at which the tail function begins to take the fitted function smoothly to zero.

The longer-ranged data shown in Fig. 4.1 from roughly 3 to 3.8 Angstrom corresponds to 3rd neighbor interactions in the B3 structure. Note that for binary compounds, second-neighbor interactions tend to be homonuclear interactions, hence the gap in the data around 2.9 Angstrom in Fig. 4.1. The best model came from fitting the near-equilibrium points highlighted on the right side in Fig. 4.1, substituting the tail function Equation (87) from 2.38 to 3.8 Angstrom. Given the small function values for $\beta_{\pi,ij}^{SiC}\left(R_{ij}\right)$ after roughly 2.9 Angstrom, a shorter final cutoff distance could be used. However, to maintain consistency with $\beta_{\sigma,ij}^{SiC}\left(R_{ij}\right)$, 3.8 Angstrom was used. The graphs on the right of Fig. 4.1 show clearly how the distance at which the tail function is applied, R_1, was chosen to coincide with the last fitted data point, avoiding extrapolation errors and making the model as smooth and short-ranged as possible.

As could be expected, structures with different screening tend to show different slopes in the projected data as was discussed and shown in Fig. 1 in reference [49]. This is seen particularly in the $\beta_{\pi,ij}^{\mu\upsilon}$ data on the bottom of Fig. 4.1 in comparison with the fitted GSP function. This is a natural result of making the two-centre Slater-Koster approximation, with similar behavior shown later in the elemental cases.

Noting the different y-axis scales, the $\beta_{\pi,ij}^{SiC}$ interaction is significantly smaller in magnitude than the $\beta_{\sigma,ij}^{SiC}$ interaction around equilibrium, consistent with the strong σ-bonding character noted for the Si-C system often discussed in chemistry.

Following the definition given in Equation (92), the transformed projected data and final fits for $p_{\sigma,ij}^{Si(C)}$ and $p_{\sigma,ij}^{C(Si)}$ are shown in Fig. 4.2.

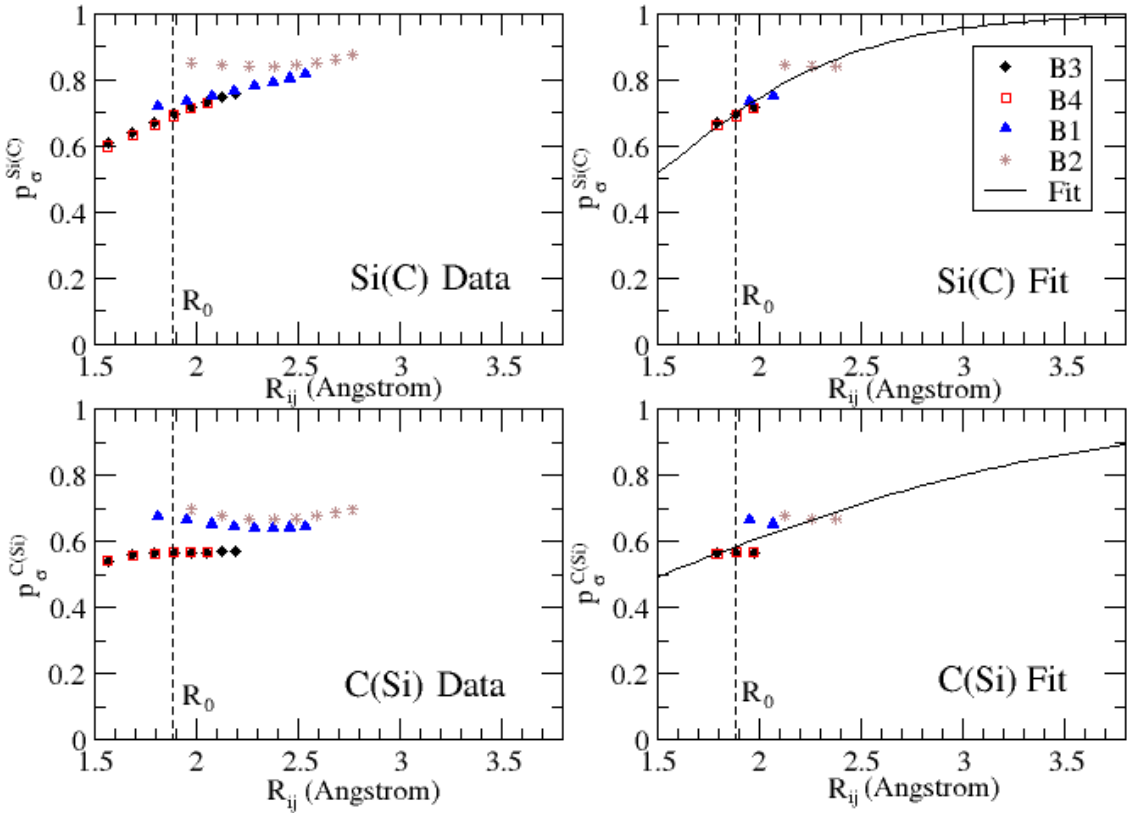

Fig. 4.2. DFT-projected OTB parameters for Si-C transformed to $p_{\sigma,ij}^{Si(C)}\left(R_{ij}\right)$ on top and $p_{\sigma,ij}^{C(Si)}\left(R_{ij}\right)$ on bottom.

As screening affects the second-neighbor interactions, data only from nearest-neighbor interactions is shown in Fig. 4.2. Again, the best model came from fitting the near-equilibrium points of the Si-C data, and the functional form given in Equation (88) was used to fit the curves of the right side of Fig. 4.2. Following the discussion in Subsection 3.3.3 on reduced TB, the larger magnitude values for $p_{\sigma,ij}^{Si(C)}\left(R_{ij}\right)$ in comparison with $p_{\sigma,ij}^{C(Si)}\left(R_{ij}\right)$ indicate a slightly stronger p-orbital character in the σ-bonding hybrid orbital on a silicon atom surrounded by carbon atoms in comparison with the corresponding orbital on a carbon atom surrounded by

silicon atoms.

The fitted functions shown in Figs. 4.1 and 4.2 fully describe the distance-dependent pairwise silicon-carbon Hamiltonian parameters given in Section 4.2. For all silicon-carbon Hamiltonian parameters, using a consistent methodology of fitting to near-equilibrium data points yielded the best model, although fitting to all the available data and to only the B3 structure data was also tested.

4.3.2 Carbon-Carbon

The transformed projected data and fits for elemental $\beta_{\sigma,ij}^{CC}$ and $\beta_{\pi,ij}^{CC}$ interactions are shown in Fig. 4.3.

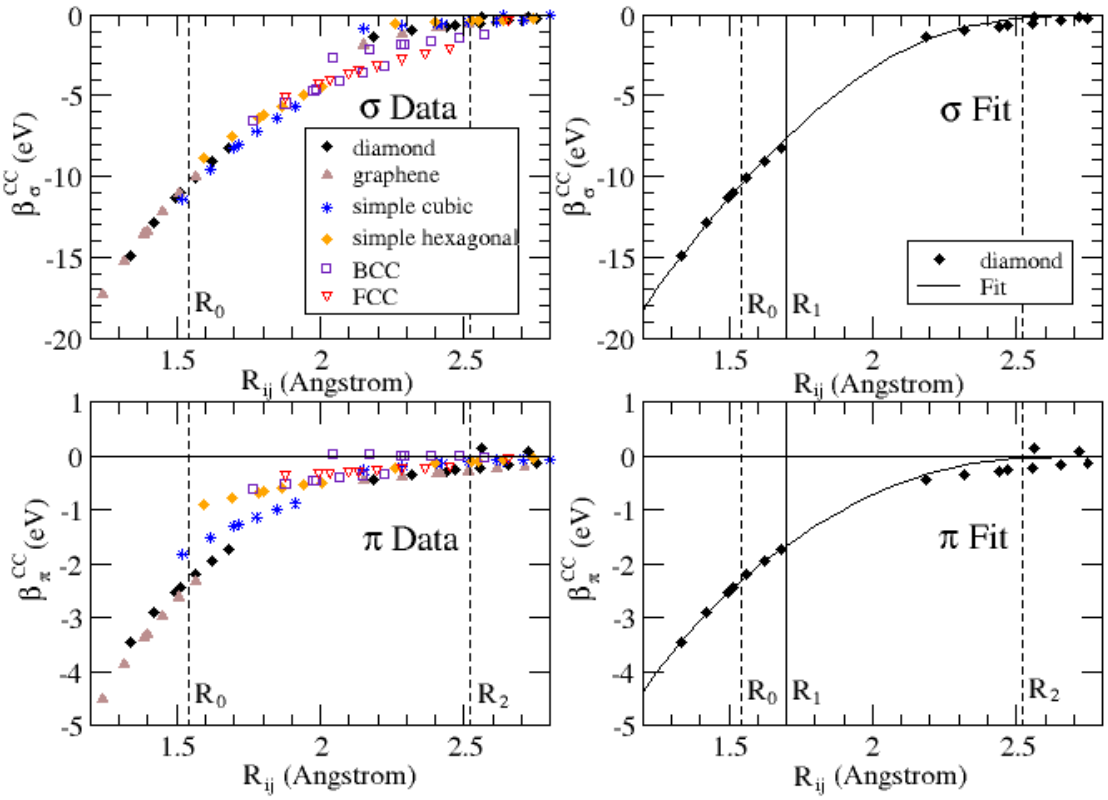

Fig. 4.3. DFT-projected OTB parameters for C transformed to $\beta_{\sigma,ij}^{CC}\left(R_{ij}\right)$ on top and $\beta_{\pi,ij}^{CC}\left(R_{ij}\right)$ on bottom. Note, additional dashed lines at R_2 provide a reference of the second-nearest-neighbor distance of the groundstate structure at equilibrium.

The spread in the data around 2.2 Angstrom, particularly for $\beta_{\sigma,ij}^{CC}\left(R_{ij}\right)$, shows the significance of screening on the second neighbors as the smaller magnitude values are second-neighbor contributions from simple cubic, diamond, and graphene structures and the larger magnitude values are nearest-neighbor contributions from BCC and FCC structures. Clearly, the nearest-neighbor data is much less structure-dependent. Similar to the Si-C interactions shown in Fig. 4.1, the $\beta_{\pi,ij}^{CC}\left(R_{ij}\right)$ interactions are more structure-dependent and smaller in magnitude than $\beta_{\sigma,ij}^{CC}\left(R_{ij}\right)$ interactions. In contrast, the relative magnitudes for both $\beta_{\sigma,ij}^{CC}\left(R_{ij}\right)$ and $\beta_{\pi,ij}^{CC}\left(R_{ij}\right)$ for elemental C in Fig. 4.3 are larger than for binary Si-C in Fig. 4.1 about their respective groundstate equilibrium distances. The best model came from fitting the diamond data highlighted on the right of Fig. 4.3 and substituting the tail function Equation (87) from 1.7 to 2.8 Angstrom.

Following the definition given in Equation (92), the transformed projected data and final fit for $p_{\sigma,ij}^{C(C)}$ are shown in Fig. 4.4.

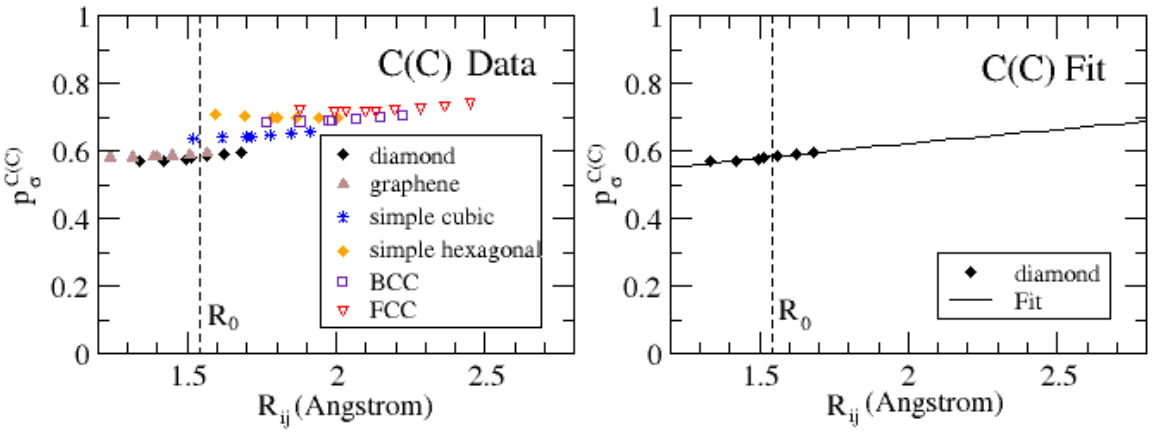

Fig. 4.4. DFT-projected OTB parameters for C transformed to $p_{\sigma,ij}^{C(C)}\left(R_{ij}\right)$.

Similar to the C(Si) data in Fig. 4.2, the C(C) data is somewhat structure-dependent but rather distance-independent, and the magnitudes at equilibrium for the groundstate structures are very close. This indicates that the *p*-orbital character of the σ-bonding hybrid orbital for carbon is sensitive to the geometry of different crystal structures but is less sensitive to expansion, compression, or surrounding species. The best model came from fitting the diamond data highlighted on the right of Fig. 4.4 with the functional form given in Equation (88).

The fitted functions shown in Figs. 4.3 and 4.4 describe the distance-dependent pairwise carbon-carbon Hamiltonian parameters given in Section 4.2. For all carbon-carbon Hamiltonian parameters, using a consistent methodology of fitting to diamond data points yielded the best model, although fitting to all the available data and to near equilibrium data points was also tested.

4.3.3 Silicon-Silicon

The transformed projected data and fits for $\beta_{\sigma,ij}^{SiSi}$ and $\beta_{\pi,ij}^{SiSi}$ interactions are shown in Fig. 4.5. Again, the $\beta_{\sigma,ij}^{SiSi}\left(R_{ij}\right)$ interaction is much stronger than the $\beta_{\pi,ij}^{SiSi}\left(R_{ij}\right)$ interaction and the trend is established that silicon shows the smallest magnitude values overall in comparison with intermediate binary Si-C values and large elemental C values. The nearest-neighbor data for $\beta_{\sigma,ij}^{SiSi}\left(R_{ij}\right)$ shows structure dependence with data spread of roughly 1 eV across the entire range from around 2.0 Angstrom to 2.8 Angstrom. The discontinuity in the data around 3.0 Angstrom again shows the significance of screening on the second neighbors as the smaller magnitude values are second-neighbor contributions.

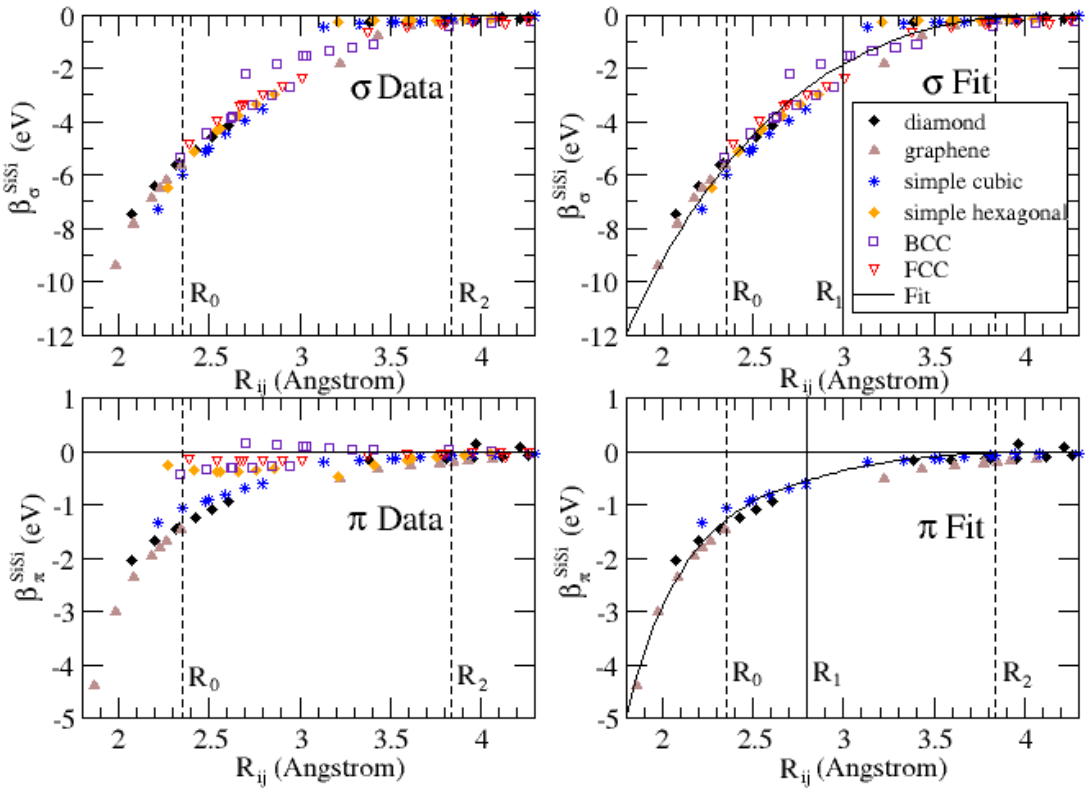

Fig. 4.5. DFT-projected OTB parameters for Si transformed to $\beta_{\sigma,ij}^{SiSi}\left(R_{ij}\right)$ on top and $\beta_{\pi,ij}^{SiSi}\left(R_{ij}\right)$ on bottom.

Structure dependence is even more pronounced for $\beta_{\pi,ij}^{SiSi}\left(R_{ij}\right)$, as was the case for the binary Si-C and elemental C. The Si data, however, shows different behavior for the higher-coordinated, higher-energy simple hexagonal, BCC, and FCC structures, in comparison with the diamond, graphene, and simple cubic structures. The best model came from fitting all the $\beta_{\sigma,ij}^{SiSi}\left(R_{ij}\right)$ data shown in Fig. 4.5, substituting the tail function Equation (87) from 3.0 to 4.3 Angstrom, but then fitting just the lower-coordination diamond, graphene, and simple cubic data for $\beta_{\pi,ij}^{SiSi}\left(R_{ij}\right)$, substituting the tail function from 2.8 to 4.3 Angstrom.

Following the definition given in Equation (92), the transformed projected data and fit for $p_{\sigma,ij}^{Si(Si)}$ is shown in Fig. 4.6.

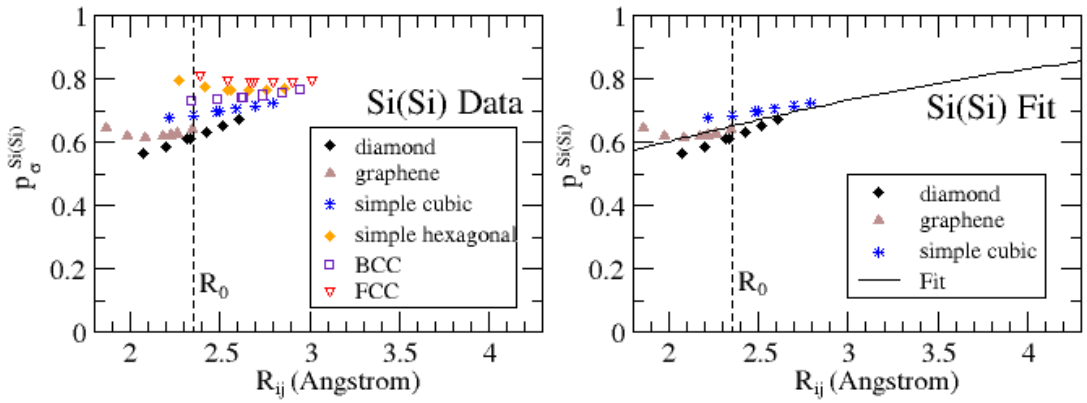

Fig. 4.6. DFT-projected OTB parameters for Si transformed to $p_{\sigma,ij}^{Si(Si)}\left(R_{ij}\right)$.

The Si(Si) data in Fig. 4.6 shows similar trends in distance dependence and structure dependence as was found for Si(C) in Fig. 4.2. The groundstate equilibrium projected data points for Si(Si) and Si(C) are also very close in value, as was the case for C(C) and C(Si) values. Overall, for silicon, this indicates significant volume-/distance- and crystal geometry- dependence but perhaps weaker species dependence. The best model came from fitting the diamond, graphene, and simple cubic data with the functional form given in Equation (88) as highlighted on the right of Fig. 4.6.

The fitted functions shown in Figs. 4.5 and 4.6 describe the distance-dependent pairwise silicon-silicon Hamiltonian parameters given in Section 4.2. As the BCC, FCC, and simple hexagonal data tended to show different behavior, particularly for $\beta_{\pi,ij}^{SiSi}\left(R_{ij}\right)$, both $\beta_{\pi,ij}^{SiSi}\left(R_{ij}\right)$ and $p_{\sigma,ij}^{Si(Si)}\left(R_{ij}\right)$ were fitted to diamond, graphene and simple cubic data. There was less structure dependence for $\beta_{\sigma,ij}^{SiSi}\left(R_{ij}\right)$ so fitting to all

the data points yielded a sensible, smooth curve. Other methodologies for fitting through the data points shown in Figs. 4.5 and 4.6 were tested but yielded final fitted models with significantly larger errors.

4.4 Extracting tight binding pair-repulsive energies from DFT

Before repulsive parameters are allowed to vary during a fitting procedure, sensible initial values can be obtained by extracting the TB pair-repulsive energy from reference DFT binding energies. Initially keeping the constant-shift energy contribution ΔU_{at} equal to zero, the TBBM energy is given again as,

$$U_{binding}^{TB} = U_{bond}^{TB} + U_{prom}^{TB} + U_{rep}^{TB}. \tag{94}$$

U_{bond}^{TB} and U_{prom}^{TB} are defined by our Hamiltonian parameters described in Section 4.2. Making use of reference DFT binding energies $U_{binding}^{DFT}$, an effective target U_{rep}^{TB} can be calculated as,

$$U_{rep}^{TB} = U_{binding}^{DFT} - \left(U_{bond}^{TB} + U_{prom}^{TB} \right). \tag{95}$$

Making a nearest-neighbor approximation the TB pair-repulsive energies can then be calculated,

$$\Phi_{rep}^{TB} = \frac{U_{rep}^{TB}}{\left(N_{at} \right)\left(z \right)}, \tag{96}$$

where N_{at} is the number of atoms and z is the nearest-neighbor coordination number for a given structure. This target Φ_{rep}^{TB} can then be plotted versus the nearest-neighbor distance to obtain $\Phi_{rep}^{TB}\left(R_{ij} \right)$. Since second-neighbor repulsive interactions are not

taken into account the error in this approximation increases as second-neighbor contributions increase, i.e. as structures are compressed.

The target $\Phi_{rep}^{TB}\left(R_{ij}\right)$ data for carbon-carbon interactions along with a fitted GSP function [54] are shown in Fig. 4.7.

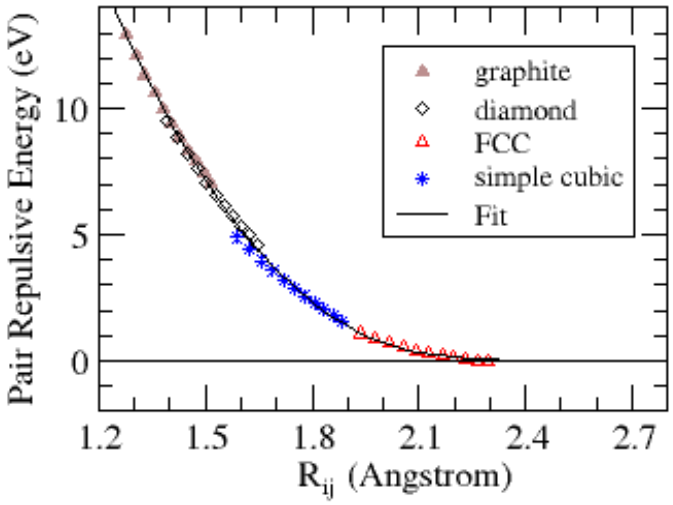

Fig. 4.7. Carbon-carbon pair-repulsive energies $\Phi_{rep}^{TB}\left(R_{ij}\right)$ as defined by Equation (96) fitted with a GSP function.

The equilibrium nearest-neighbor distances or bond lengths for carbon show a rather large spread, for instance in comparison to silicon; hence, the target carbon-carbon pair-repulsive energies about equilibrium for select simple structures span a rather large spectrum of R_{ij}, here from roughly 1.3 to 2.3 Angstrom. The largest errors in the fitted GSP function are in the region of overlap between the diamond and simple cubic structures at roughly 1.6 Angstrom. At that distance, the fitted pair-repulsive function is too weak for the diamond structure and too strong for the simple cubic structure with errors on the order of hundreds of meV per pair. The pair-repulsive

function from Fig. 4.7 serves as a sensible starting repulsive function, correctly reproducing the order of magnitude of the DFT binding energies shown in Fig. 4.8.

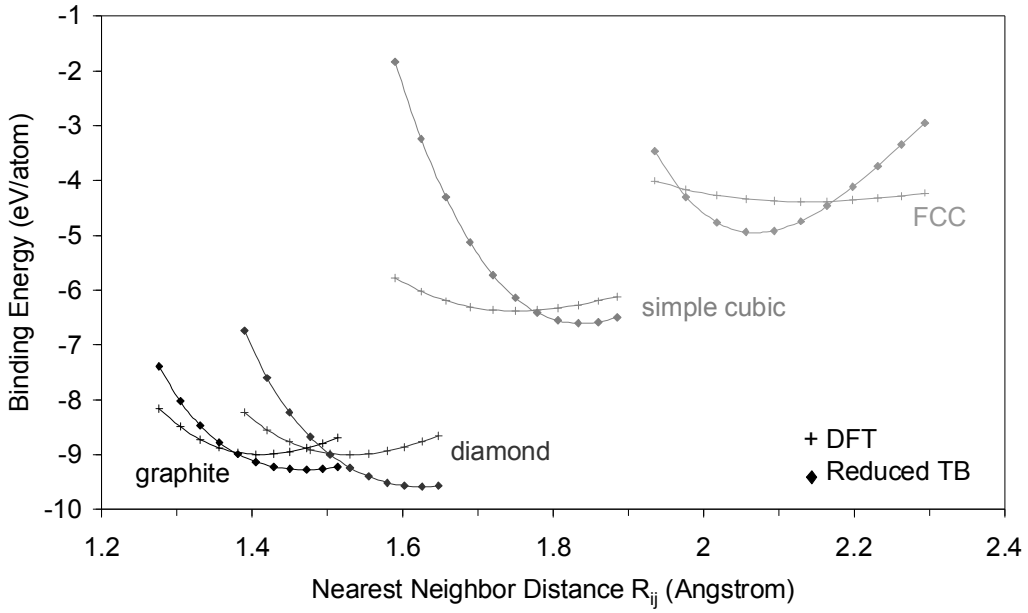

Fig. 4.8. Reduced TB elemental carbon binding energies using the pair-repulsive function from Fig. 4.7 compared with DFT reference energies.

As discussed, the largest errors from the curve in Fig. 4.7 occur around 1.6 Angstrom. All structures have increasing error under compression as the second-nearest-neighbor contributions, which are not included in Equation (96), become more significant. Nevertheless, much of the DFT structural ordering is already reproduced.

The target $\Phi_{rep}^{TB}\left(R_{ij}\right)$ data for silicon-silicon interactions along with a fitted GSP function [54] are shown in Fig. 4.9.

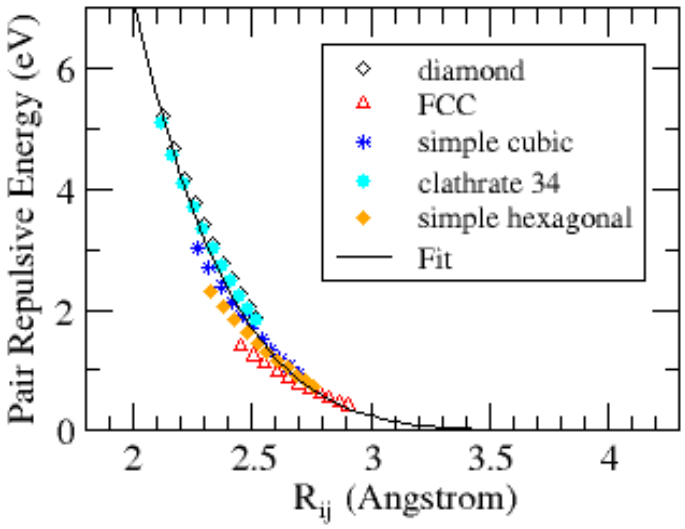

Fig. 4.9. Silicon-silicon pair-repulsive energies.

The equilibrium nearest-neighbor distances or bond lengths for elemental silicon are rather insensitive to coordination number or structure; hence, the target silicon-silicon pair-repulsive energies about equilibrium for select structures span a smaller spectrum of R_{ij}, from roughly 2.1 to 2.9 Angstrom. The largest errors in the fitted GSP function are in the region of overlap between the various structures around 2.4 Angstrom. At that distance, the fitted pair-repulsive function is too weak for the diamond structure and too strong for the FCC structure with errors on the order of hundreds of meV per pair. The pair-repulsive function from Fig. 4.9 serves as a sensible starting repulsive function, correctly reproducing the order of magnitude of the DFT binding energies shown in Fig. 4.10.

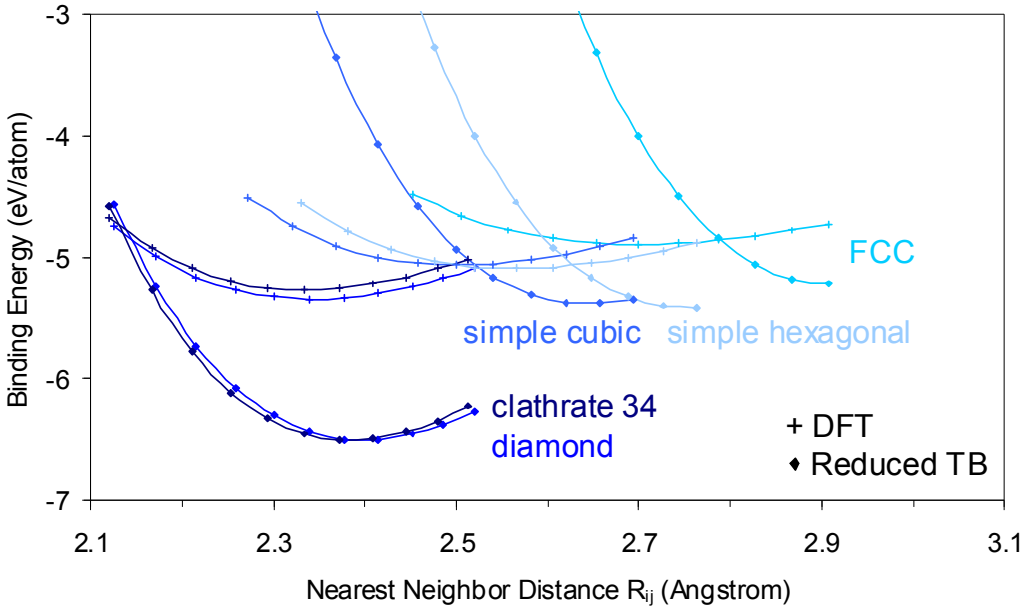

Fig. 4.10. Reduced TB elemental silicon binding energies using the pair-repulsive function from Fig. 4.9 compared with DFT reference energies.

As discussed, the largest errors from the curve in Fig. 4.9 occur around 2.4 Angstrom. All structures have increasing error under compression as the second-nearest-neighbor contributions, which are not included in Equation (96), become more significant. Again, much of the DFT structural ordering is already reproduced with this simple extraction of the pair-repulsive energies. The target $\Phi_{rep}^{TB}\left(R_{ij}\right)$ data for silicon-carbon interactions along with a fitted GSP function [54] are shown in Fig. 4.11.

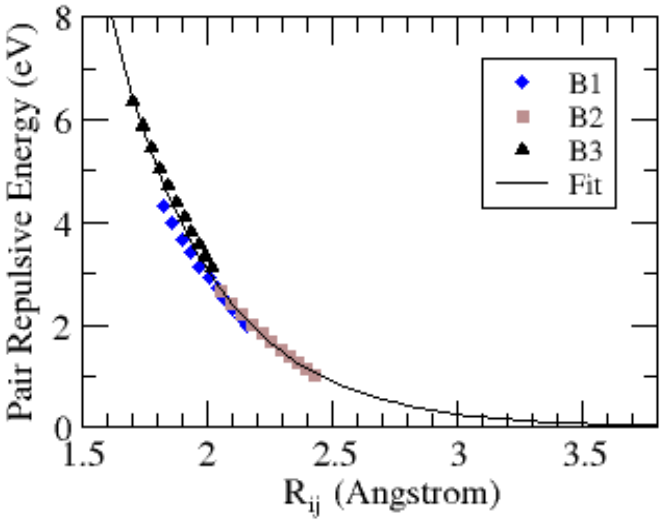

Fig. 4.11. Silicon-carbon pair-repulsive energies.

The target silicon-carbon pair-repulsive energies in Fig. 4.11 about equilibrium for select structures span a spectrum of R_{ij} from roughly 1.7 to 2.4 Angstrom. The largest errors in the fitted GSP function are in the region of overlap between the B1 and B3 structures around 1.9 Angstrom. At that distance, the fitted pair-repulsive function is too weak for the B3 structure and too strong for the B1 structure with errors on the order of 100 meV per pair. Using the pair-repulsive function from Fig. 4.11 as well as the elemental pair-repulsive functions, the TB binding energies in comparison with DFT reference values are shown in Fig. 4.12.

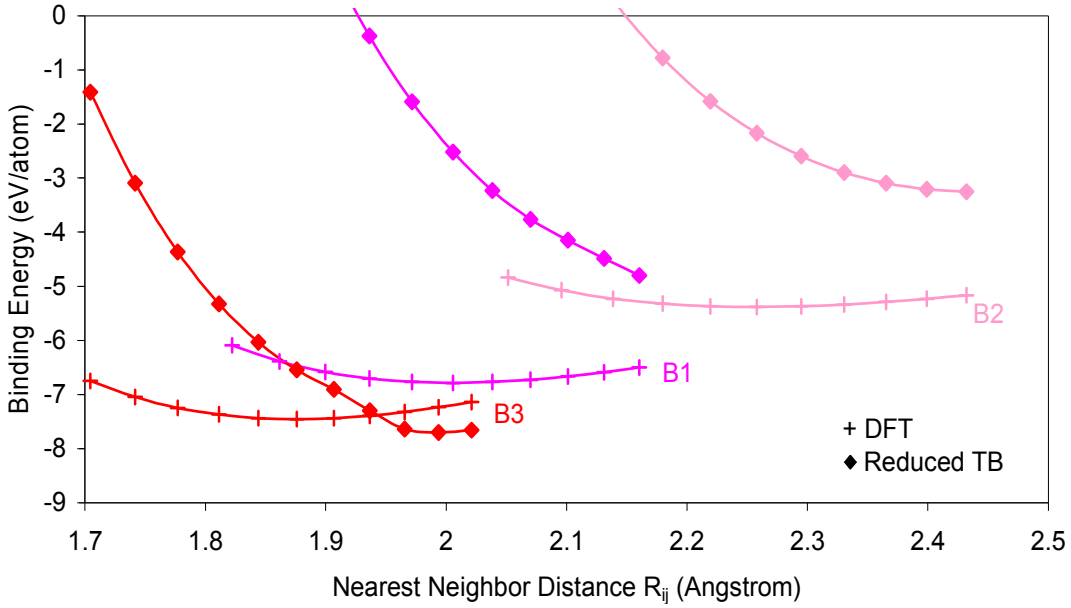

Fig. 4.12. Reduced TB binary silicon carbide binding energies, using the pair-repulsive function from Fig. 4.11 along with the earlier elemental pair-repulsive functions, compared with DFT reference energies.

As second-neighbor silicon-silicon interactions in the binary silicon carbide tend to be closer-ranged than second-neighbor interactions in elemental structures, there is a significant error in the nearest-neighbor approximation in Equation (96). The pair

silicon-silicon repulsive interactions from second neighbors are of significant magnitude, rendering reduced TB binding energies which are too small in comparison to DFT. Also the non-zero value of the fitted GSP function near the cutoff shown in Fig. 4.11 yields a small kink in the B3 structure between 1.9 and 2.0 Angstrom due to small third-neighbor effects. Nevertheless, the structural ordering and order of magnitude of the binding energies are still in line with the DFT reference. The final fitted results described in the next chapter show significantly improved quantitative agreement.

4.5 Fitting program

A fitting program, FITfox, was developed primarily by the author of this thesis to obtain the final parameters for the model described in Section 4.2. The Hamiltonian parameters remained unchanged and hence $U_{bond} + U_{prom}$ remained fixed during all fits. FITfox uses least-squared minimization of the error between a fitted model's binding energies and reference binding energies for given crystal structures. This is done by varying the repulsive parameters and the constant shift, $\Delta E^{\mu}_{i,at}$.

The FITfox program makes use of the Python open-source scientific tools library SciPy (scipy.org), and more specifically the 'fmin' optimizer which uses a Nelder-Mead simplex algorithm to approach the error function minimum. The initial simplex is created by varying each parameter by 5%, or in the case of an initial parameter value of 0.0, the change is ± 0.05. This initial variation of parameters allows the minimization to escape certain local minima if they are small enough. The FITfox

program was therefore run iteratively until the initial and final error function values were numerically equivalent. After comparison with tolerances of 1×10^{-13}, the parameter tolerance and the error function value tolerance were set to 1×10^{-11}. A conjugate-gradient relaxation algorithm was also tested, but was not found to be significantly faster or more accurate. Given the robustness of conjugate-gradient relaxation, this can be attributed to error in the inexact numerical derivatives.

4.6 Summary

All functional forms and parameters used for the final reduced OTB model were described in Section 4.2. As many of the parameters for the reduced OTB model as possible were obtained from DFT. The bond integrals were fit to DFT-projected values obtained from collaborators, as described in Section 4.3. Initial pair-repulsive function data was also obtained from DFT binding energies using a nearest-neighbor approximation described in Section 4.4. The best possible quantitative accuracy for the model in Section 4.2 was obtained using the fitting program described in Section 4.5. Further tests of the final model are described in the following Chapter 5.

5 Tests of reduced tight binding model for silicon carbide

5.1 Electronic structure tests

The OTB Hamiltonian is well defined by the reduced OTB parameters coming from DFT projections, Harrison 2004's onsite energy levels, and selfconsistency through LCN. Comparisons can therefore be made between the electronic structure from DFT (here LDA-PAW), exact projected OTB parameters, and the final model described in Section 4.2. This serves as a starting comparison before including the fitted repulsive parameters. The difference between the DFT electronic structure and the exact projected OTB parameter electronic structure will show the effect of the approximations associated with two-centre OTB, local charge neutrality, and the projection scheme. The final model from Section 4.2 further includes the reduced TB approximation and effects from using a structure-independent parameter set.

Fig. 5.1 shows the electronic DOS for graphite and diamond carbon from DFT, from the exact projected OTB parameters (using an arithmetic average of the *p* onsite levels for the case of graphite), and from the reduced OTB model in Section 4.2.

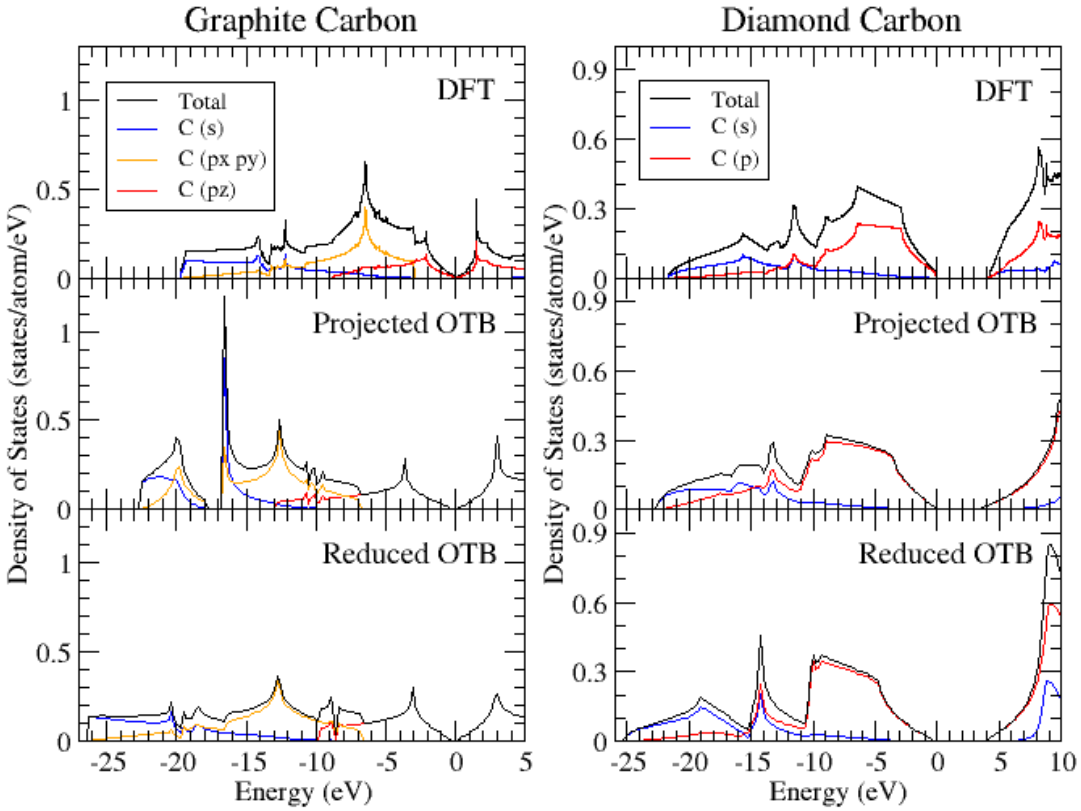

Fig. 5.1. Electronic DOS for graphite and diamond carbon from DFT (top), exact DFT-projected OTB (middle), and the final reduced OTB model (bottom), relative to a E_F of 0.0.

For graphite carbon, the structure of the DOS near the Fermi energy is reproduced fairly well in both OTB cases, reproducing the pseudogap shown in the DFT DOS. The bandwidth however, is too large in both OTB cases, especially for the reduced OTB model. The shape of the final reduced OTB model DOS appears somewhat better with a broad *s*-character band at the bottom of the valence band and no gap appearing in the valence band.

For diamond carbon, both OTB DOS show similar structure to the DFT DOS approaching the Fermi energy of 0.0 eV. The valence bandwidth for the reduced OTB model is significantly larger than for the DFT DOS by more than 3 eV, whereas the

exact projected OTB valence bandwidth is close to that of DFT. The structure in the bottom of the valence band appears better for the final reduced model with an *s*-contribution increasing to a well defined peak, and small *p*-contribution, whereas the structure just above -10 eV before the *p*-state plateau is better captured by the exact projected OTB data.

For both low-energy graphite and diamond carbon structures, the biggest impact appears to come from the OTB approximation given the scale of the errors from top to bottom in Fig. 5.1. The structure-independent onsite levels of the reduced OTB model further impact the reduced OTB DOS bandwidth. Generally, the shape of the DFT DOS is captured fairly well by the reduced OTB model.

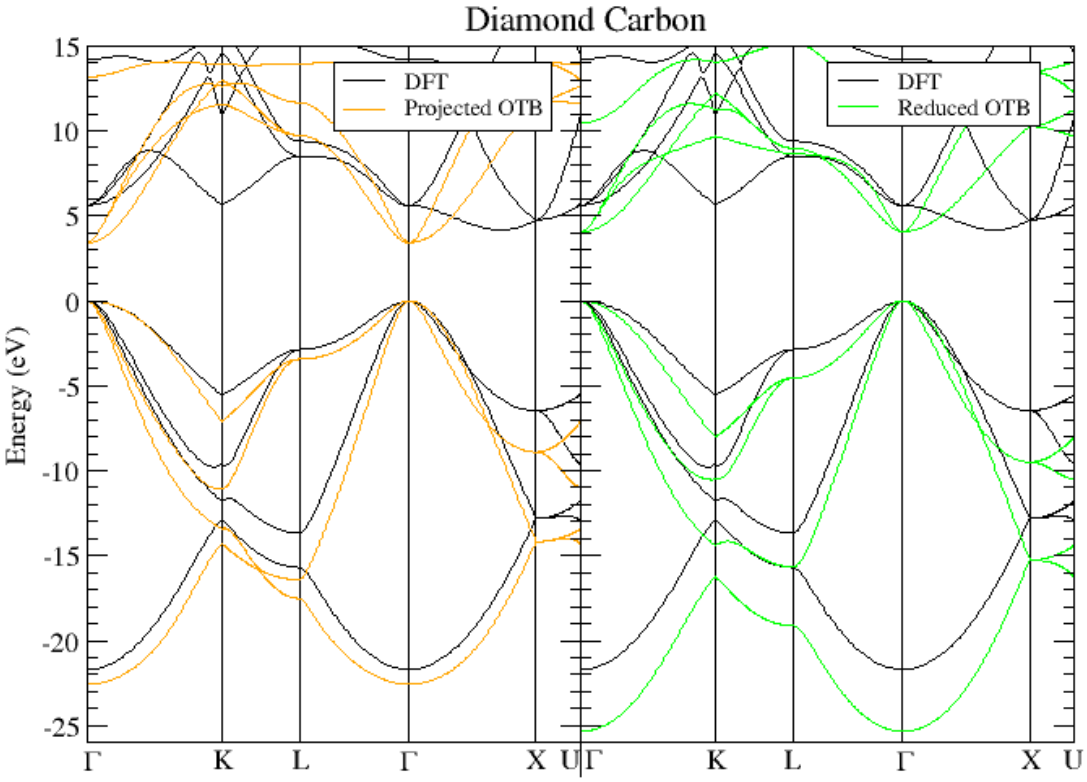

Fig. 5.2. Bandstructure for diamond carbon from DFT (black-reference), exact DFT-projected OTB (orange), and reduced OTB (green), relative to a E_F of 0.0.

The exact projected OTB bandstructure for diamond carbon in Fig. 5.2 shows the two lowest bands crossing between K and L, something not found in the DFT bandstructure. This relates to the odd structure of the DOS around -15 eV. Although the excited states are not reliable for DFT nor OTB, it can be noted that DFT shows an indirect band gap while the exact project OTB model shows a direct band gap at the Γ point. Otherwise, much of the exact projected OTB bandstructure shows similar character to the DFT bandstructure, often shifted slightly.

The reduced OTB bandstructure for diamond carbon on the right of Fig. 5.2 shows the two lowest bands shifted but not crossing between K and L, in contrast with the exact projected OTB bandstructure. This explains the shifted but relatively accurate structure of the DOS near the bottom of the valence band. Again, it can be noted that DFT shows an indirect band gap while the reduced OTB model shows a direct band gap at the Γ point. The lack of structure in the reduced OTB DOS above -10 eV can be attributed to a flattening of the corresponding eigenvalue about K and a flattening of the second-highest valence band between X and U. Otherwise, much of the reduced OTB bandstructure shows similar character to the DFT bandstructure, just shifted lower in energy.

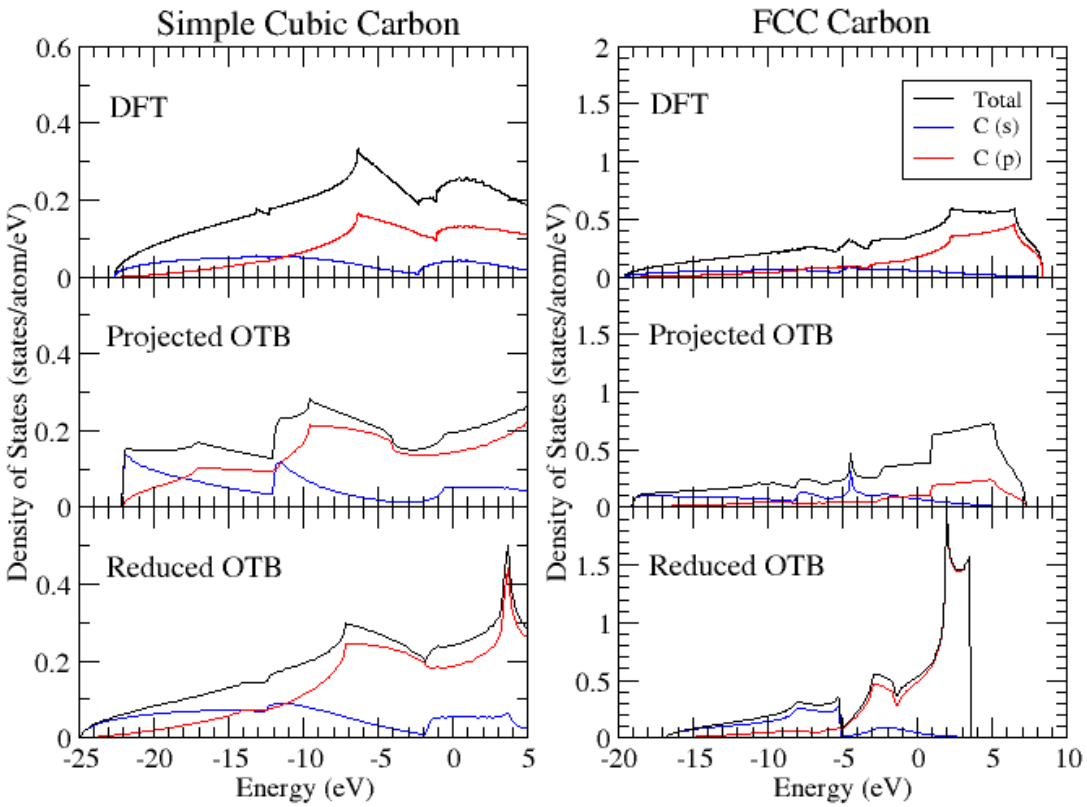

Fig. 5.3. Electronic DOS for higher-energy simple cubic and FCC carbon.

The electronic DOS for simple cubic and FCC carbon are shown in Fig. 5.3. For simple cubic carbon, neither the exact projected OTB nor the reduced OTB DOS show the same concave-downward curvature about E_F. The bandwidth of the DFT DOS is reproduced well by the exact projected OTB model but is overestimated by the reduced OTB model. The overall shape of the DOS and *s*- and *p*-character is reproduced well by the reduced OTB model. This is not the case for the exact projected OTB DOS which fails to reproduce the 3D nearly-free-electron-like behavior at the bottom of the valence band.

For FCC carbon, the exact projected OTB DOS appears to be too flat about the Fermi energy whereas the reduced OTB DOS is too steep. The bandwidth is fairly close for

exact projected OTB within roughly 1 eV compared to a bandwidth which is roughly 3 eV too small for reduced OTB. Again, the DOS at the bottom of the valence band for exact projected OTB is too large, but the overall shape and character is fairly close to DFT. The reduced TB DOS shows similar character to DFT near the bottom of the valence band but shows a significant shoulder just below -5 eV not found in the DFT DOS. Overall, the reduced OTB model reproduces the higher-energy simple cubic DOS fairly well but shows larger errors for FCC carbon.

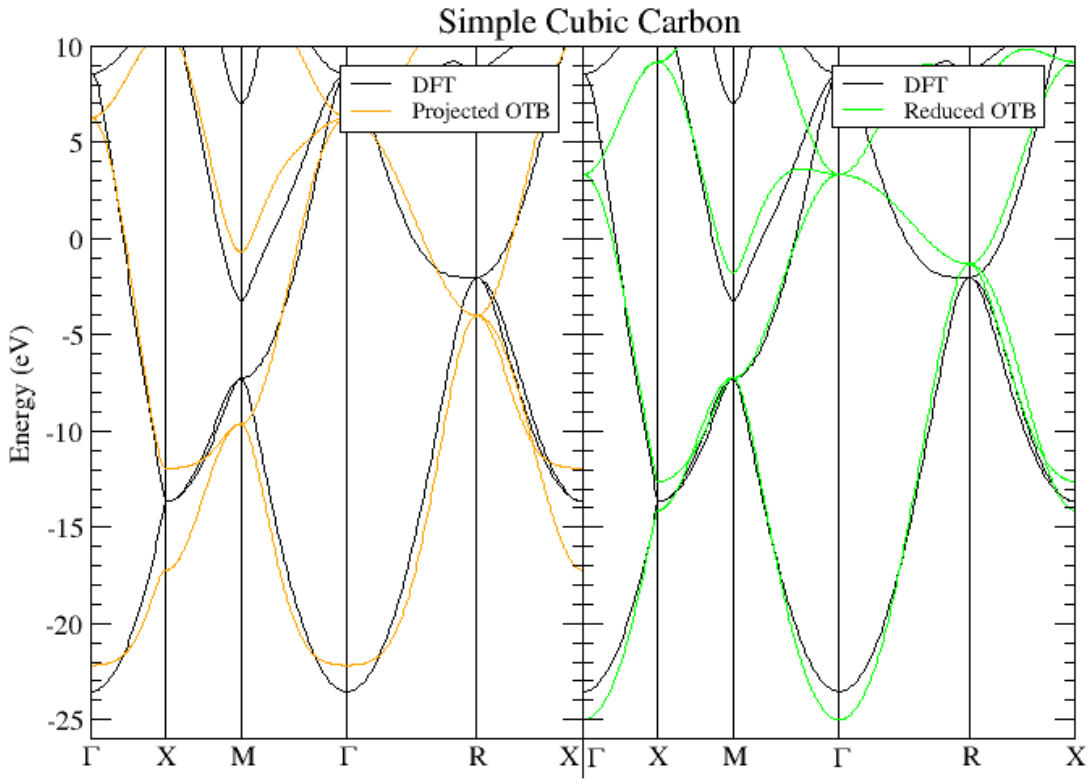

Fig. 5.4. Bandstructure for simple cubic carbon.

The exact projected OTB bandstructure for simple cubic carbon in Fig. 5.4 shows significant differences compared with DFT around the high symmetry point M and between Γ and R at the Fermi energy. The large DOS at the bottom of the valence band can be attributed to a flattening of the lowest band about the Γ point relative to

DFT. Also, significant splitting is found between the two lowest bands at X, not present within DFT.

The reduced OTB bandstructure for simple cubic carbon also shows significant differences compared with DFT around the high symmetry point M and between Γ and R at the Fermi energy. The bandwidth is too large at the Γ point; however, the curvature is reproduced fairly well. The splitting between the two lowest bands at X is still present in the reduced OTB bandstructure, but is much smaller.

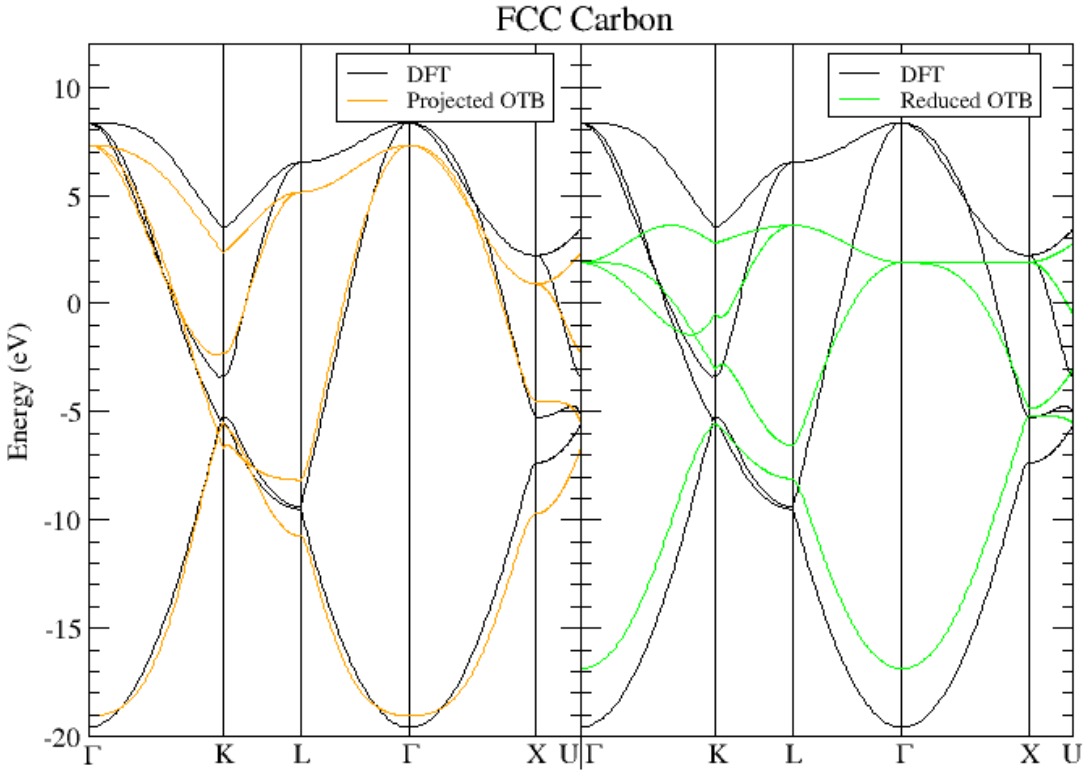

Fig. 5.5. Bandstructure for FCC carbon.

The exact projected OTB bandstructure for FCC carbon in Fig. 5.5 shows differences about the Fermi energy primarily between X and U. The bandwidth is reproduced quite well, but the lowest energy band is too flat about the Γ point. This leads to the

larger DOS values at the bottom of the valence band in Fig. 5.3. Overall the DFT bandstructure is reproduced fairly well except for rather large splitting at L and X.

The reduced OTB bandstructure for FCC carbon shows larger differences compared with DFT. The bandstructure about the Fermi energy is reproduced rather poorly across the first Brillion zone. The bandwidth is too small, although the curvature at the bottom of the valence band is reproduced fairly well. Overall the bandstructure is reproduced rather poorly which is undesirable but perhaps acceptable given how high in energy the FCC structure is relative to other carbon structures.

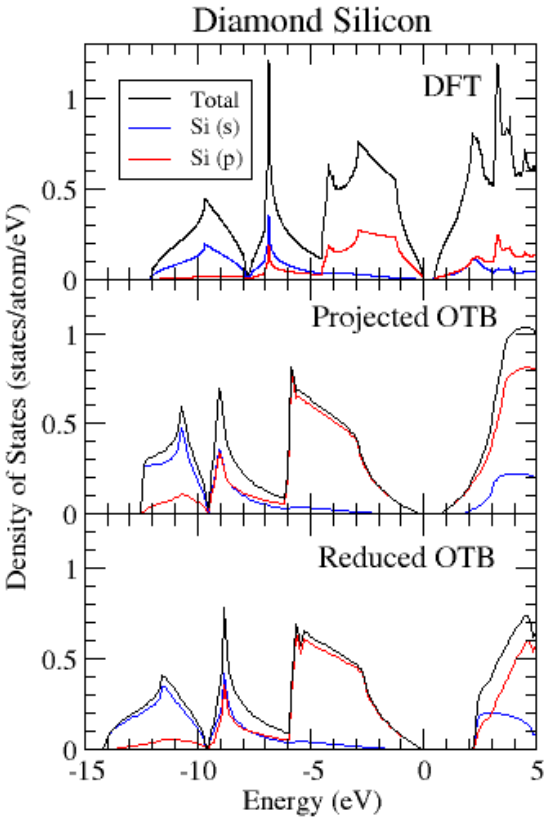

Fig. 5.6. Electronic DOS for diamond silicon.

The electronic DOS for diamond silicon are shown in Fig. 5.6. The DOS approaching the Fermi energy is too low for both the exact projected OTB and the reduced OTB

DOS. The bandwidth is reproduced fairly well by the exact projected OTB model, but the reduced OTB bandwidth is too large by roughly 2 eV. The *s*-contribution at the bottom of the valence band for the exact projected OTB DOS is too large, which is not the case for the reduced OTB DOS. The *p*-dominated character at the top of the valence band in both OTB DOS is missing the structure shown in the DFT DOS between -3 and -4 eV. Otherwise, the general structure of *s*-, hybrid-, and *p*-character peaks increasing in energy through the valence band is reproduced in both OTB cases.

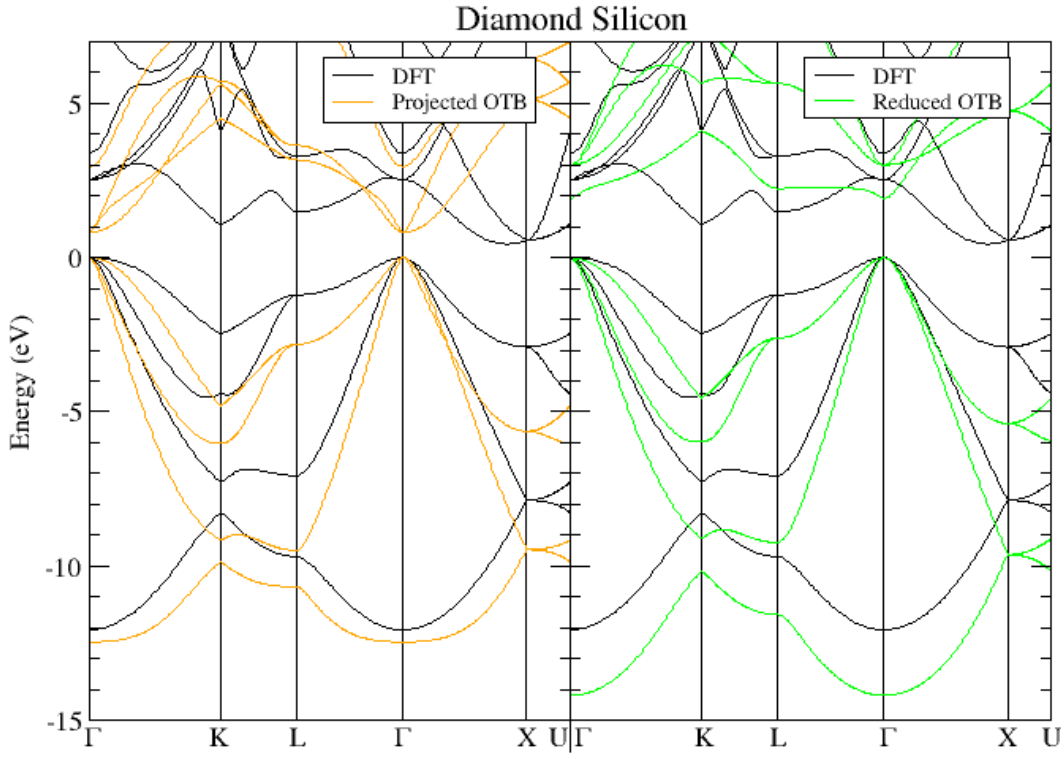

Fig. 5.7. Bandstructure for diamond silicon.

The exact projected OTB bandstructure for diamond silicon in Fig. 5.7 shows strong dispersion about the Γ point at the top of the valence band and significantly lowered eigenvalues at K, L, X, and U, explaining the smaller DOS approaching the Fermi energy compared with DFT. The bandwidth is reproduced well, but the lowest energy

band is too flat about the Γ point. As was found in the carbon OTB models, the missing structure in the *p*-character portion of the valence band can be attributed to a flattening of the second-highest valence band about U compared to DFT. The exact projected OTB bandstructure shows a direct band gap in contrast to an indirect DFT gap.

The reduced OTB bandstructure for diamond silicon shows similar problems to the exact projected OTB bandstructure approaching the Fermi energy. The bandwidth is too large, but the curvature about the Γ point at the bottom of the valence band is reproduced well. Again, the flattening of the second-highest valence band about U explains the lack of structure in the *p*-character DOS. The reduced OTB bandstructure also shows a direct band gap, inconsistent with DFT. Overall, the structure is reproduced fairly well but skewed to lower energies.

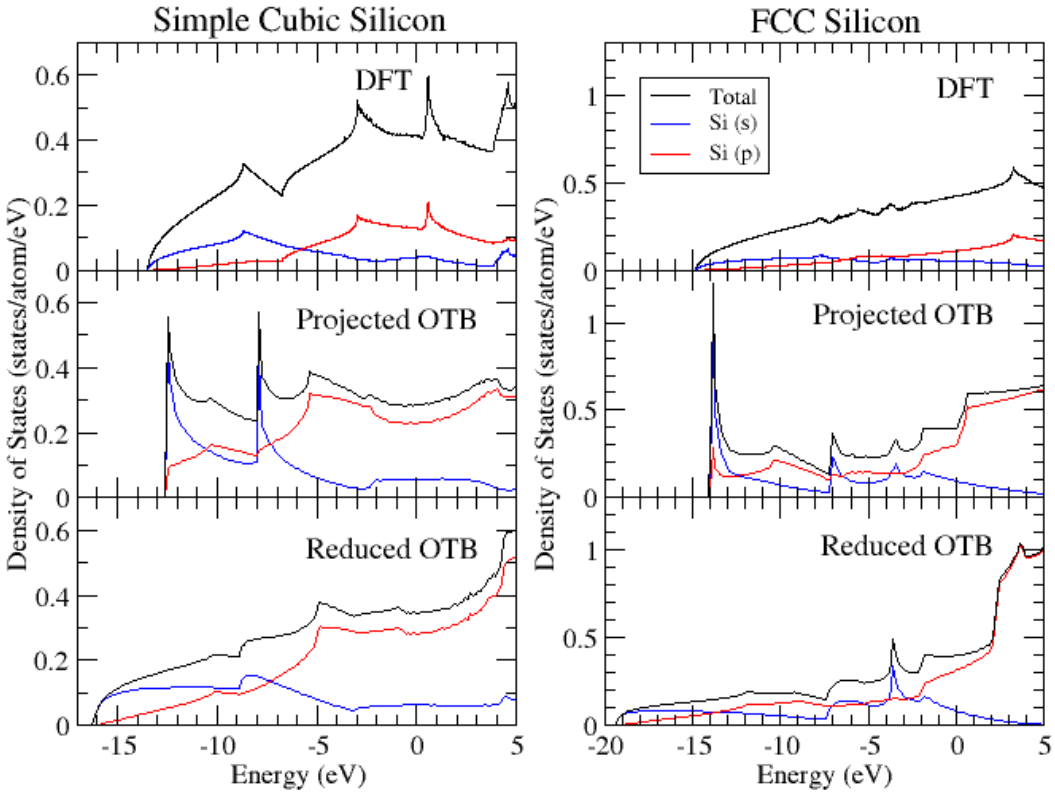

Fig. 5.8. Electronic DOS for higher-energy simple cubic and FCC silicon.

The electronic DOS for simple cubic silicon are shown in Fig. 5.8. The DOS about the Fermi energy are reproduced well by both exact projected OTB and reduced OTB. The bandwidth is roughly 1 eV too small for exact projected OTB and roughly 2.5 eV too large for reduced OTB. The DFT DOS shows a broad *s*-peak at lower energies and a broad *p*-peak at higher energies in the valence band. This behavior is not captured by either the exact project OTB or reduced TB DOS. The exact projected DOS shows very little resemblance to the DFT DOS with two *s*-peaks at the bottom of the valence band and at -8 eV. The reduced OTB DOS also shows little resemblance to the DFT DOS, but does capture the 3D nearly-free-electron-like behavior at the bottom of the valence band.

The electronic DOS for FCC silicon about the Fermi energy is reproduced fairly well by reduced OTB but shows significantly different *p*-character towards the conduction states for exact projected OTB. The bandwidth is reproduced well by exact projected OTB whereas the reduced OTB bandwidth is roughly 5 eV too large. Again the exact projected OTB DOS shows completely different behavior at the bottom of the valence band with a peak around -14 eV. The reduced OTB DOS shows similar character to DFT. Both OTB DOS show peaks within the valence band inconsistent with the DFT DOS, but the exact projected OTB DOS appears worse with more *s*- and *p*-character peaks not present in the DFT DOS. Overall, the DOS for these higher-energy silicon structures show significant errors.

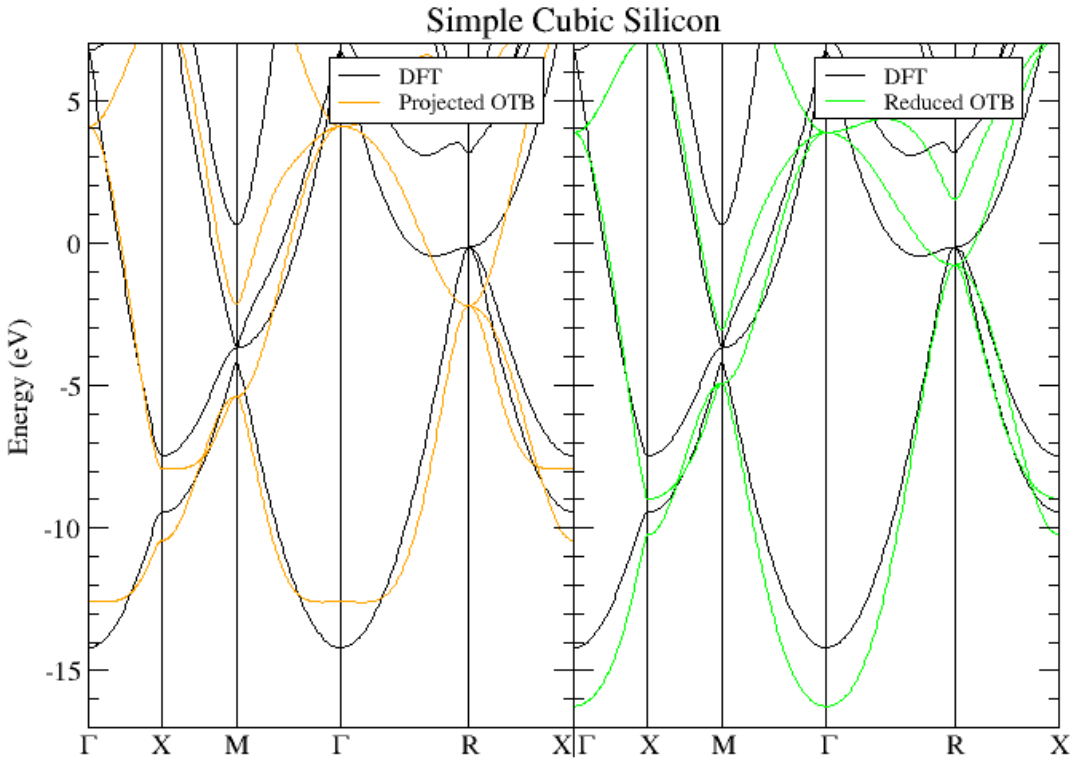

Fig. 5.9. Bandstructure for simple cubic silicon.

The exact projected OTB bandstructure for simple cubic silicon in Fig. 5.9 shows significant differences compared to the DFT bandstructure about the Fermi energy particularly around M and R. At the bottom of the valence band, the exact projected bandstructure is significantly flattened about the Γ point, creating the peak in the DOS. The band degeneracies at M are also inconsistent with DFT.

The reduced OTB bandstructure for simple cubic silicon shows similar discrepancies about the Fermi energy, although the lowest eigenvalue at R is much closer to DFT. The reduced TB bandwidth is too large, but the curvature of the lowest band about the Γ point is reproduced fairly well. The degeneracies at M are inconsistent with DFT, as was the case for the exact projected OTB bandstructure. In summary, the accuracy of the OTB bandstructure for simple cubic silicon is rather limited.

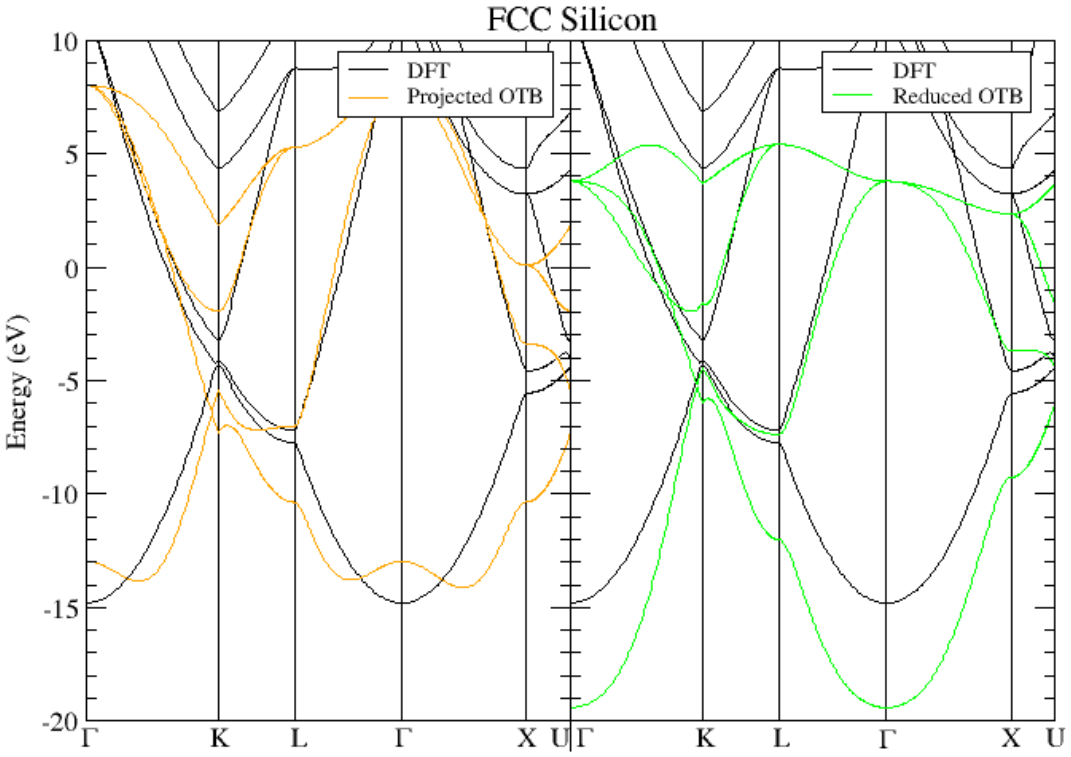

Fig. 5.10. Bandstructure for FCC silicon.

The exact projected OTB bandstructure for FCC silicon in Fig. 5.10 shows significantly different behavior at and above the Fermi energy primarily due to the highest energy bands between X and U which are lowered in energy relative to DFT. Although the bandwidth is reproduced fairly well, the dispersion of the lowest band is reproduced poorly with minima away from the Γ point, leading to the peak found at the bottom of the exact projected OTB DOS. Further discrepancies arise from the rather poor reproduction of the lowest energy bands between K and L and all the bands between X and U.

The reduced OTB bandstructure for FCC silicon shows slightly better behavior about the Fermi energy as the error in the top bands between X and U is not as large. The

bandwidth is too large, but the curvature of the lowest energy band about the Γ point is reproduced fairly well leading to the similar shape of the bottom of the valence band DOS. As was found in the exact projected OTB bandstructure, the second-lowest band decreases in energy between X and U, inconsistent with the DFT bandstructure. Other bands appear to show similar features compared with the DFT bandstructure but are significantly skewed to lower-energy values.

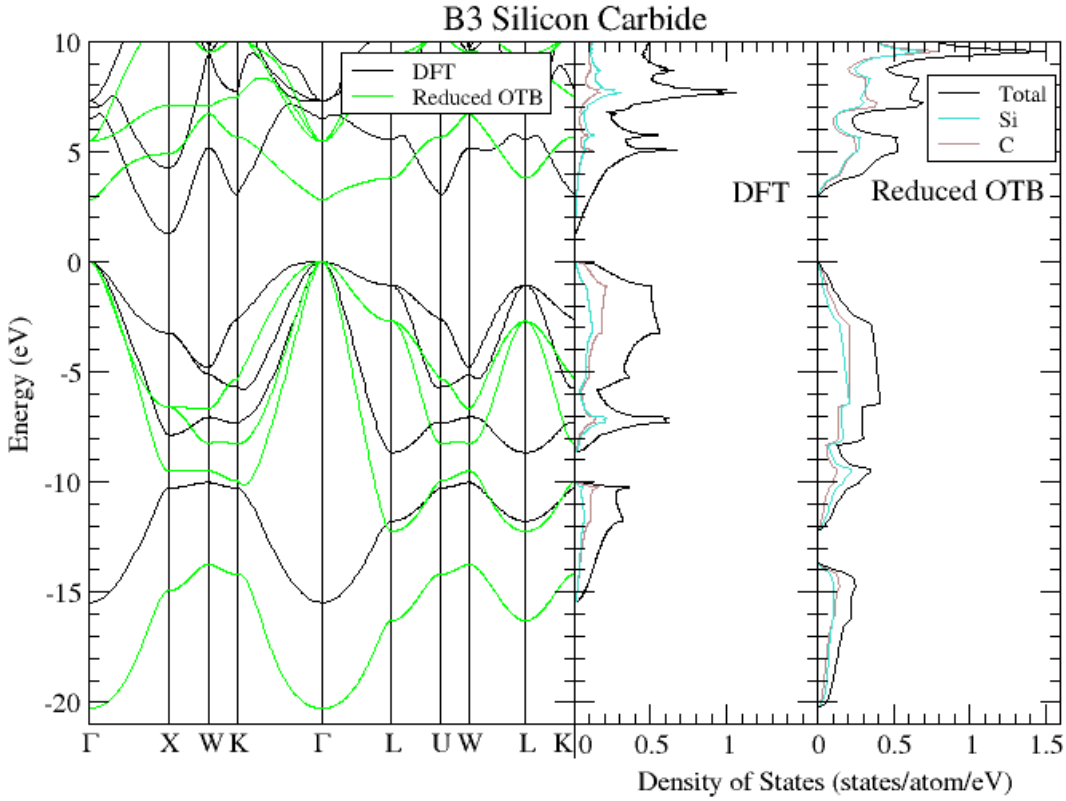

Fig. 5.11. Electronic structure for B3 SiC comparing DFT with reduced OTB.

The electronic structure for B3 SiC is shown in Fig. 5.11 without exact projected OTB results since the exact equilibrium projected data was not available. Similar to the diamond carbon and diamond silicon DOS, the reduced OTB DOS for B3 SiC on the right of Fig. 5.11 shows a more gradual decline in magnitude approaching the Fermi energy. The bandwidth is too large by roughly 5 eV but shows similar

character at the bottom of the valence band. Looking at the separate species contributions, the LCN reduced OTB DOS captures fairly well the structure of the valence band, with errors smaller than those found in the higher-energy elemental structures. This could be taken as some indication that the LCN approximation used for the reported OTB calculations throughout this thesis is a sensible approximation for this type of model.

The reduced OTB bandstructure for B3 silicon carbide in Fig. 5.11 shows stronger dispersion than DFT about the Γ point near the Fermi energy, explaining the smaller DOS values. Clearly the reduced OTB bandwidth is too large, but except for a shift to lower-energy values, the dispersion of the lowest energy band is reproduced well. The dispersion of the other bands is also reproduced fairly well except for a shift to lower-energy values. One exception is the separation of the top two valence bands at W which are nearly degenerate in DFT. This relates to the structure in the DOS found at roughly -4 eV in DFT and -7 eV in reduced OTB.

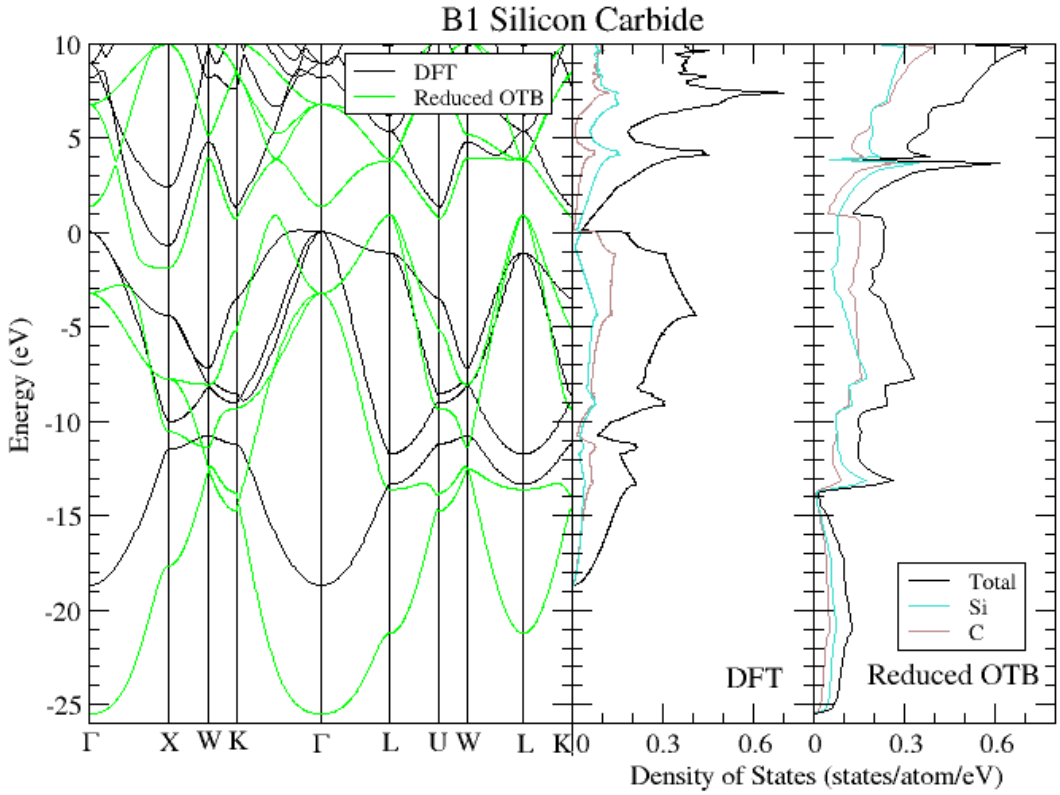

Fig. 5.12. Electronic structure for B1 SiC comparing DFT with reduced OTB.

The electronic structure for B1 SiC is shown in Fig. 5.12. Overall, the DOS is reproduced poorly. The pseudogap at the Fermi energy is not reproduced, the bandwidth is over 6 eV to large, and much of the general structure of the valence band is lost.

The reduced OTB bandstructure for B1 SiC shows significant differences across the first Brillion zone. Not only are bands shifted, often to lower energies, as was found in many of the elemental bandstructure figures, but dispersion is too strong, too weak, and at times in the wrong direction compared with DFT. There are also band degeneracies not present in the DFT bandstructure.

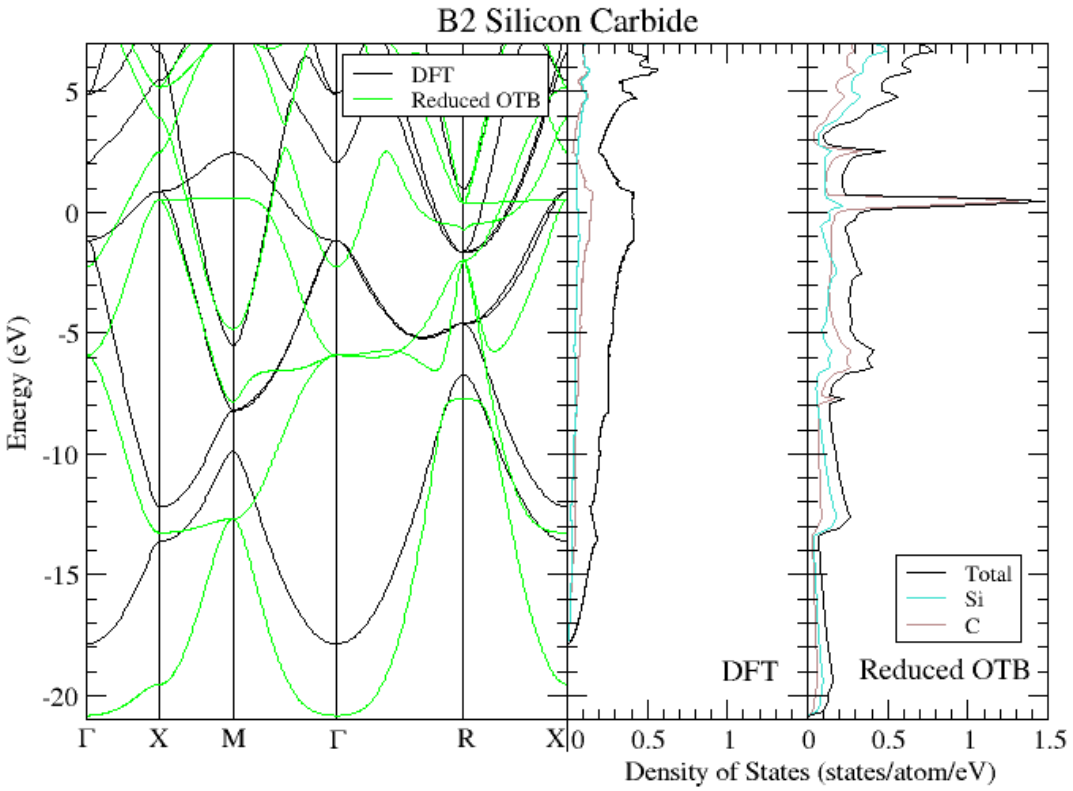

Fig. 5.13. Electronic structure for B2 SiC comparing DFT with reduced OTB.

The electronic structure for B2 SiC is shown in Fig. 5.13. Similar to the B1 structure, the reproduction of the DFT DOS is poor. The DFT DOS at the Fermi energy is flat in a plateau region, where as the reduced OTB DOS is beginning a peak towards the conduction states. The bandwidth is roughly 3 eV too large, and the overall structure shows little similarity to DFT.

The reduced OTB bandstructure for B2 SiC shows very little resemblance to the DFT bandstructure, with significant deviations across the first Brillion zone. The peak in the reduced OTB DOS is explained by the flat band between X and M as well as R and X in the reduced OTB bandstructure.

The OTB electronic structure appears to be well reproduced for the groundstate elemental diamond and binary B3 structures. Agreement for higher-energy structures is not as good, particularly for the binary B1 and B2 structures. As the reduced OTB model makes further approximations compared with the exact DFT-projected OTB DOS, one would anticipate the reduced OTB model to show larger errors in comparison with the exact DFT-projected OTB DOS. For a number of structures, this was not the case, with the reduced OTB model showing more similarities to the DFT electronic structure in comparison with the exact DFT-projected OTB electronic structure. This could be related to the projection methodology used. Some errors could have been minimized in creating the reduced OTB model as a number of methodologies for fitting through the projected data points needed to be tested before a sensible model was produced, as was described in Section 4.3. Clearly these small deviations in fitting through the projected data points and the use of different atomic onsite energy levels have a significant impact on the reproduction of the electronic structure.

5.2 Binding energies

All repulsive parameters and the constant shift, $\Delta E_{i,at}^{\mu}$, given in Section 4.2 were fit to DFT binding energies except for the hard-core repulsive parameters which were subsequently fit to the curvature of the DFT dimer binding energies. The DFT reference binding energies are LDA-PAW VASP energies [82-88] relative to the spin-polarized free atom. The initial fit of the GSP pair-repulsive functions, power-law embedding functions, and constant shifts $\Delta E_{i,at}^{\mu}$, involved varying the parameters for the entire system simultaneously. Earlier models which first fit the elemental

systems and later fit the binary system with the few remaining binary parameters were not satisfactory.

Three criteria were used to determine which structures were included in the fitting database. Groundstate and near-groundstate structures were included. Other common simple crystal structures were included to sample different coordinations and geometries. Finally, structures which have empirically been incorrectly predicted to be groundstate structures within reduced OTB model fits have also been included to best correct any missing physical contributions. The binary fitted structures were B1, B2, B3, and the Si-C dimer for hard-core repulsion. The carbon structures which were fitted were diamond, graphite, FCC, simple cubic and the C-C dimer for hard-core repulsion. The silicon structures which were fitted were diamond, FCC, simple cubic, Clathrate 34, simple hexagonal, and the Si-Si dimer for hard-core repulsion.

In addition to being used for the fitting, structural binding energies about equilibrium were used to test the reduced OTB model to best ensure no spurious groundstate structures are predicted. A database of DFT binding energies was calculated for 51 elemental crystal structures for carbon, 50 elemental crystal structures for silicon, and 156 binary crystal structures at various compositions for silicon carbide. All the structures are listed in the Appendix. Although there can be no guarantee that the final reduced OTB model will not incorrectly predict some different crystal structure outside the given database to be the groundstate, significant effort was made to make the database as large and geometrically diverse as possible.

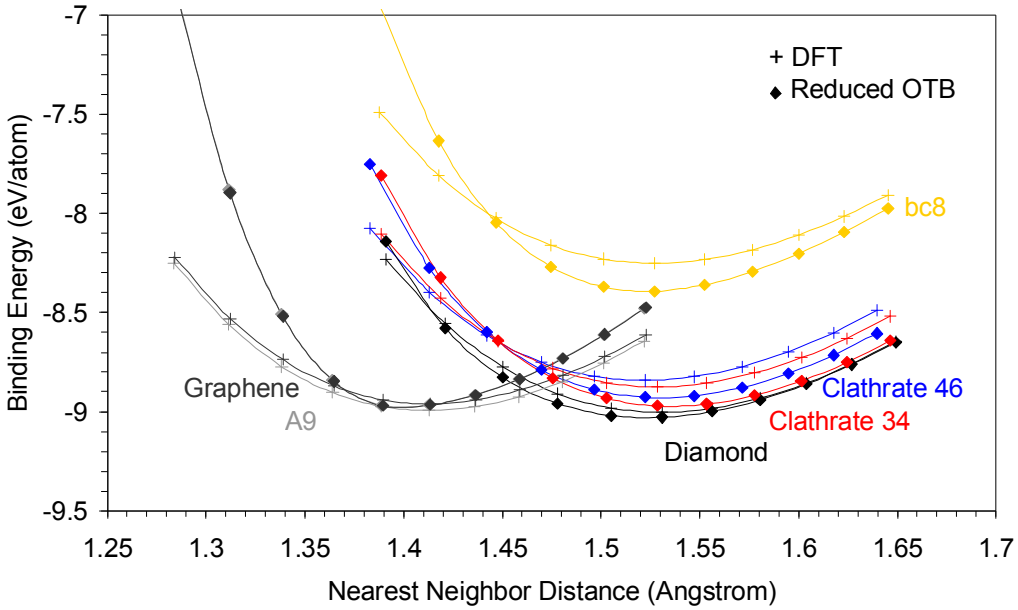

Fig. 5.14. Carbon binding energies of the lowest energy structures from DFT and the final reduced OTB model.

Figure 5.14 highlights the lowest binding energy structures for elemental carbon from both DFT and the reduced OTB model. Note that the diamond structure is the groundstate structure predicted by both DFT and the reduced OTB model. Effects from the hard-core repulsive term can already be seen in the graphene and A9/graphite structures under compression as the hard-core repulsive contribution begins at 1.4 Angstrom for carbon. Graphene and A9/graphite are indeed energetically identical about equilibrium within the reduced OTB model as the inter-planar separation is larger than the cutoff of the model.

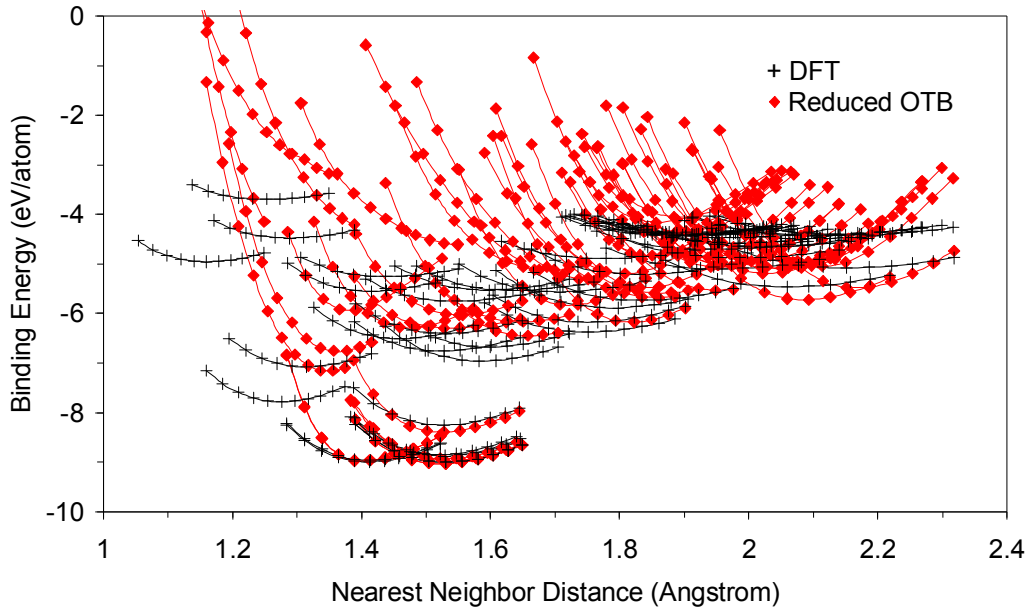

Fig. 5.15. Carbon binding energies of all the tested structures from DFT and the final reduced OTB model.

Figure 5.15 shows the entire database of binding energies for elemental carbon, including the same binding energies as shown in Fig. 5.14. No spurious groundstate structures are predicted, and higher-energy structures are destabilized relatively accurately.

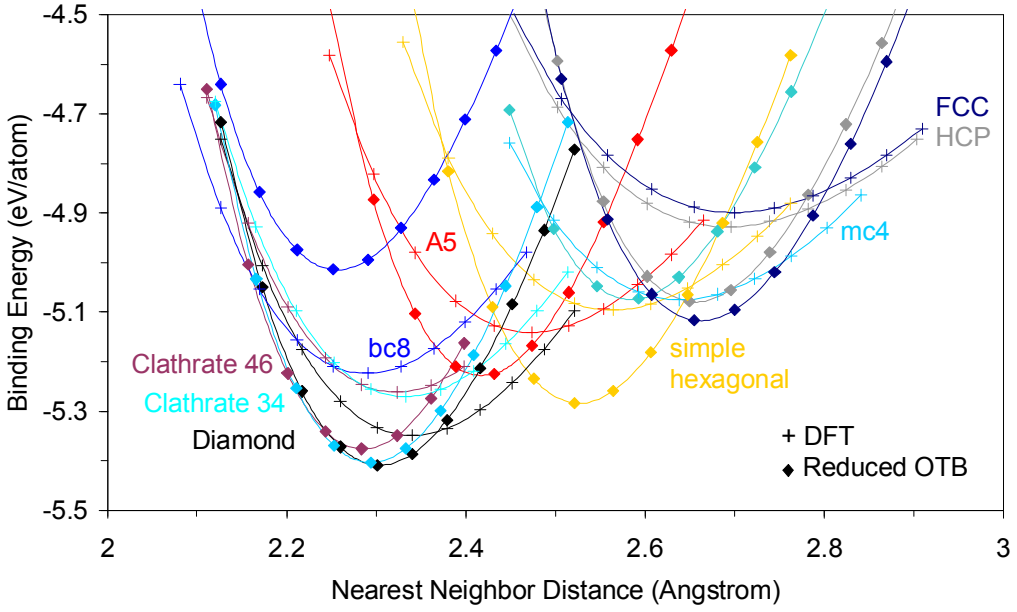

Fig. 5.16. Silicon binding energies of the lowest energy structures and select others from DFT and the reduced OTB model.

Figure 5.16 highlights the lowest binding energy structures for elemental silicon as well as select others from both DFT and the reduced OTB model. Note that the diamond structure is the groundstate structure predicted by both DFT and the reduced OTB model. During the fitting of the reduced OTB model, many tested models incorrectly predicted the clathrate, simple hexagonal, or FCC structures to either be the groundstate or very low in energy. Other models were better able to reproduce the diamond binding energy but often predicted the wrong groundstate structure. The present model reproduces much of the DFT structural ordering.

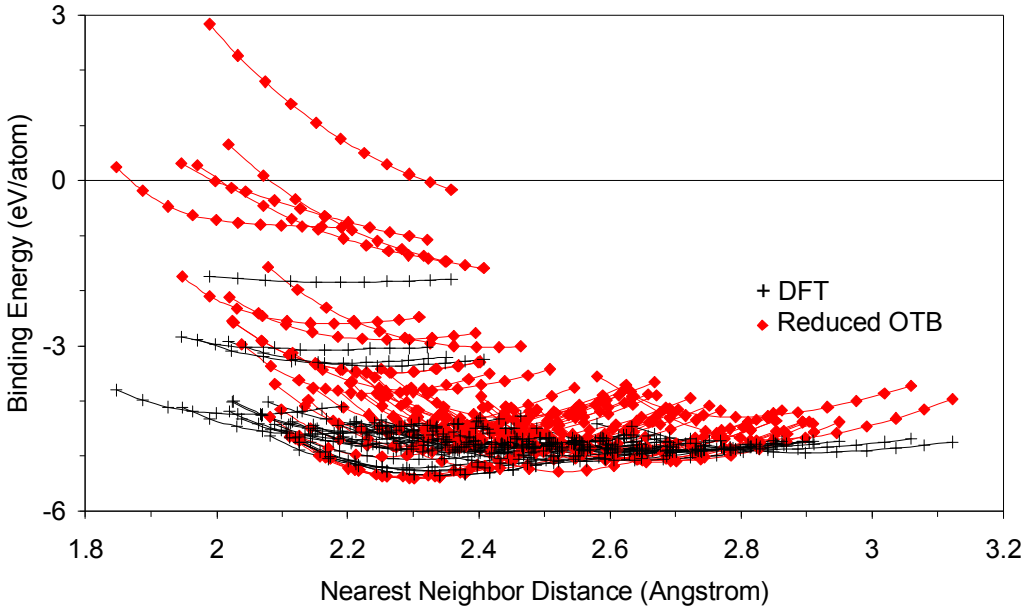

Fig. 5.17. Silicon binding energies of all the tested structures from DFT and the final reduced OTB model.

Figure 5.17 shows the entire database of binding energies for elemental silicon, including the same binding energies as shown in Fig. 5.16. No spurious groundstate structures are predicted, and higher-energy structures are destabilized. Note that besides some very open structures with short nearest-neighbor distances, the structural energy differences are very small for silicon compared with carbon. Fitting

a model for silicon with no spurious groundstate structures and roughly correct structural ordering was significantly more challenging than for carbon, and the relatively small energy differences found in silicon may have played a significant role.

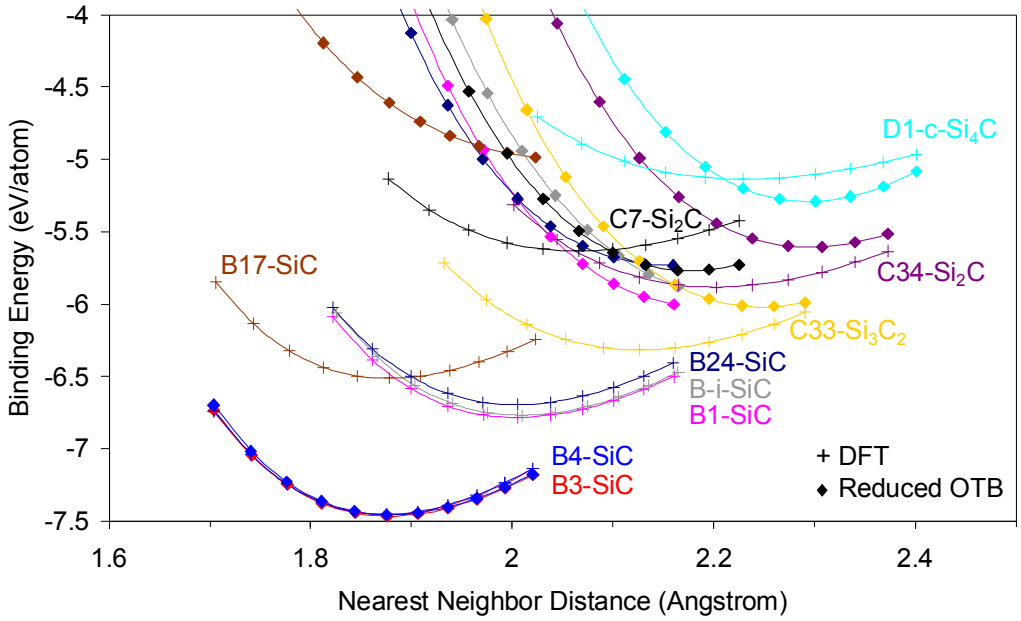

Fig. 5.18. Silicon carbide binding energies of the lowest energy structures and select others from DFT and the reduced OTB model.

Figure 5.18 highlights the lowest binding energy structures for silicon carbide as well as select others from both DFT and the reduced OTB model. Note that the B3 and B4 structures amongst other polytypes about the groundstate all have binding energies within 4 meV, close to the accuracy of DFT. Within reduced OTB, the polytypes tested, including 2H, 3C, 4H, 6H, and 9R all had binding energies within 10 meV of each other. They also were the structures with the lowest binding energies for both DFT and the reduced OTB model. Note that in the last section the electronic structure for the B1 structure was not reproduced well by the reduced OTB model, and in Fig.

5.18, likewise the binding energy is not reproduced well with too high an equilibrium binding energy and too large an equilibrium nearest-neighbor distance.

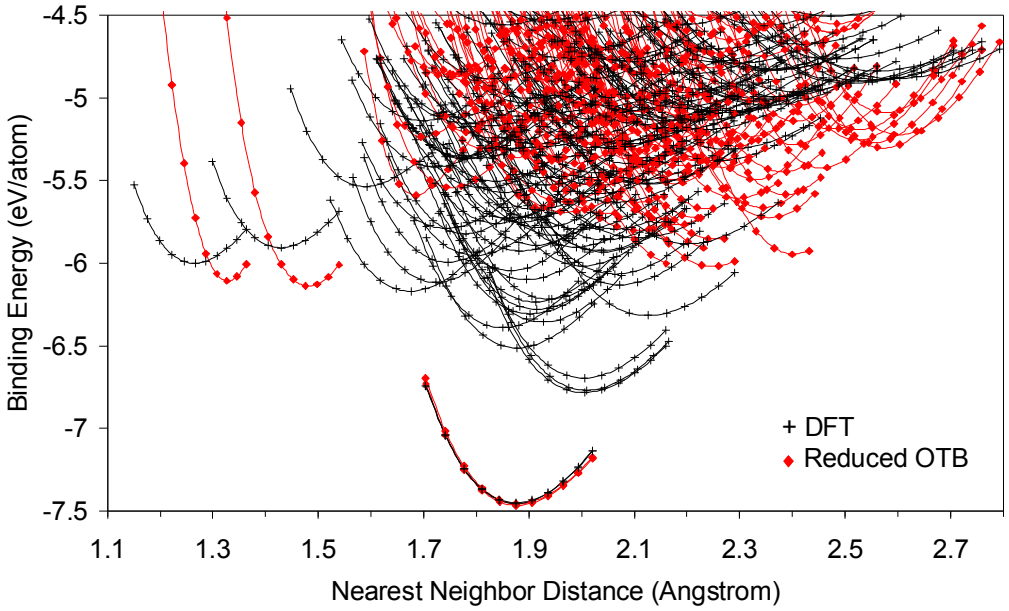

Fig. 5.19. Silicon carbide binding energies of tested structures from DFT and the final reduced OTB model.

Figure 5.19 shows the binding energies of the tested structures of silicon carbide below -4.5 eV/atom, including the same binding energies as shown in Fig. 5.18. No spurious groundstate structures are predicted, and higher-energy structures are destabilized. Many structures of intermediate stability, shown as well in Fig. 5.18, are destabilized too much. This was not able to be fixed within the current parameterization scheme without creating new spurious groundstate structures.

The binding energies in this section show good accuracy for the experimentally relevant groundstate structures and destabilization of the higher-energy structures. Given the testing in Figs. 5.15, 5.17, and 5.19, the reduced OTB model described in

Section 4.2 shows good indication of being robust for modelling the entire Si-C system, from elemental to binary calculations, with a single set of parameters.

5.3 Histograms of coordination shells at equilibrium

Coordination shell, or neighbor histograms can be used to identify at which distances the pairwise distance-dependent functions are typically evaluated, as well as to identify the gaps between the coordination shells. This is most easily visible when considering the lowest energy structures at their equilibrium volume. Coordination shell, or neighbor histograms can also clarify how thoroughly the distance-dependence of the pairwise functions is tested, as certain distances could potentially not be tested if they fall between shells. Considering all the structures in the elemental and binary test beds just at equilibrium provides a conservative estimate of this distance sampling.

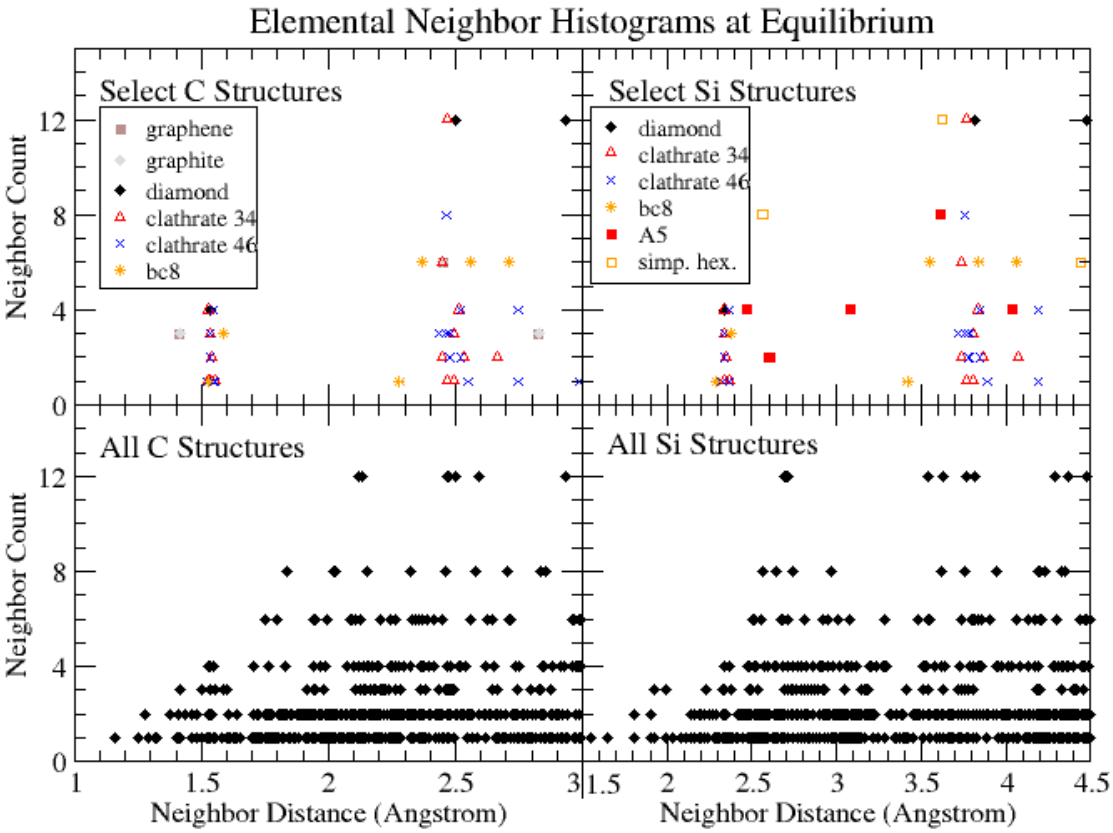

Fig. 5.20. Neighbor histogram for select low-energy structures (top) and all tested structures (bottom) at equilibrium for carbon (left) and silicon (right).

The neighbor histogram for the select low-energy carbon structures on the top left of Fig. 5.20 shows a significant gap between 1.6 and 2.2 Angstrom, or first and second shells. These low-energy structures access the pairwise distance-dependent functions within a narrow range about 1.5 Angstrom for first-shell interactions but show significant differences in second-shell distances starting before 2.3 Angstrom for the bc8 structure through roughly 2.8 Angstrom for the clathrate 46 structure.

More thorough testing of the carbon-carbon pairwise distance-dependent functions is shown on the bottom left of Fig. 5.20 for all tested carbon structures at equilibrium, which shows no distinct gaps in testing between roughly 1.3 Angstrom through the maximum range of the reduced OTB model, 2.8 Angstrom. Given all the structures tested, there is no gap as seen in the select structures at roughly 2.0 Angstrom. With all the non-equilibrium points tested as well, this indicates a rather thorough testing of the carbon-carbon pairwise distance-dependent functions.

The neighbor histogram for select low-energy silicon structures at equilibrium is shown on the top right. The gap between first- and second-shell interactions is bridged by the A5 structure, but still there are far fewer pair interactions at distances between 2.7 and 3.3 Angstrom. The lowest energy diamond and clathrate structures show nearest-neighbor interactions within a narrow range about 2.35 Angstrom, but show a wider spread of second-neighbor interaction distances from 3.7 to 4.2 Angstrom.

More thorough testing of the silicon-silicon pairwise distance-dependent functions is shown on the bottom right of Fig. 5.20 for all tested silicon structures at equilibrium. There is slightly less sampling around 3.3 Angstrom, which could be considered a rough estimate of a first-shell cutoff distance for silicon. Still, there is significant sampling from roughly 1.8 Angstrom through the maximum range of the reduced OTB model, 4.3 Angstrom. With all the non-equilibrium points tested as well, this indicates a rather thorough testing of the silicon-silicon pairwise distance-dependent functions.

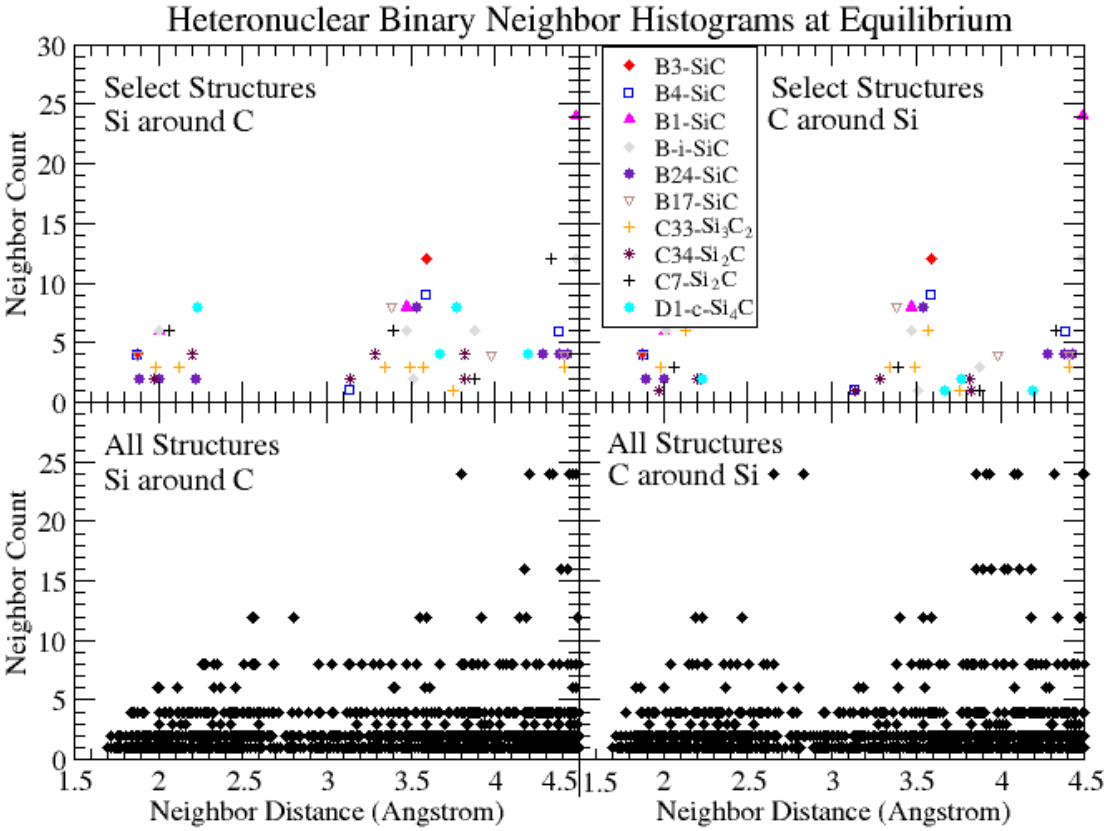

Fig. 5.21. Heteronuclear binary neighbor histogram for select low-energy structures (top) and all tested structures (bottom) of silicon carbide at equilibrium. Silicon neighbors around carbon atoms are shown on the left and carbon neighbors around silicon atoms are shown on the right.

The top left of Fig. 5.21 shows the neighbor histogram of silicon neighbors about carbon atoms for select low-energy silicon carbide structures at equilibrium. The silicon-carbon pairwise distance-dependent functions tend to be accessed from 1.9 to 2.2 Angstrom for nearest-neighbor interactions and then from 3.1 Angstrom onwards for further neighbor interactions. Note that binary structures often tend to have heteronuclear nearest-neighbor interactions and homonuclear second-neighbor interactions, particularly for 1:1 compositions. The gap from 2.3 to 3.1 Angstrom in the heteronuclear interactions is the region of second-neighbor homonuclear interactions shown later in Fig. 5.22.

The top right of Fig. 5.21 shows the neighbor histogram of carbon neighbors about silicon atoms for select low-energy silicon carbide structures at equilibrium. This neighbor histogram is very similar to the histogram of silicon neighbors about carbon atoms, the only differences being for the structures where the silicon and carbon sites are not binary equivalents of one another. Particularly the only differences in Fig. 5.21 occur in the off 1:1 composition structures. Otherwise, the same observations apply.

The neighbor histograms on the bottom of Fig. 5.21 for silicon neighbors about carbon atoms and carbon neighbors about silicon atoms for all silicon carbide structures at equilibrium shows significant sampling of the binary pairwise distance-dependent functions from 1.7 Angstrom up to the maximum binary range of the reduced OTB model, 3.8 Angstrom. Slightly fewer interactions occur around 2.9 Angstrom for carbon neighbors about silicon atoms, but the sampling is still roughly

continuous. With the addition of all the non-equilibrium points tested, this indicates rather thorough sampling of the Si-C pairwise distance-dependent functions.

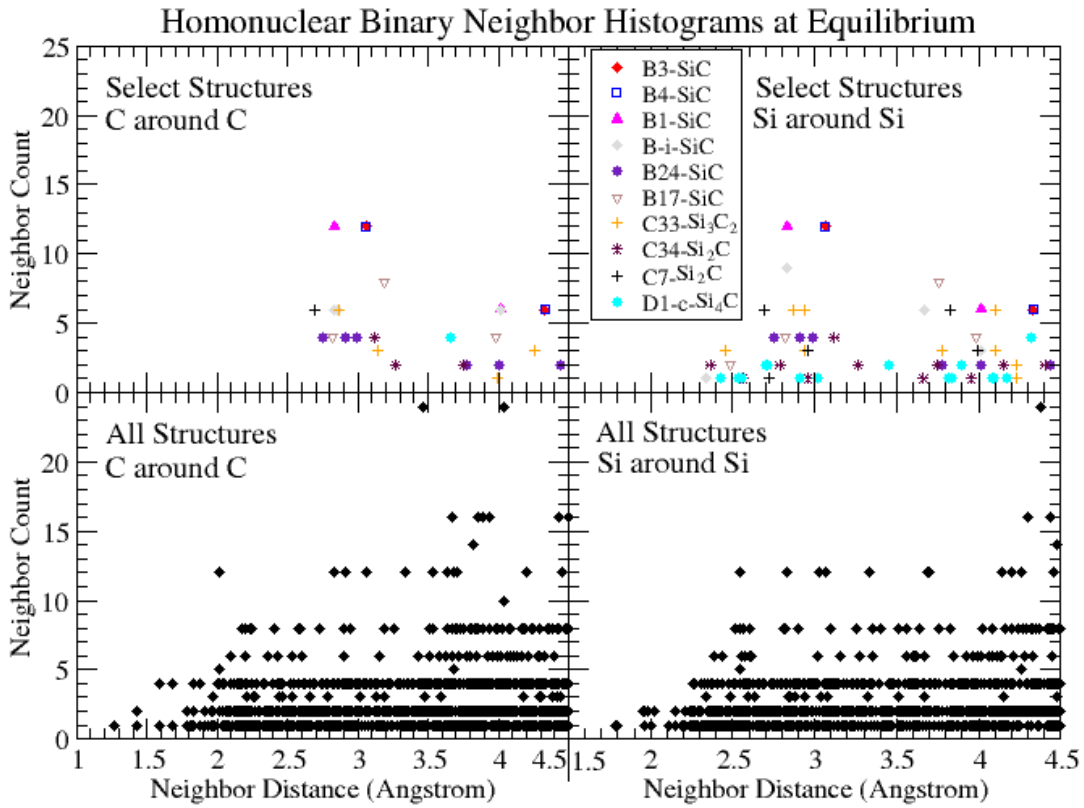

Fig. 5.22. Homonuclear binary neighbor histogram for select low-energy structures (top) and all tested structures (bottom) of silicon carbide at equilibrium. Carbon neighbors around carbon atoms are shown on the left and silicon neighbors around silicon atoms are shown on the right.

The neighbor histogram of carbon neighbors about carbon atoms for the select low-energy silicon carbide structures at equilibrium is shown on the top left of Fig. 5.22. Note there are significantly fewer homonuclear carbon-carbon interactions in the plot in comparison to homonuclear silicon-silicon interactions on the top right. This is due to the lower-energy off-1:1 composition structures shown, which tend to have higher silicon concentrations, hence the chance for more silicon-silicon interactions. As carbon is alloyed with silicon, the lattice parameter and neighbor distances tend to

increase relative to the elemental carbon system, pushing the second-neighbor homonuclear interactions from Fig. 5.20 nearer the maximum range of the reduced OTB model for carbon-carbon interactions, 2.8 Angstrom. This indicates that the relative contribution will be small from carbon-carbon pairwise distance-dependent functions.

The neighbor histogram of silicon neighbors about silicon atoms for select low-energy structures of silicon carbide is shown on the top right of Fig. 5.22. Note how the silicon-silicon pairwise distance-dependent functions are accessed in the gap region of Fig. 5.21 from 2.3 to 3.1 Angstrom. This also happens to be in the gap region of the lowest energy elemental silicon structures in Fig. 5.20. In other words, the top right of Fig. 5.22 shows the importance of having a smooth, sensible transition from first- to second-shell interactions in an elemental model as these intermediate distances can be relevant second-neighbor distances in binary systems, particularly when alloyed with lighter elements.

The neighbor histogram on the bottom left of Fig. 5.22 for carbon neighbors about carbon atoms for all silicon carbide structures at equilibrium shows significant sampling of the elemental carbon-carbon pairwise distance-dependent functions from 1.6 Angstrom up to the maximum binary range of the carbon reduced OTB model, 2.8 Angstrom. This range is shifted to slightly longer distances in comparison with all the elemental structures shown in Fig. 5.20. Still, rather short distances can arise in the carbon-rich binary silicon carbide structures.

The neighbor histogram on the bottom right of Fig. 5.22 for silicon neighbors about silicon atoms for all silicon carbide structures at equilibrium shows significant sampling of the elemental silicon-silicon pairwise distance-dependent functions from 2.1 Angstrom up to the maximum binary range of the reduced OTB model, 4.3 Angstrom. This again highlights the relative importance of silicon-silicon pairwise distance-dependent interactions in the binary silicon carbide structures.

The coordination shell, or neighbor histograms in this section highlight at which distances the pairwise distance-dependent functions are typically evaluated, as well as where gaps exist between first and second shells in the lowest energy structures. By considering just the equilibrium structures in the elemental and binary test beds, and not other tested volumes, a conservative estimate of the distance sampling is obtained. Figs. 5.20 and 5.22 show thorough sampling of the elemental pairwise distance-dependent functions with no significant gaps between typical neighbor shell distances. The same is shown for the binary silicon-carbon pairwise distance-dependent functions in Fig. 5.21.

5.4 Bond, promotion, and repulsive energy contributions

As described in the binding energy expression in Equation (82), the binding energy can be broken down into the bond, promotion, and repulsive energies which all vary depending on crystal structure and volume, as well as the atomic energy which is a constant energy shift dependent only on the species of an atom. The distance- or volume-dependent energy contributions are reviewed in this section.

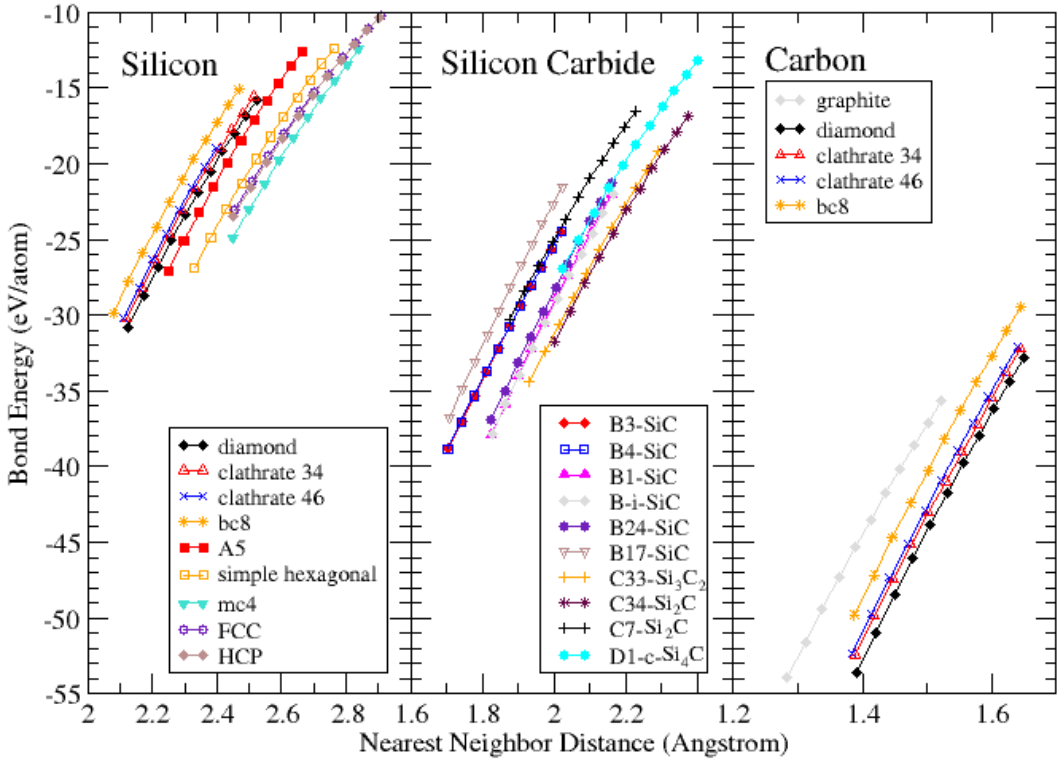

Fig. 5.23. Bond energy contribution for select structures in the Si-C system.

The bond energy contribution for select structures about equilibrium for silicon in Fig. 5.23 shows similar magnitude values for the lowest energy structures, although the equilibrium neighbor distances vary. The higher-coordinated FCC and HCP structures show a reduction in the bond energy by almost a factor of two. Likewise, the silicon carbide bond energies are rather similar in magnitude for the 1:1 composition structures, with equilibrium nearest-neighbor distances which vary slightly. The four structures shown with off 1:1 composition tend to show less strong bond energy contributions.

For carbon, although the equilibrium nearest-neighbor distance for the graphite structure is significantly smaller than for diamond, the bond energy contribution is very close in magnitude. The bond energy is slightly less strong for the bc8 structure

which has a slightly higher binding energy as well. Note that the absolute magnitudes of the bond energies for the elemental and binary systems vary significantly relative to one another with elemental silicon structures showing the weakest bond energy contribution, the binary silicon carbide structures showing intermediate values, and elemental carbon structures showing the strongest bond energy contribution.

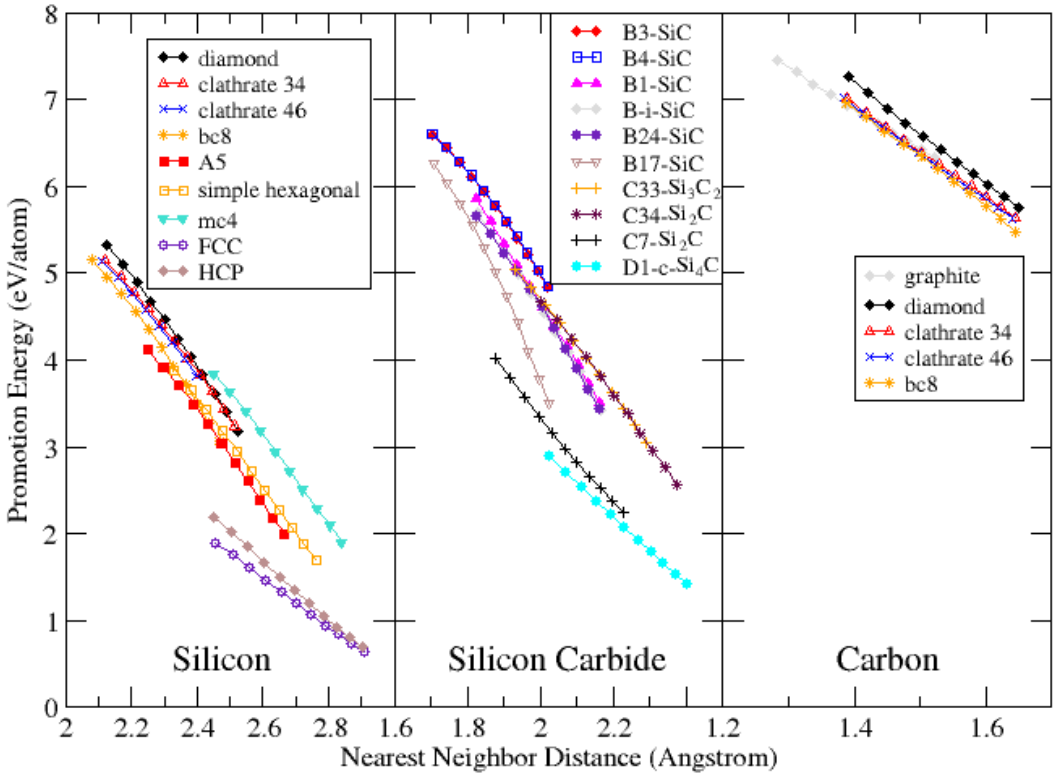

Fig. 5.24. Promotion energy contribution for select structures in the Si-C system.

The promotion energy contribution for select structures about equilibrium for silicon in Fig. 5.24 is smaller in magnitude in comparison with carbon, as was the case for the bond energy contribution. The structural promotion energy difference is relatively large, roughly a factor of three between FCC and diamond silicon, but the absolute energy difference between the different structures is small in comparison to the bond

energy contribution in Fig. 5.23. Still these energy differences are significant given that all the structures shown have binding energies within 1 eV/atom of one another.

The promotion energy contribution for the lowest energy silicon carbide structures about equilibrium again shows intermediate values in comparison with the larger contribution for elemental carbon and the weaker contribution for elemental silicon. There does not appear to be a clear composition effect with the B17 1:1 composition structure showing significantly different behavior compared to the other 1:1 composition structures and the C33 and C34 off 1:1 composition structures showing similar trends to the 1:1 composition structures.

The promotion energy contribution for carbon shows rather linear behavior for the lowest energy structures with equilibrium diamond having a value of roughly +6.5 eV, much smaller in magnitude than the negative bond energy contribution. Note that for a given nearest-neighbor distance, diamond shows the largest promotion energy, consistent with the chemical picture of sp^3 hybridization for the diamond structure. Nevertheless, compression clearly has a sizeable effect on orbital occupations as shown by the large promotion energies for graphite at small nearest-neighbor distances.

The repulsive energy contribution for select silicon structures about equilibrium in Fig. 5.25 is significantly smaller in magnitude than for carbon. The contribution is roughly three times as large as the positive promotion energy contribution for silicon in Fig. 5.24 and has a magnitude of roughly two-thirds the bond energy contribution

for silicon in Fig. 5.23. The effect from hard-core repulsion is not apparent as it begins at 2.0 Angstrom.

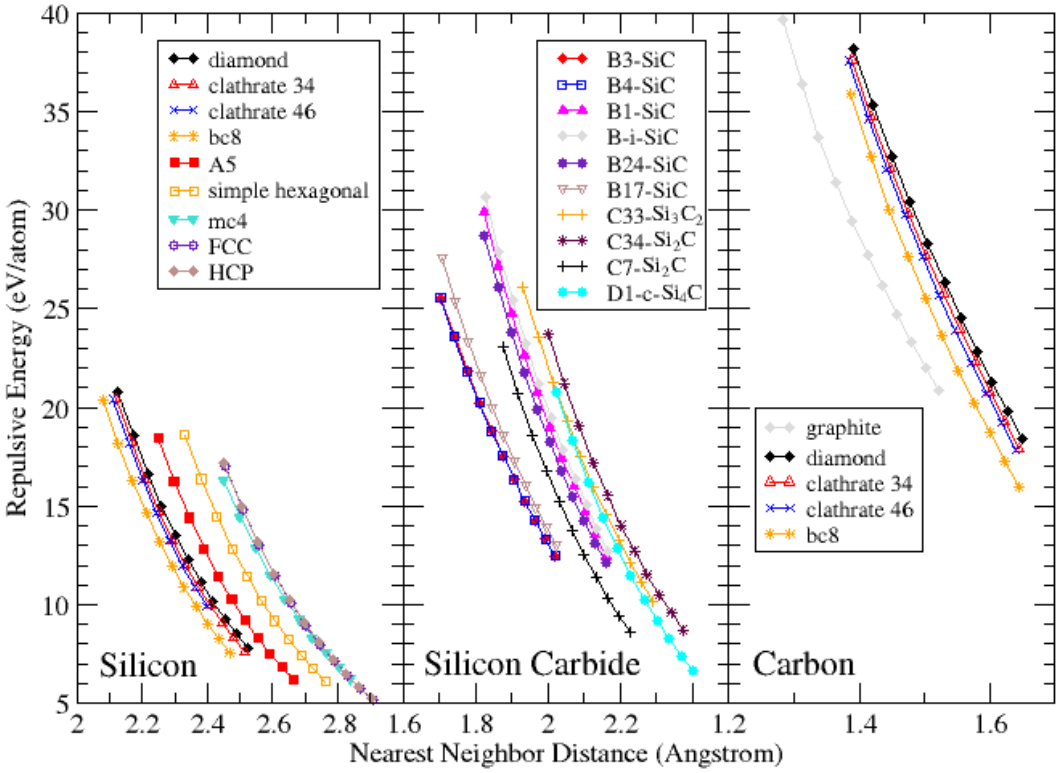

Fig. 5.25. Repulsive energy contribution for select structures in the Si-C system.

The repulsive energy contribution for silicon carbide show a similar trend to the binary bond energy contributions with the off 1:1 composition structures having smaller magnitude values. The distances dependence of the repulsive energy also shows structural dependencies with the B3, B4, and B17 structures appearing slightly less steep in Fig. 5.25. Here the repulsive energy magnitude is again roughly three times the magnitude of the promotion energy for the groundstate structure and roughly two-thirds the magnitude of the bond energy.

The repulsive energy contribution for carbon shows the effect of the hard-core repulsive function beginning under compression from 1.4 Angstrom. The repulsive energy contribution is significantly stronger than the positive promotion energy contribution shown in Fig. 5.24 and has a magnitude of roughly two-thirds the bond energy contribution shown in Fig. 5.23.

The relative magnitudes of the bond, promotion, and repulsive energy contributions are shown to be rather consistent between the elemental and binary systems. The absolute magnitudes are, however, significantly different between the systems. Elemental carbon structures show larger magnitude bond, promotion, and repulsive energy contributions, elemental silicon structures show smaller energy contributions, and the binary silicon carbide structures show intermediate values.

5.5 Equations of state results

To be more precise in specifying the equilibrium points for low energy structures, equation of state fits were completed on both the DFT reference binding energy curves and the reduced OTB model binding energy curves. Equilibirum binding energies, volumes, bulk moduli, and binding energies relative to the groundstate are shown for the ten lowest energy structures tested for the elemental and binary models. In all cases, the structures are orded relative to the DFT binding energy with the lowest, groundstate binding energy on the bottom.

Structure	$\Delta U_{binding}$	$U_{binding}^{Eq}$	*Eq Volume*	*Bulk Modulus*
A8	3.0097(2.5967)	-6.0218(-6.405)	6.0769(5.8048)	531.2526(337.0426)
st12	2.745(2.4929)	-6.2865(-6.5088)	6.1641(5.9708)	671.9644(337.2344)
A7	2.8644(2.3221)	-6.1671(-6.6797)	6.0563(5.516)	482.3706(371.3789)
A17	2.7399(2.2441)	-6.2916(-6.7577)	6.7664(6.6279)	264.6024(294.7329)
bct5	2.5751(2.0383)	-6.4564(-6.9634)	6.387(5.5704)	614.6659(391.0057)
bc8	0.6396(0.7517)	-8.3919(-8.2501)	5.2678(5.3077)	665.7421(469.5873)
Clathrate 46	0.1027(0.1594)	-8.9288(-8.8423)	6.4099(6.3269)	429.5318(400.913)
Clathrate 34	0.0604(0.1284)	-8.9712(-8.8734)	6.4794(6.4016)	429.4529(397.2958)
A9	0.0547(0.0086)	-8.9768(-8.9932)	8.5282(8.6349)	553.8216(288.4373)
Diamond	0.0(0.0)	-9.0315(-9.0018)	5.4158(5.521)	477.6604(461.3221)

Table 5.1. Equation of state fits for the ten lowest binding energy three-dimensional structures of carbon. All values are an arithmetic average of a 4th order polynomial and Murnaghan fit with reference DFT values given in parenthesis. Energies are in eV/atom, equilibrium volumes are in Angstrom^3, and bulk moduli are in GPa.

The equation of state fits for the ten lowest binding energy three-dimensional structures of carbon in Table 5.1 show no spurious groundstate structures, most easily noticed given all positive values for $\Delta U_{binding}$. Both DFT and the reduced OTB model show A9/graphite carbon being slightly higher in energy than diamond, with this difference being overestimated by the reduced OTB model. With similar coordinations and geometries, the clathrate structures are also close in energy, roughly 100 meV/atom higher than the groundstate for both DFT and the reduced OTB model. Beyond the bc8 structure, roughly 700 meV/atom higher in energy than diamond, both DFT and the reduced OTB model show a significant jump in energy with the next most stable structures being over 2 eV/atom higher in energy than the groundstate. There is fair agreement between the absolute DFT and reduced OTB binding energies with the groundstate diamond structure 30 meV/atom too stable in the reduced OTB model. The diamond and A9/graphite equilibrium volumes are both slightly too small relative to DFT, with higher-energy structures showing both too large and too small values for the equilibrium volume. Besides the A17 structure, the

bulk moduli are all significantly too large. The bulk modulus for the diamond structure is actually reproduced fairly well, within 4% of DFT, but due to the effect of the hard-core repulsive term, the A9/graphite bulk modulus is too large by roughly a factor of 2.

Structure	$\Delta U_{binding}$	$U_{binding}^{Eq}$	*Eq Volume*	*Bulk Modulus*
Ai	0.5748(0.3478)	-4.8323(-5.0005)	14.3971(15.2777)	250.8097(106.6736)
bct5	0.5779(0.2827)	-4.8292(-5.0655)	16.2401(17.1799)	205.312(98.6652)
Simple cubic	0.4626(0.2768)	-4.9445(-5.0714)	14.5804(15.6648)	235.9283(108.2999)
mc4	0.334(0.2733)	-5.0731(-5.0749)	13.9282(14.8458)	286.7623(111.0085)
Simple hexagonal	0.1257(0.2527)	-5.2814(-5.0955)	13.9688(14.5963)	283.6569(112.3168)
A5	0.1826(0.2078)	-5.2245(-5.1404)	13.8331(14.8254)	298.8188(115.8006)
bc8	0.3944(0.1254)	-5.0128(-5.2228)	17.1239(17.888)	189.4295(102.1853)
Clathrate46	0.0314(0.0863)	-5.3757(-5.2619)	21.4259(22.4863)	166.3346(84.59)
Clathrate34	0.0057(0.0783)	-5.4014(-5.2699)	21.658(22.7736)	162.7584(82.3015)
Diamond	0.0(0.0)	-5.4071(-5.3482)	18.8264(19.7266)	175.4172(95.1328)

Table 5.2. Equation of state fits for the ten lowest binding energy three-dimensional structures of silicon.

The equation of state fits for the ten lowest binding energy three-dimensional structures of silicon in Table 5.2 again show no spurious groundstate structures, with all positive values for $\Delta U_{binding}$. Significantly different in comparison with carbon, the ten lowest binding energy structures for silicon are all rather close in energy with DFT binding energies within 350 meV/atom. The ordering of the diamond and two clathrate structures is correct for the reduced OTB model, but higher-energy bc8, A5, and simple hexagonal structures are not ordered correctly, as was shown in Fig. 5.16. The absolute binding energies for the groundstate diamond structure are 59 meV/atom too low for the reduced OTB model compared with DFT. In general, it was difficult to improve the relative and absolute energies without creating a spurious groundstate structure. The equilibrium volumes for the ten lowest binding energy structures are all too small relative to DFT with the diamond structure within 5%. The

bulk moduli are all significantly too large with the diamond structure off by almost a factor of 2.

Structure	$\Delta U_{binding}$	$U_{binding}^{Eq}$	*Eq Volume*	*Bulk Modulus*
B34-SiC	2.3553(1.1473)	-5.1098(-6.3067)	12.1816(9.4202)	125.3724(200.5275)
C33-Si_3C_2	1.4447(1.138)	-6.0204(-6.3159)	11.2439(9.5057)	296.8715(200.6391)
C18-SiC_2	1.7739(1.0976)	-5.6913(-6.3564)	9.3292(8.7253)	205.4841(238.0919)
B18-SiC	2.1008(1.0624)	-5.3644(-6.3916)	13.0664(11.1192)	142.3627(188.0745)
B17-SiC	2.4532(0.9416)	-5.0119(-6.5123)	13.3687(9.8568)	86.0367(204.9055)
B24-SiC	1.7332(0.7591)	-5.732(-6.6948)	10.4334(8.3995)	268.6618(253.2346)
B-i-SiC	1.5128(0.6853)	-5.9524(-6.7686)	11.0449(8.1104)	293.6967(275.3423)
B1-SiC	1.4385(0.67)	-6.0266(-6.784)	10.5942(8.0602)	280.631(264.634)
B4-SiC	0.0097(0.0026)	-7.4554(-7.4514)	10.2321(10.164)	217.6465(227.0085)
B3-SiC	0.0(0.0)	-7.4651(-7.454)	10.2011(10.16)	216.3329(226.1639)

Table 5.3. Equation of state fits for the ten lowest binding energy three-dimensional structures of silicon carbide.

The equation of state fits for the ten lowest binding energy three-dimensional structures of silicon carbide in Table 5.3 also show no spurious groundstate structures with all positive values for $\Delta U_{binding}$. Here the structural energy differences are larger than for silicon but smaller than for carbon. The B4 polytype is very close in energy to B3, within 10 meV/atom for both DFT and reduced OTB. Besides the tetrahedral polytypes, the next closest binding energy structures within DFT are over 600 meV/atom higher in energy. A sizeable gap is also shown by the reduced OTB model but is overestimated at over 1.4 eV/atom. These higher-energy structures are properly destabilized in the reduced OTB model, but the structural ordering is not reproduced. The absolute binding energies for the tetrahedral polytypes are reproduced fairly well with the B3 binding energy too low by 11 meV/atom. The equilibrium volume for the B3 structure is overestimated by 4%, whereas the higher-energy structures show significantly larger overestimation of the equilibrium volumes.

The equations of state are reproduced fairly well for the elemental and binary groundstate structures. This was to be expected as the repulsive parameters were fit particularly to best reproduce the groundstate binding energy curves. The energies, volumes, and bulk moduli for higher-energy structures were not always in agreement between DFT and the reduced OTB model even though that also was a goal of the fitting process. Many of the equations of state could be reproduced much more accurately, but at the cost of predicting a spurious groundstate structure. Using the large testing database to search for spurious groundstate structures therefore limited the accuracy in many cases but made the reduced OTB model more robust.

5.6 Heats of formation

Using the equation of state fits discussed in Section 5.5, heats of formation have been calculated for all the structures in the binary testing database. Given the composition-dependent reference energy, this indication of the thermodynamic stability of various crystal structures at 0 K helps to identify particularly which structures may form or be more stable even if the absolute binding energies shown in Section 5.2 are higher.

The heats of formation for binary Si-C structures up to 1 eV/atom in Fig. 5.26 show a rather simple convex hull including only the tetrahedral polytype structures at 1:1 composition and the reference elemental diamond groundstate structures for pure carbon and silicon. For clarity, only the B3 and B4 polytypes are shown, but all other polytype energies tested are within 10 meV/atom as was discussed in Section 5.2. The reduced OTB model successfully reproduces the convex hull, with the tetrahedral polytype structures being the only structures with negative heats of formation. The DFT heat of formation for the B3 structure is -0.279 eV/atom, and the reduced OTB

heat of formation is -0.246 eV/atom. The binary structures with the next lowest heats of formation in the database are also 1:1 composition structures but have heats of formation of roughly +0.4 eV/atom. As was discussed in Section 5.2, the binding energy for the B1 structure was not reproduced well, but nevertheless was destabilized relative to the tetrahedral polytype structures. Other binary structures with relatively low heats of formation tend to be Si-rich given the composition range shown in Fig. 5.26, but still have significantly positive values from both DFT and reduced OTB.

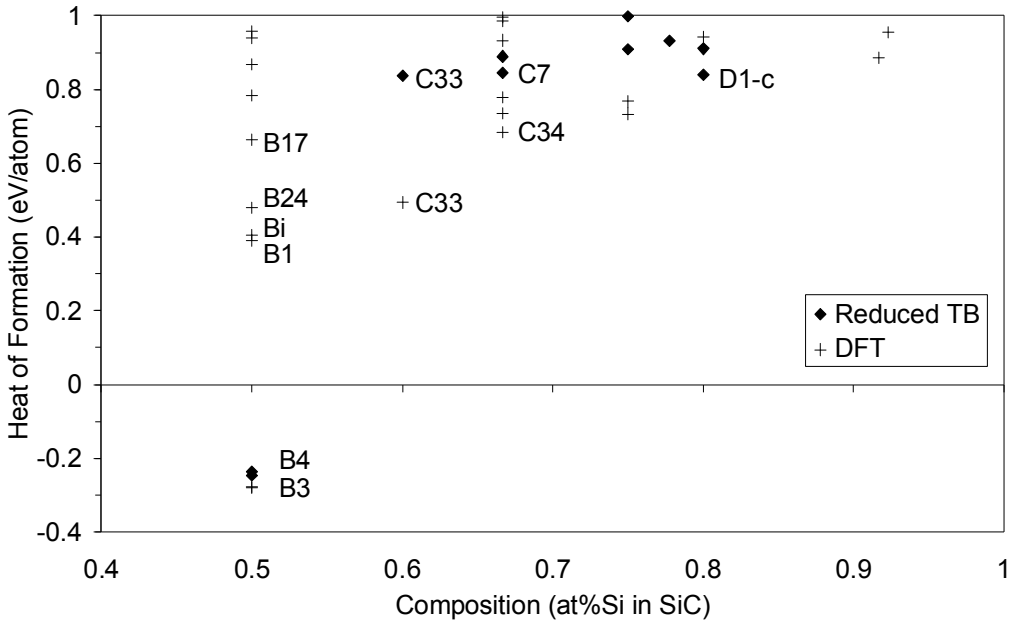

Fig. 5.26. Heats of formation for binary Si-C structures up to 1 eV/atom. Low energy structures as per DFT and reduced OTB are labeled.

The heats of formation, including even higher-energy binary Si-C structures from the testing database are shown in Fig. 5.27. Again, the only structures with negative heats of formation are the tetrahedral polytype structures at 1:1 composition. Even more apparent than in Fig. 5.26, the Si-rich structures tend to have lower heats of formation than the C-rich structures, both within DFT and reduced OTB. Fig. 5.27 also gives a

good indication of the breadth of composition space within the binary test bed, with compositions within every decile. This successful reproduction of the convex hull is good indication that the reduced OTB would be robust when modelling thin film growth or any other process with spatial or temporal variations in composition.

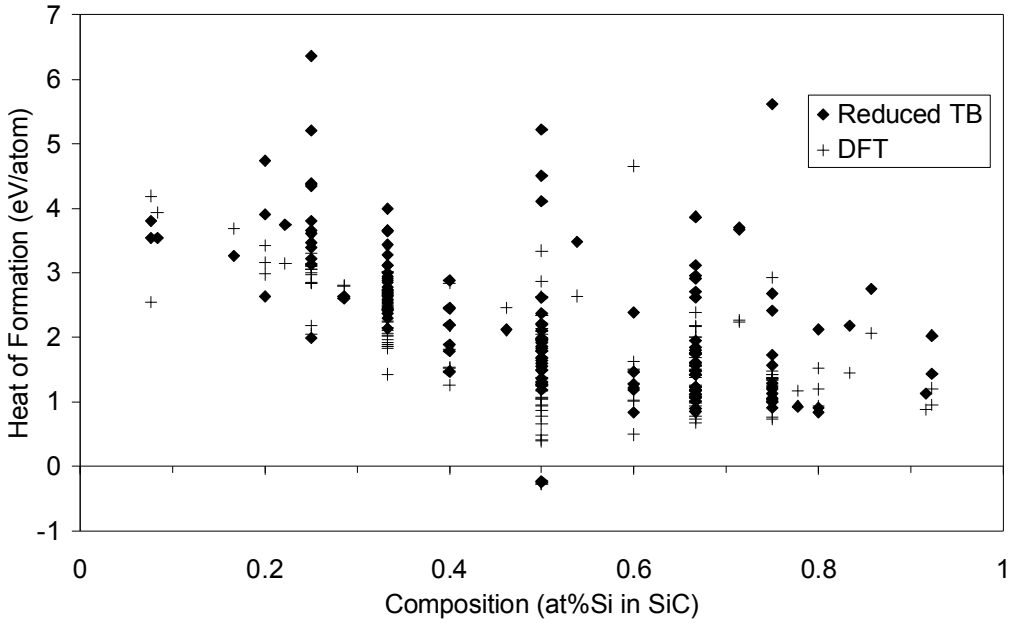

Fig. 5.27. Heats of formation for binary Si-C structures from testing database. Note only the tetrahedrally coordinated polytype structures were found to have negative heats of formation.

5.7 Elastic constants

The elastic constants for diamond carbon, diamond silicon, and B3 silicon carbide are shown in this section as a test of the stability of these structures to certain modes of deformation. For each system, experimental, DFT, other OTB, and empricial potential values are provided for comparison. Note that in all cases only the C_{44} elastic constant is sensitive to whether internal degrees of freedom are allowed to relax or not.

	Exp.	DFT	Reduced OTB	OTB Xu	EA 05	EDIP A	EDIP B	B90	T89
a (Ang)	3.567	3.528	3.512	3.552	3.566	3.535	3.561	3.566	3.566
$U_{binding}$ (eV/atom)		-9.030	-9.032	-9.030	-7.373	-7.382	-7.370	-7.324	-7.371
B (GPa)	444	460	478	468	445	438	441	484	425
B'	~4		6.20	3.0	4.15			4.06	3.92
C_{11} (GPa)	1081	1100	1030	881	1082	1057	1079	621	1067
C_{12} (GPa)	125	143	198	265	127	127	121	415	104
C_{11}-C_{12} (GPa)	956	957	832	616	955	930	958	206	963
C_{44} (GPa)	579	587	198	158	635	480	490	383	636
C_{44}^0 (GPa)			211	178	673	543	551	642	671
A	1.21	1.23	0.48	0.51	1.33	1.03	1.02	3.72	1.32

Table 5.4. Elastic constant values for diamond carbon [3, 11]. Note C_{44}^0 is the static (unrelaxed) shear modulus and A is the Zener anisotropy ratio, $A = 2C_{44}/(C_{11} - C_{12})$.

The elastic constant values for diamond carbon are shown in Table 5.4. Note that all the elastic constants are positive, or stable to the different modes of deformation. For all the elastic constants, there are significant differences between the reduced OTB values and the reference experimental or DFT values. The reduced OTB model values do, however, consistently improve on the results from Xu's OTB model, which were recalculated for this study. Except for Brenner's 1990 model, many of the empirical potentials better reproduce this near equilibrium stability, particularly for the C_{12} and C_{44} elastic constants.

	Exp.	DFT	Reduced OTB	OTB Kwon	EA 05 1	EA 05 2	DS	LSA	EDIP A	EDIP B	SW	T89
a (Ang)	5.429	5.400	5.320	5.443	5.429	5.429	5.432	5.430	5.430	5.425	5.431	5.432
$U_{binding}$ (eV)	-4.63	-5.348	-5.407	-5.348	-4.63	-4.63	-4.63	-4.61	-4.65	-4.647	-4.63	-4.63
B (GPa)	99	93	175	81	99	99	98	110	99	101	108	98
B'	4.2	3.8	3.87	2.4	4.43	4.36					2.93	4.3
C_{11} (GPa)	168	159	275	147	167	167	109	165	175	155	162	143
C_{12} (GPa)	65	61	131	55	65	65	93	82	65	75	82	75
C_{11}-C_{12} (GPa)	103	98	144	92	102	102	16	83	110	80	80	68
C_{44} (GPa)	80	85	47	29	60	72	38	72	71	59	60	69
C_{44}^0 (GPa)		111	163	66	105	111	114		112	111	117	119
C_{12}-C_{44} (GPa)	-15	-24	84	26	5	-7	55	10	-6	16	22	6

Table 5.5. Elastic constant values for diamond silicon [3, 11]. Note C_{44}^0 is the static (unrelaxed) shear modulus.

The reduced OTB elastic constant values for diamond silicon in Table 5.5 also show significant differences with the reference experimental and DFT values. Still, all models show positive values, indicating stability to the certain modes of deformation. Kwon's OTB model results which were recalculated for this study show closer agreement, except for C_{44}, but the model was also found to have a spurious clathrate groundstate structure. Again, many of the empirical potentials better reproduced this near equilibrium stability.

	Exp.	DFT	Reduced OTB	EA 05	EDIP A	EDIP B	T89	T90	T94	GW	V 07
a (Ang)	4.3596	4.344	4.338	4.359	4.411	4.364	4.321	4.307	4.28	4.36	4.3581
$U_{binding}$ (eV)	-6.34	-7.415	-7.465	-6.34	-6.359	-6.338	-6.165	-6.21	-6.434	-6.412	-6.341
B (GPa)	225	222	216	224	224	226	225	231	241	235	225.2
B'			4.28	4.16							
C_{11} (GPa)	390	390	445	382	437	394	437	426	447	254	390
C_{12} (GPa)	142	134	107	145	117	142	118	134	134	225	152.6
C_{11}-C_{12} (GPa)	248	256	338	237	320	252	319	292	313	29	237.4
C_{44} (GPa)	256	253	90	240	195	168	311	280	293	66	191
C_{44}^0 (GPa)		273	97	305	260	255					
A	2.06	1.98	0.53	2.03	1.22	1.33	1.95	1.92	1.87	4.55	1.61

Table 5.6. Elastic constant values for B3 silicon carbide [1-4]. Note C_{44}^0 is the static (unrelaxed) shear modulus and A is the Zener anisotropy ratio, $A = 2C_{44}/\left(C_{11} - C_{12}\right)$.

The reduced OTB elastic constant values for B3 silicon carbide are shown in Table 5.6. The C_{44} lattice parameter is significantly too low in comparison with reference experimental or DFT values, but C_{11} and C_{12} are much closer. All models again show positive values indicating the stability of the ideal structure relative to these modes of deformation. All of the empirical potentials show fairly good agreement with the reference values, except the Gao and Weber model, and tend to better reproduce this near equilibrium stability than the reduced OTB model.

The elastic constants in this section indicate the stability of the ideal diamond and B3 structures to certain modes of deformation. In all cases the reduced OTB model reproduced positive values as found in the reference experimental and DFT data. For all the systems, certain empirical potentials were better able to reproduce the elastic constants for these structures. However, as was found in Kwon's OTB model for silicon, spurious groundstate structures may exist for other models, particularly if they were not thoroughly tested using a large database of structures. As highlighted elsewhere, in the current work there was a significant comprise between reproducing near-equilibrium behavior and correcting any spurious groundstate structures.

5.8 Point defect energies

As a further test of the reduced OTB model, relaxed point defect energies have been calculated in elemental diamond carbon and silicon as well as B3 SiC based on 216 atom supercells. Point defect energies from other commonly used models are reported as well. The defect energies are reported as antisite pair or Frenkel pair energies, removing any ambiguity regarding the reference chemical potentials between different models. All point defects are calculated individually, so the reported pair energies correspond to energetically separated point defects as opposed to nearest-neighbor or other nearby point defect pairs. The notation used indicates the species of the defect atom with the first label, and then the site where the defect atom is placed. The interstitial sites T, B, and H correspond to tetrahedral, bond, and hexagonal interstitial sites. The interstitial site label is then followed by the species of the surrounding nearest-neighbor atoms. So, C_Tsi corresponds to a carbon interstitial in a tetrahedral site surrounded by silicon atoms. Dumbbell interstitial defects are labeled with the species of the original atom at that site and the crystallographic

orientation of the dumbbell. So, C_c100 corresponds to a carbon dumbbell interstitial with another carbon atom in the 100 direction.

C Point Defects	DFT	Reduced OTB	EA05	T88	Brenner
C_Tc Frenkel	30.6	28.67	29.14	22.84	17.92
C_c100 Frenkel	23.7	25.49	15.45	13.35	14.20
C_Bc Frenkel	22.8	29.42	21.3	17.88	17.99

Table 5.7. Energetically separated Frenkel pair defect energies in diamond carbon [1-3]. Note that all defect energies are given in eV.

Energetically separated Frenkel pair defect energies in diamond carbon are shown in Table 5.7. DFT shows the bond-centered C_Bc Frenkel pair to be the lowest in energy at 22.8 eV. None of the other models reproduce the C_Bc Frenkel as the lowest energy defect. For the reduced OTB model and the other interatomic potentials, the C_c100 Frenkel is the lowest energy point defect pair in diamond carbon. All the empirical potentials show Frenkel pair formation energies which are over 7 eV too small in comparison with DFT. This difference is less than 3 eV for the current reduced OTB model.

Si Point Defects	DFT	Reduced OTB	EDIP	EA05	T88	SW	LSA
Si_Tsi Frenkel	7.2	13.74	7.27	6.7	7.15	8.07	6.30
Si_Hsi Frenkel	7	16.29	7.38	7.2	8.31	9.77	6.51
Si_si110 Frenkel	6.9	13.09	6.57	7.6	8.1	7.5	6.43

Table 5.8. Energetically separated Frenkel pair defect energies in diamond silicon [1, 2, 6, 7]. Note that all defect energies are given in eV.

Energetically separated Frenkel pair defect energies in diamond silicon are shown in Table 5.8. DFT shows the Si_si110 Frenkel to be the lowest in energy. This is reproduced by the reduced OTB model, the EDIP model, and the Stillinger-Weber

model. The Erhart and Albe, Tersoff, and Lenosky-Sadigh-Alonso models predict the Si_Tsi Frenkel to be lowest in energy. The reduced OTB model, however, predicts absolute defect energies which are much higher than DFT with the lowest energy Si_si110 Frenkel at 13.09 eV. In this respect the agreement is rather poor in comparison with common interatomic potentials.

SiC Point Defects	DFT	Reduced OTB	EDIP A	EDIP B	EA05	T89	GW02	V07
C_si+Si_c	7.5	8.50	5.84	5.14	4.9	6.7	9.48	27.3
C_Tc Frenkel	C_c100	17.34	13.4	C_c100	14.53	11.09	7.41	
C_Tsi Frenkel	C_c100	18.03	9.82	7.85	11.28	8.28	7.08	12.625
C_c100 Frenkel	9.94	13.98	6.67	6.27	6.68	10.38	5.8	14.541
C_c110 Frenkel	10.28	14.06	C_si100	6.58	11.79	9.56	6.06	
C_si100 Frenkel	10.57	15.89	7.3	6.12	10.21	11.57	6.19	
C_si110 Frenkel	C_c100	14.44	C_c100	C_c100	6.71	C_c100	6.71	unstable
Si_Tc Frenkel	14.52	29.11	Si_c100	Si_c110	22.10	20.96	7.27	7.511
Si_Tsi Frenkel	16.71	30.80	Si_c100	Si_c110	21.85	19.18	10.07	
Si_si100 Frenkel	16.8	28.85	12.86	12.43	25.45	15.81	8.83	
Si_si110 Frenkel	15.59	27.80	13.66	Si_c110		15.4		
Si_c100 Frenkel	Si_si110	28.62	13.27	13.08	18.69	Si_si110	10.84	
Si_c110 Frenkel	Si_Tc	27.03	13.46	11.96		15.68		

Table 5.8. Energetically separated Frenkel pair and antisite pair defect energies in B3 SiC [1-4]. Note that all defect energies are given in eV.

Energetically separated Frenkel pair and antisite pair defect energies in B3 SiC are shown in Table 5.8. The DFT antisite pair energy is 7.5 eV, which is best reproduced by the Tersoff model at 6.7 eV. The reduced OTB model is next closest with a slightly overestimated value of 8.5 eV. Given the purely repulsive elemental interactions, the Vashishta value of 27.3 eV is over 19 eV too large. The most stable carbon interstitial within DFT is the C_c100 interstitial with a Frenkel energy of 9.94 eV. A number of the models were able to reproduce the C_c100 interstitial being the most stable carbon interstitial, including the reduced OTB model. Out of those models none are within 3 eV of the absolute Frenkel pair energy from DFT, and the reduced OTB model is the only one to overestimate the Frenkel pair energy at 13.98

eV. The Si_Tc Frenkel is the lowest energy silicon Frenkel pair in B3 SiC within DFT at 14.52 eV, significantly higher than the carbon Frenkel pair formation energy. Only the Gao-Weber potential was able to reproduce Si_Tc as the lowest energy silicon Frenkel pair, although the defect formation energy is too small by roughly a factor of 2. Across all the silicon interstitial point defects, the reduced OTB model predicts Frenkel energies which are too large in comparison with DFT. Overall, silicon point defect energies in B3 SiC are not reproduced very well by any of the models.

The point defect pair tests indicate that the reduced OTB model shows some improvements in defect energetics in comparison to certain interatomic potentials. Overall, none of the models reproduce the elemental or binary point defect energies very well. Either the relative ordering is incorrect or absolute defect energies tend to be significantly different in comparison with DFT. This continues to be a challenge in modelling the Si-C system.

5.9 Summary

The reduced OTB model presented in Section 4.2 has been tested by looking at the electronic structure, binding energies, and point defect relaxations. Section 5.1 reviewed the electronic structure for a number of elemental and binary crystal structures showing fairly good reproduction of the DFT electronic structure for the groundstate structures. Higher-energy structures were not always reproduced well, particularly for the binary B1 and B2 structures. Given these electronic structure tests, one could expect fairly good binding energy agreement for the groundstate structures and slightly larger errors for the higher-energy structures.

Section 5.2 showed binding energy results for the elemental and binary systems, indeed showing good agreement for the lowest energy groundstate structures and significantly larger errors for the higher-energy structures. It was, however, particularly difficult to reproduce the diamond silicon binding energy curve accurately without creating other spurious groundstate structures for elemental silicon. Nevertheless, the model presented in Section 4.2 has been tested with a large database of crystal structures and no spurious groundstate structures have been found in the Si-C system.

The coordination shell histograms and the energy contributions described in Sections 5.3 and 5.4 provide a reference for where the reduced OTB pairwise distance-dependent functions tend to be accessed, and what the resultant bond, promotion, and repulsive energies are for structures of interest. The coordination shell histograms further gave an indication of the distance sampling of the pairwise distance-dependent functions, showing thorough sampling for all elemental and binary functions.

The equations of state shown in Section 5.5 provided further information regarding the equilibrium points of the ten lowest energy structures in the elemental and binary test beds. In general, the groundstate structures were reproduced fairly well and higher-energy structures tended to show larger errors. Further making use of the fitted equations of state, the heats of formation were shown in Section 5.6. The convex hulls matched for the reduced OTB model and DFT, a further indication of robustness of the reduced OTB model.

Finally, distortions about the groundstate equilibrium structures were tested through the elastic constants and relaxed point defect energies in Sections 5.7 and 5.8. The elastic constants were reproduced somewhat better by certain interatomic potentials, but within the current work, it was difficult to improve the equilibrium behavior without creating a spurious groundstate structure. The rather thorough testing for other groundstate structures therefore limited the accuracy of the elemental diamond and binary B3 structures. None of the models presented for the point defect relaxations rendered good agreement both with relative defect energy ordering and absolute energy values. Although reproducing the DFT point defect energetics continues to be a challenge in the Si-C system, the reduced OTB model gives a fair description, particularly for the absolute Frenkel pair energies for elemental carbon, especially given that the defect structures were not included in the fitting database.

6 Conclusions

As SiC is well known to be useful as an electronic and structural material, much research has been done in pursuit of sufficiently fast and accurate models to study SiC through computer simulation. Since the energy differences are roughly on the same order as the accuracy of the computational methods being use, models for SiC have not focused on the various polytypes of SiC. Instead, models have focused on reproducing the elastic, thermal, and mechanical properties of the common B3 SiC, and to a lesser extent, to reproduce the high-pressure structural transformation to the B1 structure.

Interatomic potentials used to model Si-C have had some successes but also some significant deficiencies in both functional form and calculated results as discussed in Chapter 3. The neglect of π-bonding effects is well known with the accompanying linear structures, which should be bent. A correction for the dihedral rotational barrier in conjugated systems has improved results but not fixed the omission of explicit π-bonding. The coarse-graining of DFT to TB to analytic BOPs has shown good promise in addressing some of these deficiencies. In that sense, a reduced OTB model for SiC is an important step towards the development of an analytic BOP for SiC. Strictly within TB, a simple selfconsistent OTB model parameterized specifically for SiC did not exist, further showing the importance of a reduced OTB model for SiC.

The reduced OTB model for SiC presented in Chapter 4 was parameterized specifically for SiC without any averaging techniques as a selfconsistent model

through LCN. Hamiltonian parameters were fit directly to DFT-projected data for elemental and binary structures, and repulsive parameters were fit to DFT binding energies. Errors associated with the polynomial form for the repulsive embedding function used in the popular Kwon et al. and Xu et al. models for silicon and carbon [4, 5, 7] were addressed by using a simple power-law embedding function. Additional effects from hard-core repulsion were included through the fitting of a screened Yukawa-type potential. The reduced form of the OTB model ensures that there is a single scalar σ bond order contributing to the bond energy making good connection with the concept of the bond order as used in chemistry and interatomic potentials.

The electronic structure of the reduced OTB model shows good agreement with DFT for all the groundstate elemental diamond and binary B3 structures. The binding energies of those groundstate structures were also reproduced well, with the elemental diamond silicon model showing the largest errors. Higher-energy structures were not always reproduced accurately but in all cases were destabilized with the reduced OTB model showing no spurious groundstate structures, an improvement on the Kwon et al. model for Si [7]. Even where less quantitative agreement was obtained, much of the DFT structural ordering was captured. The results from the large test beds give a strong indication that the reduced OTB model will be robust to different coordinations, geometries, compositions, or nearest-neighbor distances. Given the poor reproduction of the B1 electronic structure and subsequent binding energy fit, the reduce OTB model would however, have limited accuracy in modeling the high-pressure phase transformation to the B1 structure.

The reduced OTB model successfully captured the convex hull of the Si-C heats of formation with only the 1:1 composition tetrahedral polytype structures showing negative values in good quantitative agreement with DFT. This provides good indication of the usefulness of the reduced OTB model in situations with varying composition, as found in CVD or PVD thin film growth.

Ensuring as best as possible that no spurious groundstate structures would be predicted proved difficult. Therefore, the near-equilibrium groundstate structure behavior was in less quantitative agreement than for some interatomic potentials, particularly for silicon. Nevertheless all elastic constants were positive and some improvements were seen in relaxed point defect energies, particularly for the absolute Frenkel pair energies in elemental carbon.

Overall, the reduced OTB model for SiC shows good improvements over the existing OTB models for the Si-C system and provides an important basis for further analytic BOP development.

7 Appendix

All the crystal structures tested with binding energies reviewed in Section 5.2 are listed here. The elemental carbon structures are given in Table A.1.

A4	A13	Ai	dimer	hr13	st12
A5	A14	bc8	FCC	hr22	st12-W
A6	A15	BCC	Gamc4	linear chain	tp30
A7	A17	bct5	Gaoc4	mp16	Uoc4
A8	Aa	C19	graphene	mp4	45° armchair chain
A9	Ab	ci12	HCP	of 8	90° zigzag chain
A10	Ac	Clathrate34	hp12	of 8 back	
A11	Ad	Clathrate46	hp4	simple cubic	
A12	Ag	diamond	hp7	simple hexagonal	

Table A.1. All carbon crystal structures tested.

The elemental silicon crystal structures are given in Table A.2.

A5	A15	bct5	graphene	mp4
A6	A17	C19	HCP	of 8
A7	A20	ci12	hp12	simple cubic
A8	Aa	clathrate 34	hp4	simple hexagonal
A9	Aaback	clathrate 46	hp7	st12
A10	Ab	diamond	hr13	st12-W
A11	Ac	dimer	hr22	tp30
A12	Ad	FCC	linear chain	Uoc4
A13	Ai	Gamc4	mc4	45° armchair chain
A14	bc8	Gaoc4	mp16	90° zigzag chain

Table A.2. All silicon crystal structures tested.

The binary silicon carbide crystal structures are given in Table A.3.

A15-Si_3C	B34-SiC	C10-Si_4C_8	C35-C_2Si_4	D0-9-CSi_3	D2-b-CSi_{12}	D8-5-Si_6C_7
A15-SiC_3	B35-SiC	C14-Laves-C_2Si	C36-Laves-Si_2C	D0-9-SiC_3	D2-b-SiC_{12}	D8-h-C_5Si_2
B1-SiC	B37-SiC	C15-Laves-Si_2C	C36-Laves-SiC_2	D0-11-CSi_3	D2-d-CSi_5	D8-h-Si_5C_2
B2-SiC	B-a-SiC	C15-Laves-SiC_2	C37-CSi_2	D0-11-SiC_3	D2-d-SiC_5	D8-i-C_5Si_2
B3-SiC	B-b-Si_2C	C16-C_2Si_4	C37-SiC_2	D0-14-CSi_3	D2-e-CSi_{11}	D8-i-Si_5C_2
B4-SiC	B-b-SiC_2	C16-Si_2C_4	C38-CSi_2	D0-14-SiC_3	D2-e-SiC_{11}	L1-0-SiC
B8-1-SiC	B-e-SiC	C18-C_2Si_4	C38-SiC_2	D0-17-CSi_3	D2-f-CSi_{12}	L1-1-Csi
B8-2-Si_2C	B-g-SiC	C18-Si_2C_4	C40-CSi_2	D0-17-SiC_3	D2-f-SiC_{12}	L1-1-SiC
B8-2-SiC_2	B-h-SiC	C21-CSi_2	C40-SiC_2	D0-18-CSi_3	D5-11-C_3Si_2	L1-2-CSi_3
B10-SiC	B-i-SiC	C21-SiC_2	C43-CSi_2	D0-18-SiC_3	D5-11-Si_3C_2	L1-2-SiC_3
B11-SiC	C1-CSi_2	C22-CSi_2	C43-SiC_2	D0-19-CSi_3	D5-19-C_3Si_2	L1-3-CSi_3
B16-SiC	C1-SiC_2	C22-SiC_2	C46-CSi_2	D0-19-SiC_3	D5-19-Si_3C_2	L1-3-SiC_3
B17-SiC	C3-CSi_2	C23-CSi_2	C46-SiC_2	D0-a-CSi_3	D5-1-C_3Si_2	L2-2-C_2Si_7
B18-SiC	C3-SiC_2	C23-SiC_2	C54-CSi_2	D0-a-SiC_3	D5-1-Si_3C_2	L2-2-Si_2C_7
B20-SiC	C4-CSi_2	C24-CSi_2	C54-SiC_2	D0prime-c-CSi_3	D5-8-C_3Si_2	Lprime2-CSi_2
B24-SiC	C4-SiC_2	C24-SiC_2	C-a-CSi_2	D1-3-CSi_4	D5-8-Si_3C_2	Lprime2-SiC_2
B26-CSi	C5-CSi_2	C25-CSi_2	C-a-SiC_2	D1-3-SiC_4	D5-a-C_3Si_2	L6-0-CSi_3
B26-SiC	C5-SiC_2	C25-SiC_2	C-h-CSi_2	D1-a-CSi_4	D5-a-Si_3C_2	L6-0-SiC_3
B27-SiC	C7-CSi_2	C32-CSi_2	C-h-SiC_2	D1-a-SiC_4	D5-c-C_3Si_2	
B29-SiC	C8-CSi_2	C33-C_3Si_2	D0-2-CSi_3	D1-c-CSi_4	D5-c-Si_3C_2	
B31-SiC	C8-SiC_2	C33-Si_3C_2	D0-2-SiC_3	D1-c-SiC_4	D5-e-C_3Si_2	
B33-SiC	C9-CSi_2	C34-CSi_2	D0-5-CSi_3	D2-1-CSi_6	D5-e-Si_3C_2	
B34-CSi	C9-SiC_2	C34-SiC_2	D0-5-SiC_3	D2-1-SiC_6	D8-5-C_6Si_7	

Table A.3. All silicon carbide crystal structures tested.

Tables A.1, A.2, and A.3 list all the structures shown in all figures reporting values for ‘all tested structures’.

8 References

[1] J. Tersoff, Physical Review B 39 (1989) 5566.

[2] D. W. Brenner, Physical Review B 42 (1990) 9458.

[3] P. Erhart, K. Albe, Physical Review B 71 (2005) 035211.

[4] M. Mrovec, M. Moseler, C. Elsässer, P. Gumbsch, Progress in Materials Science. Reprinted with permission from Elsevier. 52 (2007) 230-254.

[5] C. H. Xu, C. Z. Wang, C. T. Chan, K. M. Ho, A transferable tight-binding potential for carbon. Journal of Physics: Condensed Matter. Institute of Physics. http://iopscience.iop.org/0953-8984/4/28/006 4 (1992) 6047-6054.

[6] R. Drautz, X. W. Zhou, D. A. Murdick, B. Gillespie, H. N. G. Wadley, D. G. Pettifor, Progress in Materials Science. Reprinted with permission from Elsevier. 52 (2007) 196-229.

[7] I. Kwon, R. Biswas, C. Z. Wang, K. M. Ho, C. M. Soukoulis, Physical Review B. "Copyright 1994 by the American Physical Society." http://link.aps.org/abstract/PRB/v49/p7242 49 (1994) 7242.

[8] D. G. Pettifor, I. I. Oleinik, Physical Review B. "Copyright 2002 by the American Physical Society." http://link.aps.org/abstract/PRB/v65/p172103 65 (2002) 172103.

[9] M. S. Tang, C. Z. Wang, C. T. Chan, K. M. Ho, Physical Review B. "Copyright 1996 by the American Physical Society." Readers may view, browse, and/or download material for temporary copying purposes only, provided these uses are for noncommercial personal purposes. Except as provided by law, this material may not be further reproduced, distributed, transmitted, modified, adapted, performed, displayed, published, or sold in whole or part, without prior written permission from the American Physical Society. http://link.aps.org/abstract/PRB/v53/p979 53 (1996) 979.

[10] B. A. Gillespie, X. W. Zhou, D. A. Murdick, H. N. G. Wadley, R. Drautz, D. G. Pettifor, Physical Review B. "Copyright 2007 by the American Physical Society." http://link.aps.org/abstract/PRB/v75/e155207 75 (2007) 155207-155210.

[11] M. B. G. Lucas, L. Pizzagalli, Journal of Physics: Condensed Matter 22 (2010).

[12] M. Lattemann, S. Ulrich, H. Holleck, M. Stüber, H. Leiste, Diamond and Related Materials 11 (2002) 1248-1253.

[13] P. Vashishta, R. K. Kalia, A. Nakano, J. P. Rino, Journal of Applied Physics 101 (2007) 103515-103512.

[14] R. W. Olesinski, G. J. Abbaschian, Binary Alloy Phase Diagrams, ASM International. Reprinted with permission of ASM International. All rights reserved. www.asminternational.org., 1984.

[15] Y. M. Chiang, D. Birnie III, W. D. Kingery, Physical Ceramics: principles for ceramic science and engineering, John Wiley & Sons, Inc. , 1997, p. 522.

[16] N. Bernstein, H. J. Gotsis, D. A. Papaconstantopoulos, M. J. Mehl, Physical Review B 71 (2005) 075203.

[17] Q. G. Fu, H.-J. Li, X.-H. Shi, K.-Z. Li, G.-D. Sun, Scripta Materialia 52 (2005) 923-927.

[18] F. Liao, S. L. Girshick, W. M. Mook, W. W. Gerberich, M. R. Zachariah, Applied Physics Letters 86 (2005) 171913-171913.

[19] R. Madar, Nature 430 (2004) 974-975.

[20] B. L. Oscar, L. O. Angel, G. Fernando, P. P. Nitin, Journal of the American Ceramic Society 88 (2005) 3531-3534.

[21] W. D. Callister Jr., Fundamentals of Materials Science and Engineering - An Integrated Approach, John Wiley & Sons, Inc., 2005, p. 712.

[22] X. Zhao, X. He, Y. Sun, J. Yi, P. Xiao, Acta Materialia 57 (2009) 893-902.

[23] F. H. Stillinger, T. A. Weber, Physical Review B 31 (1985) 5262.

[24] K. Chenoweth, S. Cheung, A. C. T. van Duin, W. A. Goddard, E. M. Kober, Journal of the American Chemical Society 127 (2005) 7192-7202.

[25] P. C. Kelires, EPL (Europhysics Letters) 14 (1991) 43-48.

[26] J. F. Vetelino, S. S. Mitra, Physical Review 178 (1969) 1349.

[27] M. Tang, S. Yip, Journal of Applied Physics 76 (1994) 2719-2725.

[28] X. Luo, G. Qian, W. Fei, E. G. Wang, C. Chen, Physical Review B 57 (1998) 9234.

[29] I. Szlufarska, A. Nakano, P. Vashishta, Science 309 (2005) 911-914.

[30] I. Szlufarska, R. K. Kalia, A. Nakano, P. Vashishta, Applied Physics Letters 85 (2004) 378-380.

[31] I. Szlufarska, R. K. Kalia, A. Nakano, P. Vashishta, Applied Physics Letters 86 (2005) 021915-021913.

[32] W. Kohn, L. J. Sham, Physical Review 140 (1965) A1133.

[33] J. C. Slater, G. F. Koster, Physical Review 94 (1954) 1498.

[34] C. M. Goringe, D. R. Bowler, E. Hernandez, Reports on Progress in Physics 60 (1997) 1447-1512.

[35] D. J. Chadi, M. L. Cohen, Physica Status Solidi (b) 68 (1975) 405-419.

[36] W. A. Harrison, Electronic Structure and the Properties of Solids, W.H.Freeman & Co Ltd, 1980, p. 586.

[37] W. A. Harrison, Elementary Electronic Structure, World Scientific, 2004, p. 838.

[38] W. A. Harrison, Physical Review B 24 (1981) 5835.

[39] Y. Li, P. J. Lin-Chung, Physical Review B 36 (1987) 1130.

[40] M. W. Finnis, A. T. Paxton, D. G. Pettifor, A. P. Sutton, Y. Ohta, Philosophical Magazine A 58 (1988) 143-163.

[41] W. M. C. Foulkes, R. Haydock, Physical Review B 39 (1989) 12520.

[42] J. A. Majewski, P. Vogl, Physical Review B 35 (1987) 9666.

[43] M. Kohyama, R. Yamamoto, Y. Ebata, M. Kinoshita, physica status solidi (b) 152 (1989) 533-541.

[44] M. Kohyama, S. Kose, M. Kinoshita, R. Yamamoto, Journal of Physics: Condensed Matter 2 (1990) 7791-7808.

[45] M. Kohyama, S. Kose, M. Kinoshita, R. Yamamoto, Journal of Physics: Condensed Matter 2 (1990) 7809-7823.

[46] M. Kohyama, S. Kose, R. Yamamoto, Journal of Physics: Condensed Matter 3 (1991) 7555-7573.

[47] J. L. Mercer, Physical Review B 54 (1996) 4650.

[48] A. P. Sutton, M. W. Finnis, D. G. Pettifor, Y. Ohta, Journal of Physics C: Solid State Physics 21 (1988) 35-66.

[49] D. Nguyen-Manh, D. G. Pettifor, V. Vitek, Physical Review Letters 85 (2000) 4136.

[50] A. T. Paxton, An introduction to the tight binding approximation - implementation by diagonalisation, in: Lecture notes: Multiscale Simulation Methods in Molecular Sciences Forschungszentrum Julich, Julich, 2009, p. 32.

[51] D. G. Pettifor, The Journal of Chemical Physics 69 (1978) 2930-2931.

[52] D. G. Pettifor, M. W. Finnis, D. Nguyen-Manh, D. A. Murdick, X. W. Zhou, H. N. G. Wadley, Materials Science and Engineering A 365 (2004) 2-13.

[53] D. G. Pettifor, Many-atom interactions in solids : proceedings of the International Workshop, Pajulahti, Finland, June 5-9, 1989, Springer-Verlag, 1990.

[54] L. Goodwin, A. J. Skinner, D. G. Pettifor, EPL (Europhysics Letters) 9 (1989) 701-706.

[55] A. P. Horsfield, P. D. Godwin, D. G. Pettifor, A. P. Sutton, Physical Review B 54 (1996) 15773.

[56] J. Robertson, Philosophical Magazine Part B 66 (1992) 615-638.

[57] D. A. Papaconstantopoulos, M. J. Mehl, S. C. Erwin, M. R. Pederson, Tight-binding hamiltonians for carbon and silicon, in: MRS Proceedings: Tight-Binding Approach to Computational Materials Science, vol 491, 1998.

[58] A. D. Patrick, X. Dong, T. C. Allison, E. Blaisten-Barojas, The Journal of Chemical Physics 130 (2009) 244704-244707.

[59] C. C. Fu, M. Weissmann, Physical Review B 60 (1999) 2762.

[60] M. Salvador, J. M. Perlado, A. Mattoni, F. Bernardini, L. Colombo, Journal of Nuclear Materials 329-333 (2004) 1219-1222.

[61] V. I. Ivashchenko, P. E. A. Turchi, V. I. Shevchenko, L. A. Ivashchenko, G. V. Rusakov, Physical Review B 66 (2002) 195201.

[62] D. G. Pettifor, Physical Review Letters 63 (1989) 2480.

[63] D. G. Pettifor, Bonding and Structure of Molecules and Solids, Oxford University Press, 1995, p. 259.

[64] M. Aoki, D. G. Pettifor, Physics of Transition Metals 1 (1993) 299-304.

[65] M. Aoki, Physical Review Letters 71 (1993) 3842.

[66] D. G. Pettifor, I. I. Oleinik, Physical Review B 59 (1999) 8487.

[67] T. Hammerschmidt, R. Drautz, Bond order potentials for bridging the electronic to atomistic modelling hierarchies, in: Lecture notes: Multiscale Simulation Methods in Molecular Sciences Forschungszentrum Julich, Julich, 2009, p. 18.

[68] D. W. Brenner, O. A. Shenderova, J. A. Harrison, S. J. Stuart, B. Ni, S. B. Sinnott, Journal of Physics: Condensed Matter 14 (2002) 783-802.

[69] R. Drautz, D. A. Murdick, D. Nguyen-Manh, X. Zhou, H. N. G. Wadley, D. G. Pettifor, Physical Review B 72 (2005) 144105.

[70] D. G. Pettifor, I. I. Oleinik, Physical Review Letters 84 (2000) 4124.

[71] D. A. Murdick, X. W. Zhou, H. N. G. Wadley, D. Nguyen-Manh, R. Drautz, D. G. Pettifor, Physical Review B (Condensed Matter and Materials Physics) 73 (2006) 045206-045220.

[72] G. C. Abell, Physical Review B 31 (1985) 6184.

[73] A. J. Dyson, P. V. Smith, Surface Science 355 (1996) 140-150.

[74] H. Balamane, T. Halicioglu, W. A. Tiller, Physical Review B 46 (1992) 2250.

[75] F. Gao, W. J. Weber, Nuclear Instruments and Methods in Physics Research Section B: Beam Interactions with Materials and Atoms 191 (2002) 504-508.

[76] M. Z. Bazant, E. Kaxiras, Physical Review Letters 77 (1996) 4370.

[77] A. E. Carlsson, C. D. Gelatt, H. Ehrenreich, Philosophical Magazine A 41 (1980) 241-250.

[78] M. Z. Bazant, E. Kaxiras, J. F. Justo, Physical Review B 56 (1997) 8542.

[79] J. F. Justo, M. Z. Bazant, E. Kaxiras, V. V. Bulatov, S. Yip, Physical Review B 58 (1998) 2539.

[80] N. A. Marks, Physical Review B 63 (2000) 035401.

[81] M. R. A.Urban, M.Mrovec, C.Elsaesser, and B.Meyer, Physical Review B 9 (2011).

[82] J. P. Perdew, A. Zunger, Phys. Rev. B 23 (1981) 5048.

[83] G. Kresse, J. Hafner, Phys. Rev. B 47 (1993) 558.

[84] P. E. Blöchl, Phys. Rev. B 50 (1994) 17953.

[85] G. Kresse, J. Hafner, Phys. Rev. B 49 (1994) 14251.

[86] G. Kresse, J. Furthmüller, Comput. Mat. Sci. 6 (1996) 15.

[87] G. Kresse, J. Furthmüller, Phys. Rev. B 54 (1996) 11169.

[88] G. Kresse, D. Joubert, Phys. Rev. B 59 (1999) 1758.